

**Geometric and electronic structure of misfit layered
compounds and epitaxial thin films of PbS on
transition metal dichalcogenides**

Dissertation
zur Erlangung des Doktorgrades
der Mathematisch-Naturwissenschaftlichen Fakultät
der Christian-Albrechts-Universität
zu Kiel

vorgelegt von
Julia Brandt

Kiel 2003

Referent/in: Priv.-Doz. Dr. Lutz Kipp

Korreferent/in: Prof. Dr. Felix Tuzek

Tag der mündlichen Prüfung: 19.02.2003

Zum Druck genehmigt: Kiel,

Der Dekan

Contents

1	Introduction	1
2	Misfit layered compounds and their constituents	3
2.1	Transition metal dichalcogenides	3
2.2	Cubic monochalcogenides	5
2.3	Misfit layered compounds	6
3	Experimental setup	9
3.1	Photoelectron spectroscopy	9
3.2	Scanning tunneling microscopy	13
3.3	Electron diffraction and electron microscopy	14
3.4	The surface science laboratory in Kiel	15
3.5	The photoelectron spectroscopy experiment at HASYLAB	16
4	Crystal growth and characterization	17
4.1	Chemical vapor transport	17
4.2	Molecular beam epitaxy	19
4.3	Characterization of the relevant single crystals	20
5	The electronic structure of PbS	29
6	Tracing the incommensurability of misfit layered compounds	38
6.1	Symmetries in the electronic structure of $(\text{PbS})_{1.14}\text{NbS}_2$	39
6.2	Misfit induced modification of the Fermi surface	41
6.3	Photoelectron diffraction from localized valence band states	45
6.4	Conclusions	47
7	What makes misfit compounds stick together?	48
7.1	Charge transfer in $(\text{PbS})_{1.18}\text{TiS}_2$ and $(\text{PbS})_{1.18}(\text{TiS}_2)_2$	48
7.2	Bonding mechanisms in $(\text{PbS})_{1.14}\text{NbS}_2$	51
7.3	Conclusions	61
8	Epitaxy of PbS on layered TMDC	63
8.1	Geometric structure of epitaxial thin films of PbS	64
8.2	Electronic structure of epitaxial PbS films on TiS_2	71
8.3	Conclusions	79
9	Summary and perspectives	81
	References	85
	List of abbreviations	95
	List of publications	96
	Acknowledgements	99

1 Introduction

The application of heterostructures from different crystal systems is an essential part of modern life. Basically, the development of modern computer technologies and its fast growing importance for everyday life is unthinkable without the creation of transistors, diodes and other electronic devices [1]. But also in basic research heterostructures play an important role, e. g. the formation of a two-dimensional electron gas in heterojunctions was a crucial precondition for the discovery of the integral and fractional quantum Hall effect [2,3]. The most convincing results in the preparation of heterostructures are achieved by molecular beam epitaxy [4, 5]. However, different problems arise during this growth process such as lattice mismatch induced mechanical strain and high defect density at the interface. Although a new kind of epitaxy has been developed [6] which uses quasi-two-dimensional crystals (e. g. transition metal dichalcogenides) that exhibit inert saturated surfaces without dangling bonds and reduces the influence of lattice mismatch, epitaxy remains a non-equilibrium process.

On the other hand, nature yields crystals that consist of an alternate stacking of different crystal systems [7]. Misfit layered compounds represent such a material class, where layers of transition metal dichalcogenides and two-atomic slices of a cubic monochalcogenide, e. g. PbS, are stacked alternately one upon the other, creating thus natural heterostructures. These compounds can synthetically be grown by a chemical vapor technique which is a rather slow process where thermodynamic considerations are applicable. Misfit layered compounds exhibit properties that are of special interest not only in connection with the formed interfaces but also in view of general solid state basics. Due to the different symmetry of the two constituting subsystems at the interface and their differing lattice constants a one-dimensional misfit along one of the in-plane layer axes is created. Contrarily, along the second orthogonal in-plane layer axis both lattices match exactly. Both subsystems are modulated mutually along the incommensurate axis and therefore lack translational symmetry which has long been included in the definition for crystals. In this context misfit layered compounds can be regarded as quasi periodic crystals [8]. The large stability and high stacking order is a second interesting property of misfit layered compounds. From a thermodynamic point of view the entropy of these crystals is significantly decreased by the observed precise alternate stacking of the subsystem layers. Therefore, the energy of the system must simultaneously be reduced with respect to the single non-interacting subsystems. Bonding mechanisms in misfit compounds are not well understood yet. Due to the incommensurability, the different electronic character and interface properties the interaction of the different subsystems is further complicated and new bonding mechanisms must be expected.

These two topics – the incommensurability and the stability of misfit layered compounds – take center stage within the present thesis (see Fig. 1.1). The access to both problems is taken from different directions. Probably the most straightforward approach is undertaken by comparing specific properties of misfit compounds to those of the subsystems as single crystals. For this purpose the pure components (the transition metal dichalcogenides NbS₂, NbSe₂ and TiS₂ and the cubic monochalcogenide PbS) are characterized with respect to their geometric and electronic structure. In case of PbS a detailed study of the electronic structure is performed since some problems concerning electronic properties had not been solved satisfactorily yet. The electronic structure of misfit layered compounds and their constituents will be investigated by angle resolved photoelectron spectroscopy with syn-

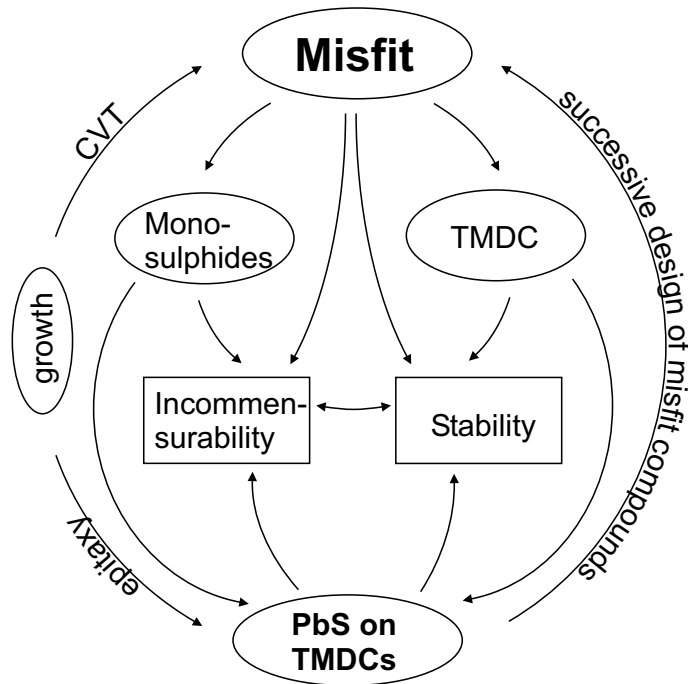


Figure 1.1: Schematic outline of this thesis. Its main topics concern misfit layered compounds and a similar system epitaxial PbS on transition metal dichalcogenides. Both enclose their fundamental properties of incommensurability and high stability. The aim of determining the bonding mechanisms which are responsible for the stability and the influence of the misfit on the electronic structure implies a precise knowledge of the single subsystems: transition metal dichalcogenides and cubic monosulphides.

chrotron radiation in the vacuum ultraviolet (VUV) as well as in the soft X-ray regime. An intermediate system between misfit compounds and the subsystems as single crystals is created by the epitaxial growth of an appropriate monochalcogenide on transition metal dichalcogenides. These epitaxial samples combine properties of the single crystals and of the respective misfit compound. It will thus be possible to distinguish between simple effects that emerge from the contact of both crystal systems and the properties that are unique to misfit compounds and that are responsible for their high stability and stacking order. Furthermore, the above mentioned fundamental differences between the non-equilibrium growth via epitaxy and crystal growth by chemical transport techniques will be pointed out.

Except for PbS that was used as natural mineral, the single crystals investigated within this thesis were grown by chemical vapor transport in the Kiel surface science laboratory. They were characterized in the framework of the DFG Forschergruppe on "Growth and interface properties of sulphide and selenide layer systems" by various methods concerning bulk properties and by surface sensitive techniques of the Kiel surface science laboratory. Photoemission experiments were carried out at the Hamburger Synchrotronstrahlungslabor HASYLAB at the Deutsches Elektronen-Synchrotron DESY and analyzed in the context of band structure calculations provided by E. E. Krasovskii.

2 Misfit layered compounds and their constituents

Misfit layered compounds with the general formula $(MX)_{1+\delta}(TX_2)_m$ ($M = \text{Pb, Sn, Bi}$ or rare earth metals; $T = \text{Nb, Ti, Ta, ...}$; $X = \text{S, Se}$; $m = 1, 2, 3$ and $0.08 < \delta < 0.28$) are built up by two very different material classes which are stacked in a layered way on top of each other. One layer is represented by a two atomic slice of a cubic monochalcogenide while the other layer consists of a three atomic transition metal dichalcogenide (TMDC) sandwich. The pure components exhibit as single crystals different properties. They will be described in the following chapters 2.1 and 2.2 before a closer description of the misfit compounds will be given in chapter 2.3.

2.1 Transition metal dichalcogenides

Transition metal dichalcogenides belong to the layered compounds of the type TX_2 , where T symbolizes an early transition metal of group IV (Ti, Zr, Hf), V (V, Nb, Ta) or VI (Cr, Mo, W) of the periodic table and X is one of the chalcogenides S, Se or Te . They are built up by three atomic sandwich layers, which are stacked on top of each other. Each sandwich consists of a hexagonally ordered sheet of transition metals that is surrounded by two hexagonal layer planes of chalcogen atoms (see Fig. 2.1 (a)). The bonds within one sandwich are of strong covalent and ionic character, while the interaction between different sandwich layers is rather weak and van-der-Waals like. Consequently numerous electrical, optical and mechanical properties are of a two-dimensional character, e.g. the electrical and thermal conductivity.

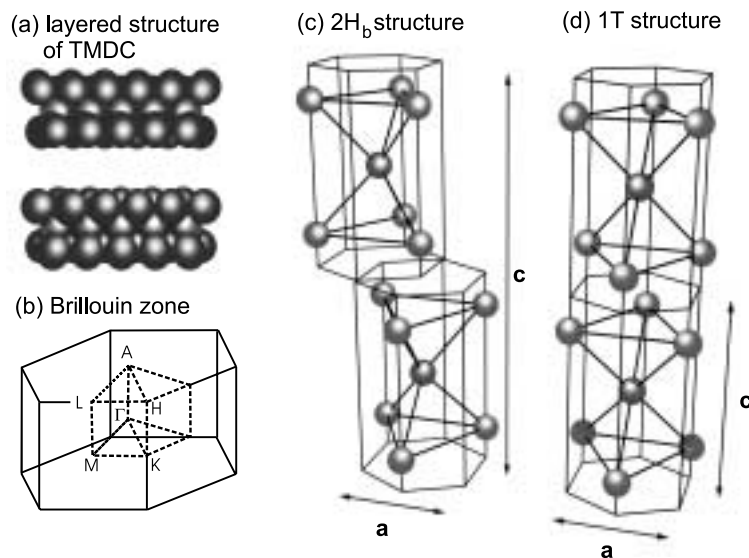


Figure 2.1: (a) Layered structure of transition metal dichalcogenides and (b) the corresponding Brillouin zone. (c) Unit cells of the $2H_b$ and (d) the $1T$ polytype, from [9].

geometric structure Although all transition metal dichalcogenides are built up in a similar way, they still differ in their crystallographic description. As can be seen in Fig. 2.1 (c) and (d) the transition metal atom can be coordinated by the six nearest chalcogen atoms in two different ways: In the $1T$ structure (symmorphic space group $P\bar{3}m1$) the chalcogen

atoms form a nearly regular octahedron. The unit cell contains only one sandwich layer in the c direction. The unit cell of the 2H structure (non-symmorphic space group $P6_3/mmc$) is extended over two sandwich layers. In one layer the chalcogen atoms are situated above each other. It is rotated by 60° with respect to the neighboring layers. Different stacking sequences of the layers result in various polymorphic types such as 1T, $2H_a$, $2H_b$, 3R etc., where the number denotes the number of layers which are contained in one unit cell.

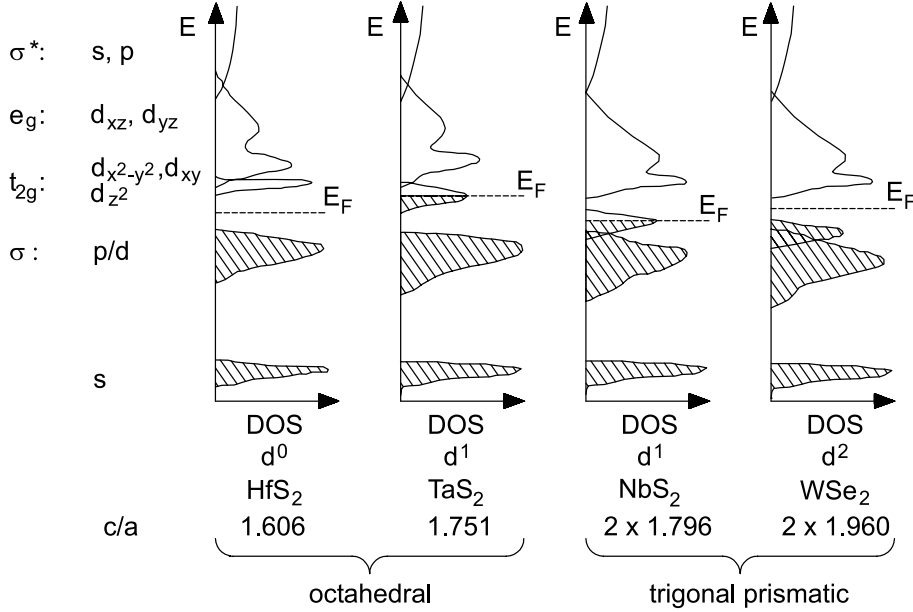


Figure 2.2: Simple model of the electronic structure after [10]

electronic structure The electronic structure of transition metal dichalcogenides can be described in a general scheme offered first by Wilson and Yoffe [10]. Fig. 2.2 shows the energetic positions of the relevant band states: According to Wilson and Yoffe the s - and p - orbitals of the chalcogen atoms are divided into unoccupied (σ^*) and occupied (σ) band states, separated by an energy gap of several eV. The metal derived d states are located within this bonding-antibonding energy gap. They are split into a twofold degenerate level e_g associated with the d_{xz} and d_{yz} orbitals and into a threefold degenerate level t_{2g} associated with the d_{z^2} , $d_{x^2-y^2}$ and d_{xy} orbitals. The degree of filling of d bands largely determines the electrical, magnetic and optical character of the various compounds. This can be understood by a simple ionic picture: Two electrons are transferred from the transition metal to the chalcogen atoms where the p orbitals are then completely filled. The remaining electrons can occupy the d_{z^2} band of the metal to a certain degree: The transition metals of group IVb are in a d^0 configuration, the d_{z^2} band stays unoccupied, the respective TMDC are generally semiconductors. In TMDC with transition metals from group Vb, the d_{z^2} band is half filled resulting in metallic behaviour. Due to the completely filled d_{z^2} band of group VI transition metals, the respective TMDC show semiconducting properties.

The electronic structure is directly related to the geometric structure and vice versa. This can be seen by the effect that the coordination of chalcogen atoms changes from octahedral for group IVb metals to trigonal prismatic for group VIb metals. (Group Vb TMDC exist in

both coordinations.) In the latter case the d_{z^2} band is split off from the other d bands and lowered in energy. This energy gain compensates in trigonal prismatic TMDC the energy loss due to a higher Madelung energy in this coordination.

intercalation Of particular interest is the possibility to intercalate foreign atoms or molecules into the van-der-Waals gap between the host layers. This method of modifying the physical properties and in particular the electronic structure was widely studied and discussed in view of practical applications. It is for instance possible to achieve semiconductor-to-metal transitions (or vice versa) or to turn a normal conductor into a superconductor. The occurring changes are ascribed to a charge transfer from the introduced species to the host lattice, which is also regarded as the driving force of the intercalation. They are simply described in terms of the rigid band model (RBM), in which it is assumed that the band structure of the host material is not changed except for the filling of the conduction band due to the charge transfer. Going into more detail it is evident that the rigid band model is not strictly applicable. Due to a decoupling of the host layers other changes going beyond the RBM occur: In general, the perpendicular dispersion of electronic states is markedly reduced and band widths and band gaps are significantly altered. These changes are already taking place at an early stage of intercalation. The most important categories of intercalants are alkali metals and other simple metals like copper and silver [11], 3d transition metals [12] and organic molecules like ammonia and hydrazine [13]. The intercalation of transition metal dichalcogenides with alkali metals can be achieved by different methods, e. g. immersion in alkali-ammonia solutions, electrolysis of a solution of an appropriate metal salt or *in situ* through alkali-metal deposition in ultra high vacuum onto a clean surface. Although the latter method has the great advantage that the surface remains more or less intact it is a complex process which is not well understood. This applies in particular to the diffusion of the absorbed species towards the interior where defects seem to play a major role and the detailed structure of the resulting intercalation compounds. Misfit layered compounds can be regarded as a strongly intercalated transition metal dichalcogenide which combines the advantages of both electrochemical and *in situ* intercalation: The crystals have a high surface quality on the one hand and their crystallographic structure is precisely known. The description as intercalation compounds is not only formal, because the electrical transport properties are similar to those of the intercalates M_xTX_2 , leading to the suggestion that the conduction takes place in the TMDC layers only. As it will be demonstrated in Chapter 7 also the electronic band structure of misfit compounds largely resembles the band structure of alkali metal intercalated TMDC.

2.2 Cubic monochalcogenides

The second constituent of misfit layered compounds is a monochalcogenide which crystallizes in the cubic rock salt structure. One has to distinguish between compounds containing divalent Pb, Sn or Bi and trivalent rare earth compounds, which are especially interesting for their magnetic properties. Being one of the constituents of misfit compounds they show different behaviour particularly concerning a possible charge transfer; this will be discussed later in chapter 7. Some of them, e. g. SnS, are hypothetical since they do not exist in the rock salt crystal structure as pure component. Others like PbS can be found as natural minerals (galena) or can be grown artificially.

Lead sulphide (PbS) crystallizes in a cubic closest-packed rock salt structure with space

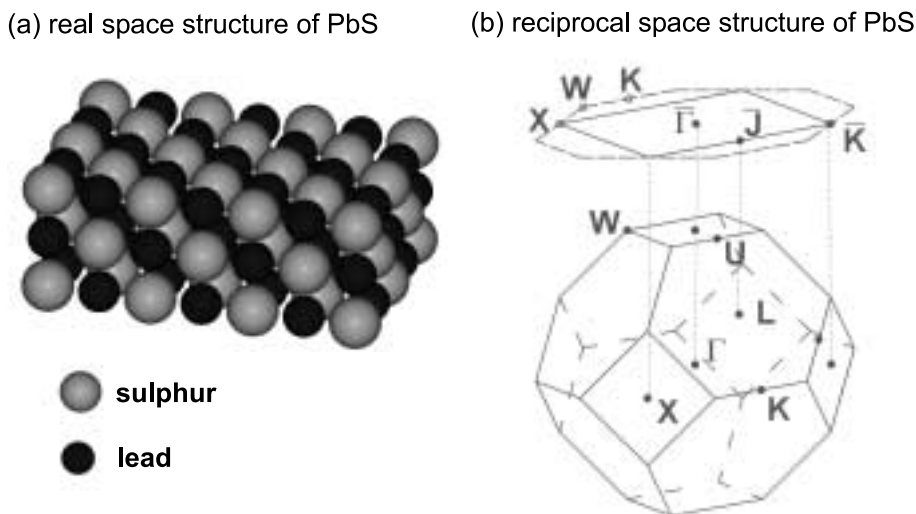


Figure 2.3: (a) Rock salt structure of PbS and (b) the corresponding bulk Brillouin zone. The surface Brillouin zone of the (001) surface is depicted above.

group Fm3m (see Fig. 2.3 (a)). It belongs to the IV-VI semiconductors with a narrow energy gap of $E_g=0.41$ eV at room temperature. It was one of the first semiconductors ever used in electronic devices. The rectifying behavior of metal semiconductor contacts was demonstrated initially by Braun 1874 on galena interfaces. (Even four thousand years ago PbS was used by ancient Egyptians as a main ingredient of early cosmetics [14].) Currently, for example, PbS finds wide application in diode lasers [15], thermovoltaic energy converters [16] or infrared detectors. Other unusual and unique properties are its high dielectric constant ($\epsilon \approx 170$ [17]) and a high mobility. But also in basic research PbS is a subject of great interest. Since it can be obtained as crystals of excellent quality and due to its simple cubic structure it served as a model compound for photoemission theory [18].

2.3 Misfit layered compounds

Misfit layered compounds were first prepared around 1970 but not recognized as such [19–21]. They are a special kind of composite or intergrowth crystal. These are crystals with at least two interpenetrating sublattices each with three-dimensional periodicity, characterized by a unit cell and space group [7]. In the case of misfit layered compounds one sublattice is represented by up to three sandwich layers of a transition metal dichalcogenide. The second sublattice contains a double layer of a cubic monochalcogenide (see Fig. 2.4).

geometric structure Layers of the two subsystems are stacked alternately one upon the other. One of the in-plane axes of the first subsystem (chosen to be the a axis) is parallel to the a axis of the second subsystem, but the length ratio is incommensurate, constituting thus a one-dimensional misfit. The b axis in both subsystems is chosen orthogonally to the a axis. For the cubic monochalcogenide these lattice vectors are those of the fcc lattice. For the TMDC subsystem the primitive a vector is chosen, the b vector is orthogonal to it within the layer plane with a length of $\sqrt{3} \cdot a$ (see Fig. 2.4). The composition of the crystal, i. e. the ratio of MX to $(\text{TX}_2)_m$ is determined by the ratio of the a axes of the subsystems. It varies between 1.56 for $(\text{YS})_{1.28}\text{CrS}_2$ [22] and 1.85 for $(\text{BiS})_{1.08}\text{TaS}_2$ [23]. Table 2.1

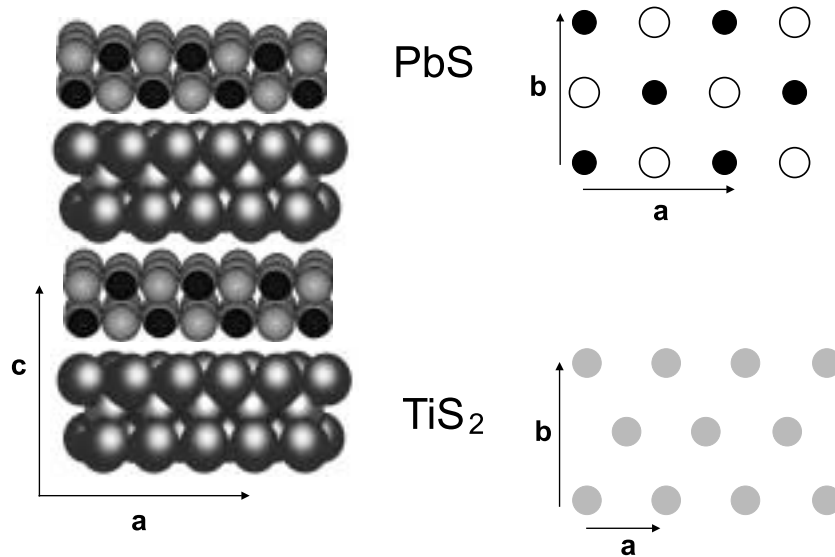


Figure 2.4: Crystal structure of the misfit layered compound $(\text{PbS})_{1.18}\text{TiS}_2$ with the incommensurate \mathbf{a} axis and the layer perpendicular \mathbf{c} axis. On the right the single subsystems are shown represented by a monatomic layer along the (ab) plane respectively. The Pb atoms are denoted as black circles, the S atoms as open circles for the PbS layer. For the sake of clarity the TiS_2 subsystem is represented only by the Ti atoms as grey circles. It should be noted that the \mathbf{b} axis in the TMDC subsystem deviates from the lattice vector that is usually chosen for pristine TMDC.

summarizes the unit cell dimensions of the misfit compounds that will be studied within this thesis. To be more precise one has to take into account that the two subsystems mutually modulate each other incommensurately, which means that the structure obtained from the three-dimensional space groups of the two subsystems gives only the average structure of the misfit compound. The complete structure, including the mutual modulations, can be described by a $(3+1)$ -dimensional superspace group.

compound	subsystem	a[Å]	b[Å]	c[Å]	reference
$(\text{PbS})_{1.14}\text{NbS}_2$	PbS	5.834	5.801	11.90	[24]
	NbS ₂	3.313	5.801	23.80	[24]
$(\text{PbS})_{1.14}(\text{NbS}_2)_2$	PbS	5.829	5.775	35.86	[25]
	NbS ₂	3.326	5.775	35.87	[25]
$(\text{PbS})_{1.13}\text{TaS}_2$	PbS	5.825	5.779	23.96	[23]
	TaS ₂	3.304	5.779	23.96	[23]
$(\text{PbS})_{1.18}\text{TiS}_2$	PbS	5.800	5.881	11.76	[26]
	TiS ₂	3.409	5.881	11.76	[26]
$(\text{PbS})_{1.18}(\text{TiS}_2)_2$	PbS	5.761	5.873	17.46	[27]
	TiS ₂	3.390	5.873	17.46	[27]

Table 2.1: Unit cell dimensions of the misfit layered compounds that are relevant for this thesis.

electronic structure The electronic structure of misfit layered compounds can be described in a first approximation as a simple superposition of the constituents except for a charge transfer from the MX subsystem to the TX₂ layer. This charge transfer is the reason for the existence of misfit compounds like (PbS)_{1.12}VS₂ or (LaS)_{1.20}CrS₂ while the pristine dichalcogenides VS₂ and CrS₂ do not exist in a stable state. Exemplarily the band structures of the relevant compounds (PbS)_{1.14}NbS₂ and (PbS)_{1.18}TiS₂ will be discussed in further detail: On the basis of the rigid band model we expect due to the charge transfer a decrease of the number of holes in the d_{z²} band of NbS₂ and an equivalent number of holes in the valence band of the PbS subsystem (see Fig. 2.5), and therefore a contribution to the conductivity from holes of both subsystems. In TiS₂ containing compounds the transferred electrons occupy the broad Ti 3d conduction band, suggesting an electron conduction in the TMDC subsystem. These expectations could not be confirmed by transport measurements [28]. For titanium misfit compounds both Hall and Seebeck coefficients were negative indicating that electrons are the major charge carriers. Since holes in the valence band are expected to have a higher mobility than the electrons in the Ti 3d band, a positive Hall coefficient and a negative Seebeck coefficient are likely but have not been observed. The rigid band model seems not to hold. There are various explanations ranging from a strong deformation of the Fermi surface due to interlayer bonds [29] through a localization of charge carriers due to a mutual modulation of the potential in the MX subsystem [30] to an exchange of cations between the two subsystems [31]. In niobium misfit compounds the Hall coefficient is positive while the Seebeck coefficient is still negative. In view of the presence of holes as well as electrons, the determination of the number of holes in the MX subsystem is very uncertain and definite conclusions about a contribution from the MX layers cannot be drawn. One still has to keep in mind, that the understanding of electrical transport properties is very complex. In particular the interpretation of the Seebeck coefficient is rather uncertain, because a lot of assumption must be made. Therefore one of the aims of this thesis is to achieve a more profound knowledge of the electronic structure of misfit layered crystals by means of angle resolved photoemission and an appropriate theory.

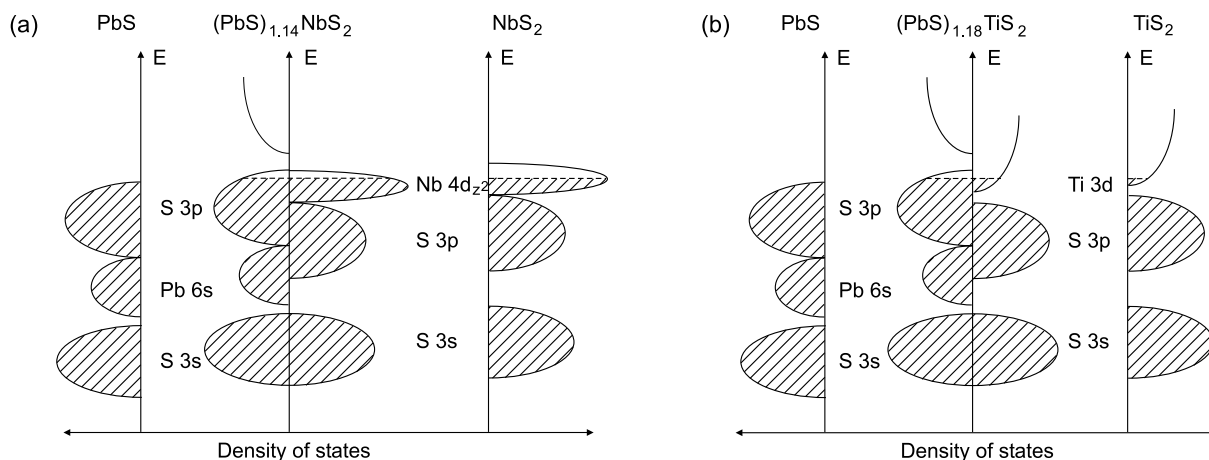


Figure 2.5: Simple model for the electronic band structure of misfit layered compounds after [28] exemplarily for (a) (PbS)_{1.14}NbS₂ and (b) (PbS)_{1.18}TiS₂

3 Experimental setup

The experimental setup that was used to characterize and investigate the relevant single crystals as well as the epitaxial thin films of lead sulphide will be introduced in the following. The emphasis will be laid on the experimental methods used by our group, i. e. on surface sensitive techniques to study the geometric and electronic structure of solid materials, in particular angle-resolved photoelectron spectroscopy (ARPES, Chapter 3.1), scanning tunneling microscopy (STM, Chapter 3.2) and low energy electron diffraction (LEED, Chapter 3.3). Due to the surface sensitivity all techniques are associated with high experimental efforts to obtain and maintain ultra-high vacuum (UHV) conditions in the 10^{-10} mbar range throughout the whole system of the Surface Science Laboratory in Kiel (Chapter 3.4) and the experimental station in Hamburg (Chapter 3.5) which both are connected by a transportable vacuum chamber. Thus the samples can be investigated not only using the experiments in Kiel but also by high-resolution photoelectron spectroscopy with synchrotron radiation in Hamburg without breaking the UHV. Due to the DFG Forschergruppe on "Growth and interface properties of sulphide and selenide layer systems" also bulk specific techniques such as transmission electron microscopy and X-ray diffraction were applied to the crystals studied in this thesis. Also the chemical composition was checked by energy-dispersive X-ray analyses. However, these techniques will not be described. In Chapter 4.3 some of these measurements will be introduced, but the interpretation should be understandable with the knowledge from standard text books.

3.1 Photoelectron spectroscopy

In the last 30 years **A**nge **R**esolved **P**hotoelectron **S**pectroscopy (ARPES) has known a continuous development and is now established as one of the most fundamental and direct techniques to probe the occupied states in solids [32]. With the development of synchrotron radiation facilities as sophisticated light sources together with the technological progress in the development of high resolution energy spectrometers and the advances in vacuum technologies it is nowadays possible to perform various modes of photoemission which enable an understanding of solid state properties that still go far beyond a simple determination of the experimental band structure $E(\mathbf{k})$.

Photoelectron spectroscopy is based on the photoelectric effect [33], which was interpreted as a quantum phenomenon by Albert Einstein [34] who received therefore the Nobel prize in 1921. The main principle of this effect is depicted in Fig. 3.1: A photon with the energy $h\nu$ impinges on a sample surface. An electron is excited from an occupied state with the binding energy E_B and if the photon energy exceeds the work function Φ of the sample the electron can leave the sample and is detected under the emission angles ϑ and φ with its kinetic energy E_{kin} :

$$E_{kin} = h\nu - \Phi - E_b. \quad (3.1)$$

Theoretical aspects A theoretical approach is needed that allows to relate the photoelectron intensity to the electronic band structure. In the three-step model that was originally introduced by Spicer [35, 36] the photoemission process is divided into three steps: the photoexcitation of the electrons, the motion of the electrons through the crystal and the escape of the electrons over the surface barrier into the vacuum.

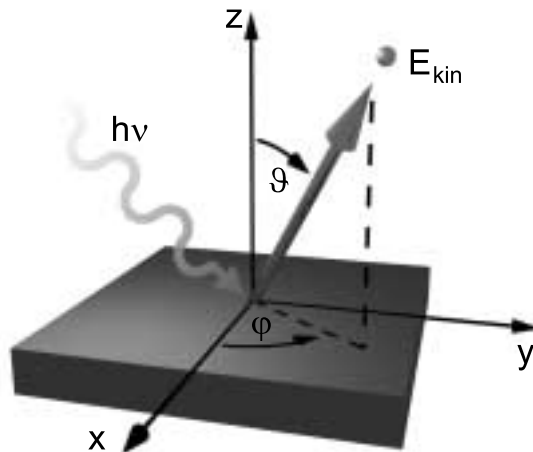


Figure 3.1: Schematic representation of the photoemission process: an incoming photon $h\nu$ excites photoelectrons that can be detected by their kinetic energy E_{kin} and the emission angles ϑ and φ , from [9].

The photoionization as the first step is a very fast process. It is therefore usually described within the sudden approximation. A further simplification neglects many-body interactions (one-particle interpretation). The transition probability from occupied initial states $|\Psi_i\rangle$ with energy E_i to empty final states $|\Psi_f\rangle$ with energy E_f is given by a Golden rule-type expression:

$$w_{fi} = \frac{2\pi}{\hbar} |\langle \Psi_f | H_1 | \Psi_i \rangle|^2 \delta(E_f - E_i - h\nu) \quad (3.2)$$

The operator H_1 describes the interaction between the electron with momentum \mathbf{p} and a photon field \mathbf{A} :

$$H_1 = \frac{e}{2mc} (\mathbf{A} \cdot \mathbf{p} + \mathbf{p} \cdot \mathbf{A}) + \frac{e^2}{2mc^2} \mathbf{A}^2. \quad (3.3)$$

Within the dipole approximation which neglects multi-photon processes and assumes the wavelength of the light to be large compared to atomic dimensions this expression is simplified to $H_1 = \frac{e}{2mc} \mathbf{A} \cdot \mathbf{p}$. Summing up all initial and final states we arrive at an expression for the total photoabsorption:

$$I \propto \sum_{\Psi_i, \Psi_f} |\langle \Psi_f | \mathbf{A} \cdot \mathbf{p} | \Psi_i \rangle|^2 \delta(E_f - E_i - h\nu). \quad (3.4)$$

The energy conservation is explicitly given by the δ -function. In Ref. [37] it is shown that in the limit of weak electron damping and under neglect of the photon momentum also the momentum is conserved in the matrix element except for a reciprocal lattice vector: $\mathbf{k}_f = \mathbf{k}_i + \mathbf{G}$. Then the photoemission current can be interpreted in terms of direct transitions from occupied initial states $|\Psi_i\rangle$ with energy E_i to empty final states $|\Psi_f\rangle$ with energy E_f (see Fig. 3.2 left panel).

The second step is the propagation of the excited electrons through the crystal to the surface. Within this process the interaction of the electron with other electrons and phonons leads to a decrease of the lifetime of its excited state and thereby to a broadening of the

emission peaks of the photoelectron spectrum. Inelastically scattered electrons result in a background that increases to lower kinetic energies in the spectrum. Furthermore these interactions lead to a finite mean free path of the photoelectrons that depends on their kinetic energy. In the vacuum ultraviolet (VUV) regime of photoemission the mean free path of the electrons is of the order of 1 nm and causes the extreme surface sensitivity of photoelectron spectroscopy.

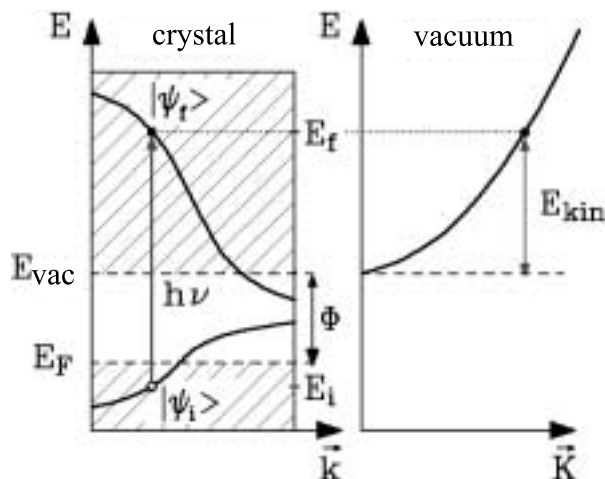


Figure 3.2: *Electronic transitions involved in the photoemission process. An electron is excited from an initial state $|\Psi_i\rangle$ to a final state $|\Psi_f\rangle$ and leaves the crystal with the kinetic energy E_{kin} .*

Finally the electrons have to escape from the surface into the vacuum (see Fig. 3.2). Within this process the surface parallel component of the wave vector is conserved except for a reciprocal vector of the surface lattice \mathbf{G} : $\mathbf{K}_{\parallel} = \mathbf{k}_{f\parallel} + \mathbf{G}$, where we can relate \mathbf{K}_{\parallel} with the measured quantities:

$$\mathbf{K}_{\parallel} = \sqrt{\frac{2m}{\hbar^2} E_{kin}} \sin \vartheta \begin{pmatrix} \cos \varphi \\ \sin \varphi \end{pmatrix}. \quad (3.5)$$

The surface perpendicular component of the wave vector of the photoelectrons $\mathbf{k}_{f\perp}$ remains undetermined because of the broken translational symmetry perpendicular to the surface. Assuming direct transitions we can express it as a function of the photon energy:

$$\mathbf{k}_{f\perp} = \mathbf{k}_{f\perp}(h\nu). \quad (3.6)$$

Further assumptions about the final states allow to determine the electronic structure perpendicular to the surface. Usually final states must either be known from theory or they can be approximated by the dispersion of free electrons ($E \propto k^2$) that are energetically shifted by the inner potential of the sample.

Photoemission modes In a photoemission experiment we measure the photoelectron intensity as a function of different parameters $I = I(E_{kin}, \vartheta, \varphi, h\nu)$. Varying some of them during a measurement and keeping others constant gives rise to different photoemission modes. Those that are used within this thesis shall be described in the following:

Energy Distribution Curve (EDC): $I = I(E_{kin}, \cdot)$

The energy distribution curve is probably the most important technique in photoelectron spectroscopy. The emission angles ϑ and φ as well as the photon energy $h\nu$ are kept constant and the photoelectron intensity is measured as a function of the kinetic energy. Thus both initial and final state are varied simultaneously and when an allowed transition lies within the scanned energy window it appears as a peak in the energy distribution curve. With the emission angles and the kinetic energy of the peak Equation 3.5 allows to determine the surface parallel component of the wave vector that belongs to this transition. By taking EDC at various emission angles it is thus possible to map the electronic structure within defined directions in reciprocal space parallel to the surface. Instead of varying the emission angles we can change the photon energy for each spectrum of a series. According to Equation 3.1 the detected kinetic energy has then to be adjusted in order to measure the respective binding energy range. With further assumptions concerning the final states we can thus determine the electronic structure perpendicular to the surface.

Azimuthal Angle Scan (AAS): $I = I(\cdot, \varphi)$

During the azimuthal angle scan the photon energy and the detected kinetic energy as well as the polar angle ϑ are kept constant. Only the azimuthal angle φ is varied while the photoelectron intensity is measured. Hence, the electron analyzer is moved concentrically around normal emission above the sample surface. This photoemission mode can thus be used to determine symmetries in the electronic structure, particularly it is used to find the highly symmetric directions during a photoemission experiment.

Photoelectron Angular Distribution (PAD): $I = I(\cdot, \vartheta, \varphi)$

The PAD mode has recently been developed [38] and has successfully been used to study Fermi surfaces in great detail, e. g. [38–40]. It is an even more sophisticated mode to study symmetries in the electronic structure than the AAS, but it is connected to a considerable time exposure. Like in the AAS mode the kinetic energy and the photon energy are held constant. In contrast to it both emission angles are varied thus that we obtain a horizontal cut through the electronic structure within the Brillouin zone at a constant initial energy.

X-ray photoelectron spectroscopy Instead of using light with energies in the ultraviolet range as described above it is also possible to perform photoelectron spectroscopy with higher excitation energies in the soft X-ray regime ($200 \text{ eV} \leq h\nu \leq 700 \text{ eV}$). The photon energy is then high enough to excite electrons from core levels. The simplest application of XPS is the determination of the chemical composition of the investigated sample, as the binding energies are characteristic for the specific elements (**E**lectron **S**pectroscopy for **C**hemical **A**nalysis (ESCA)). Still more information can be obtained by taking energy shifts and line shapes into account and analysing them carefully. The exact peak positions may be capable of indicating the chemical state of the component elements of the sample. From line shapes it is possible to draw conclusions even about valence band properties because valence band electrons are generally involved in relaxation processes that follow the core electron excitation. An asymmetry in core level peaks indicates for example the metallic

behavior of the respective sample¹ [41]. Other many-body effects arise from the participation of more than one electron during the photoemission process; for a more detailed description see e.g. Ref. [42].

3.2 Scanning tunneling microscopy

Since 1981 when the first successful experiments were performed by G. Binnig, H. Rohrer and coworkers [43], the scanning tunneling microscope (STM) has evolved as the most powerful tool for the investigation of the local geometric and electronic structure of surfaces in real space. Only five years later Binnig and Rohrer received the Nobel Prize in physics. Especially for the characterization of crystal surfaces and the understanding of electronic properties and the growth morphology of epitaxial films the STM is of invaluable general importance.

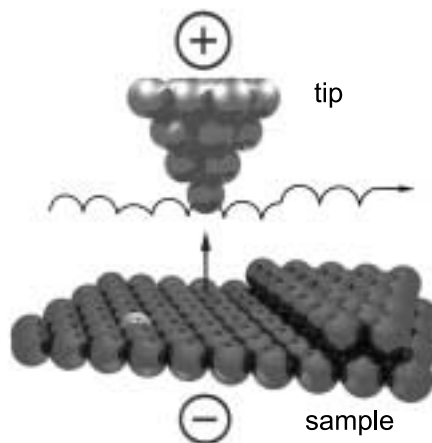


Figure 3.3: Principle set-up of a STM experiment. A voltage is applied between the sample and the tip. When the distance between them is small enough electrons can tunnel from the sample to the tip or vice versa, from [9].

The principle of scanning tunneling microscopy is depicted in Fig. 3.3. A voltage U_g is applied between a thin metal tip (here: tungsten) and the sample. The tip is approached very closely to a distance of only a few Å to the sample surface. When the distance is small enough that the wave functions of the tip and the sample overlap significantly the current I_t arising from electrons that tunnel between tip and sample can be measured:

$$I_t \sim e^{-2\kappa d} \quad (3.7)$$

The quantum mechanical tunneling effect is strongly dependent on the distance d between the tip and the sample surface (κ is a constant depending on the height of the potential barrier). By scanning the tip over a defined area of the surface it is thus possible to receive detailed information about the surface topography. One can distinguish between two standard modes of using the STM: The *constant current mode* uses an electronic feedback loop

¹This effect can be explained as follows: When a core electron is excited within the photoelectron process a core level photohole is created. The conduction electrons at the Fermi level are capable to move and screen the localized potential of the photohole. Hence, the kinetic energy of the photoelectron is reduced and the core level line shape becomes asymmetric.

to keep the tunneling current constant by moving the tip vertically to the surface. Hence, the tip follows a contour line of constant local density of states which offers information about the surface morphology. In the *constant height mode* the feedback loop is switched off so that the tip remains at a constant height above the sample and the tunneling current is measured which contains information about the local density of states (LDOS) of the sample surface.

3.3 Electron diffraction and electron microscopy

Low energy electron diffraction (LEED) can reasonably claim to be the oldest of modern surface science techniques. The first LEED experiment by Davisson and Germer [44] provided the first demonstration of the wave nature of electrons.

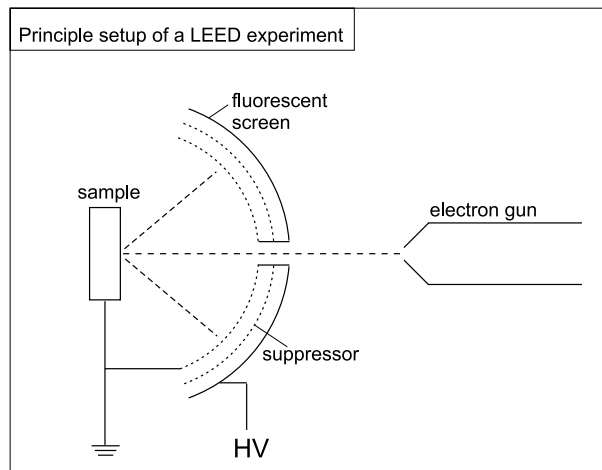


Figure 3.4: *Schematic diagram of a typical LEED experiment*

Still it is a powerful tool for the investigation of the geometric structure of surfaces in reciprocal space and therewith a useful complement to scanning tunneling microscopy. It is of particular importance for epitaxial samples, as the orientation of the epilayer with respect to the substrate and their lattice constants can easily be obtained. Also the sharpness of the LEED spots gives a first hint on the structural order of the epitaxial films.

A schematic diagram of a typical LEED system is shown in Fig. 3.4. The electron gun delivers a beam of typically $1 \mu\text{A}$ at energies in the 20...300 eV range. Electrons scattered or emitted from the sample pass the field free region between the sample and an inner grid which both lie on ground potential. The suppressor is laid on a potential close to that of the electron gun filament to suppress all electrons that have not been scattered elastically. Finally the electrons are reaccelerated onto the fluorescent screen where they can be observed as bright spots.

More bulk sensitivity is achieved by the use of electrons with higher kinetic energy. Transmission electron microscopes (TEM) provide electrons with energies of typically 10...100 keV, transmission electron diffraction patterns are therefore bulk specific and complete the information obtained from LEED. Additionally high-resolution lattice images and X-ray microanalysis spectra taken with the TEM were used to characterize the stacking order and the chemical composition of misfit layered compounds.

3.4 The surface science laboratory in Kiel

The experimental techniques described above are combined with different preparation chambers in the laboratory for surface science in Kiel (see Fig. 3.5).

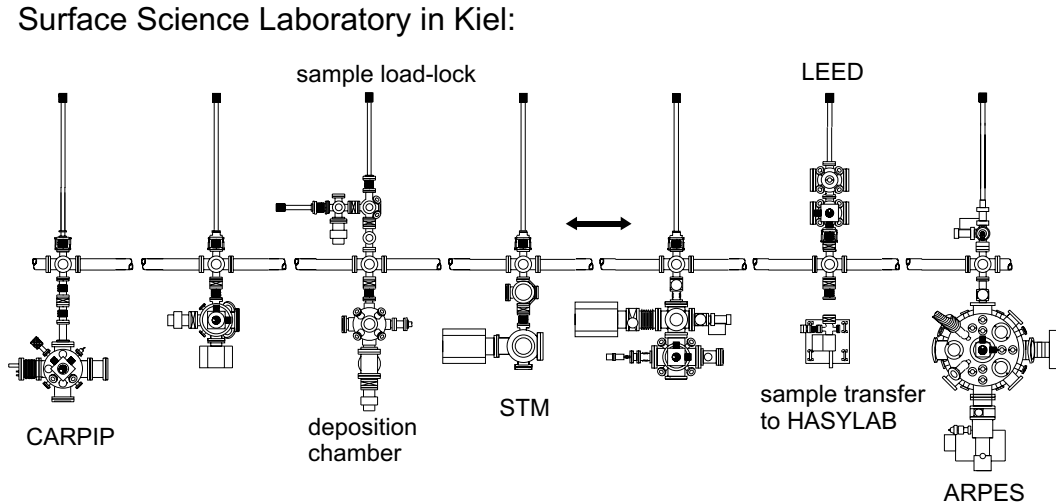


Figure 3.5: The surface science laboratory in Kiel. The experimental chambers for ARPES, STM, CARPIP and LEED as well as the deposition chamber for van der Waals epitaxy are connected by a transfer tube keeping the whole system under UHV conditions.

In order to perform different measurements on the same sample all preparation and experimental chambers are connected by a long transfer tube. It is held on a base pressure of $2 \cdot 10^{-10}$ mbar by several different pumps in order to conserve a high surface quality of single crystals and even epitaxial samples. Inside the tube a carrier [45] ("sample train") with a loading capacity for ten sample holders provides the transport of the samples to the different vacuum chambers where they can be introduced by magnetically coupled rods with a pick up assembly [46]. The individual chambers are shown in Fig. 3.5. The experimental chambers comprise the combined angle resolved photoemission and inverse photoemission (CARPIP) which allows to determine the electronic structure on both sides of the Fermi level. The *Omicron Micro STM* used in this thesis is a commercial UHV-STM that has been equipped later with an eddy current damping system in order to integrate it into the surface science laboratory in Kiel [45, 47]. It is operated at room temperature. The chamber for angle resolved photoemission (ARPES) is equipped with a Helium discharge lamp that provides unpolarized radiation with a photon energy of $h\nu = 21.22$ eV. Furthermore a Mg/Al double anode X-ray system with a photon energy of $h\nu = 1253.6$ eV and 1486.8 eV respectively facilitates the use of the chamber for X-ray photoemission studies. A LEED system is also integrated into the UHV system. The deposition chamber was developed originally for van-der-Waals epitaxy [48, 49]. It consists of a three-wall-spherical UHV chamber [46] with a base pressure of typically 10^{-10} mbar. The hollow space between the two inner spheres can be filled with liquid nitrogen in order to serve as a cryoshroud. Between the middle and the outer sphere a thermally insulating vacuum is produced by a rotary pump. The chamber is furthermore equipped with a mass spectrometer in order to control the residual gas during a preparation. The manipulator contains a resistive heater that can raise the temperature of a sample to 750 K and a thermocouple to measure the temperature. A closer description of the deposition chamber is given in [49]. In order to

produce PbS thin epitaxial films on different substrates a new effusion cell was constructed and integrated into this chamber [50]. The samples are introduced into the UHV system via the load-lock chamber that can be baked out within six hours. In order to use the advantages of synchrotron radiation and of the spectrometer ASPHERE which will be described in the following chapter the laboratory is equipped with a transportable UHV chamber. Samples that were prepared and characterized in Kiel can be transferred into this chamber that is kept on UHV with an ion getter pump and transported to Hamburg.

3.5 The photoelectron spectroscopy experiment at HASYLAB

At the **H**amburger **S**ynchrotronstrahlungslabor (HASYLAB) photoelectron spectroscopy is performed with synchrotron radiation. The HONORMI (**H**ochauflösender **N**ormalinzenzmonochromator) monochromator at the W 3.2 beamline provides light in the $5 \leq h\nu \leq 35$ eV energy range. The spectrometer ASPHERE (**A**ngular **S**pectrometer for **P**hotoelectrons with **H**igh **E**nergy **R**esolution) [51,52] is installed permanently at the beamline. The 180° spherical energy analyser is mounted on a two-axis goniometer [53,54] and can be moved by computer-controlled stepping motors. Therewith it is possible to perform the angle scanning photoemission modes described above. In contrast to other spectrometers, that are installed at a fixed position and where the sample is rotated instead, we can collect photoelectrons in the whole hemisphere above the sample without changing the orientation of the sample with respect to the incoming light. This setup allows to study phenomena that depend on the incoming light like matrix element effects or effects derived from the polarization of the light. The photoemission experiment is equipped with a two-stage evaporative cooling liquid helium cryostat, so that the sample temperature can be varied between room temperature and ≈ 10 K. The whole experimental station can be transported and connected to the undulator beamline BW3 where the SX-700 monochromator provides radiation in the energy range of $35 \leq h\nu \leq 1500$ eV [55]. Here, it is possible to perform high-resolution XPS measurements with tunable photon energies.

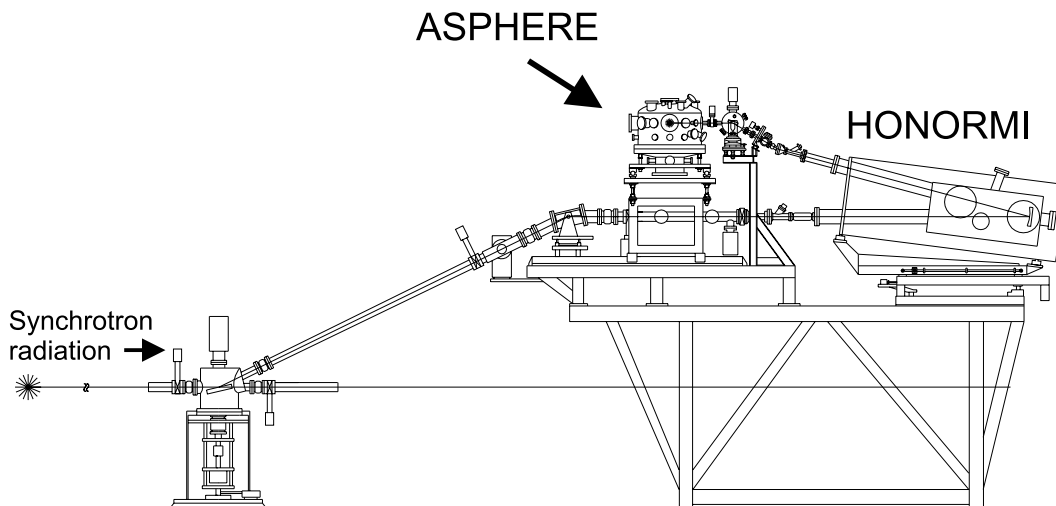


Figure 3.6: *Experimental set-up of the photoemission experiment at HASYLAB. The storage ring DORIS serves as a tunable light source. The photons pass the monochromator HONORMI and reach as monoenergetic light the experimental chamber where the spectrometer ASPHERE detects the energy of the excited electrons.*

4 Crystal growth and characterization

The quality of experimental results and therefrom derived conclusions are certainly strongly dependent on the quality of the underlying samples. The growth of a new system of materials in our group was therefore one of the first aims within this thesis. Single crystals of different misfit layered compounds were produced by a chemical vapor transport (CVT) technique that is described in the following Chapter 4.1. Before studying their physical properties into detail they had to be characterized in view of their structural order, surface properties, the influence of cleavage and their chemical composition. These measurements that are indispensable requirements for further investigations in chapters 6 and 7 will be presented in Chapter 4.3. A second method to grow crystals is the molecular beam epitaxy (MBE) that will be introduced briefly in Chapter 4.2. In contrast to chemical transport techniques it is herewith possible to grow thin films from submonolayers to several nanometer thickness. The characterization of epitaxially grown PbS thin films on TMDC substrates as the first step to build successively misfit compounds will be presented in Chapter 8.

4.1 Chemical vapor transport

Chemical Vapor Transport represents the standard technique to grow crystalline bulk transition metal dichalcogenides (TMDC). All of the single crystals investigated in this thesis were grown by CVT, including transition metal dichalcogenides as substrate crystals and misfit layered compounds. The principle of CVT is sketched in Fig. 4.1 (left).

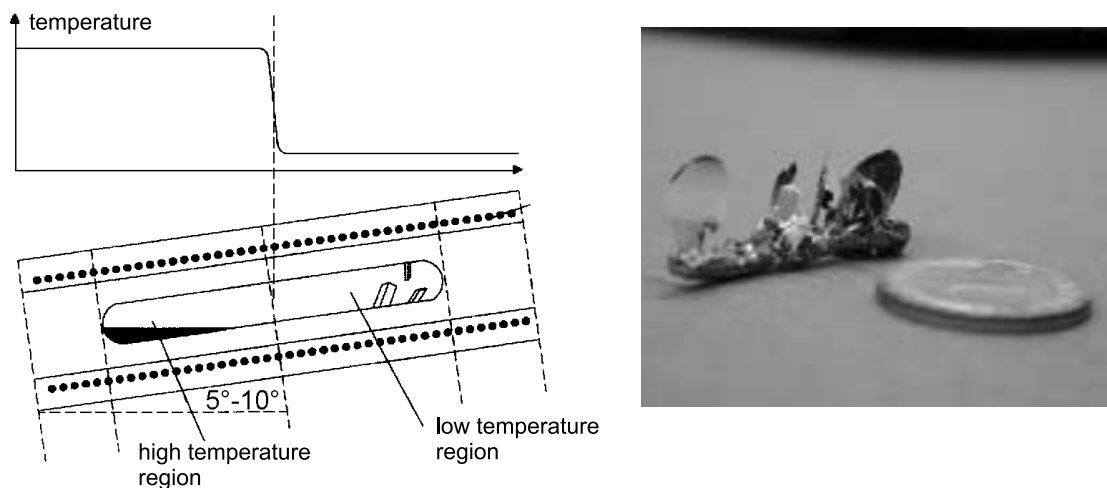


Figure 4.1: *Four-zone furnace for the chemical vapor transport (left). A temperature gradient is established so that the pure components in the high temperature source zone evaporate and grow as single crystals in the low temperature growth zone. Typical samples of the misfit compound $PbS_{1.14}NbS_2$ are shown on the right.*

A stoichiometric amount of the respective pure elements is introduced into a quartz tube with iodine (I_2) as transport agent. The tube is evacuated and sealed and then put into a four-zone furnace. The temperature of the four zones is chosen such that a gradient is established with the source zone on the high temperature side and the growth zone on the low temperature side of the tube. Within 26 days single crystals of the respective TMDC sample are grown after the chemical formula:



with $T = \text{Nb, Ti, W, Ta, Hf}$ and $X = \text{S, Se}$. For the misfit layered compounds new growth parameters had to be found. The best results were obtained with a temperature gradient from 780° to 940° [?]. After Ref. [56] the temperature dependent balance reaction must be adjusted as follows:



with $M = \text{Pb, Sn}$ and $0.08 < x < 0.28$.

In Fig. 4.1 (right) the first misfit layered compounds ever grown in our CVT facility are shown. They exhibit a shining metallic surface that is optically flat and undisturbed. The crystals reach a diameter of nearly 10 mm. Different misfit crystals were grown by CVT with a molar ratio of $m:1.2$ ($m=1,2,3$) for the cations T/M , corresponding to the approximant misfit crystal $(MX)_{1.2}(TX_2)_m$ with an excess amount of sulphur. The successfully grown misfit compounds are listed in Table 4.1 together with the experimental techniques by which they were characterized. Some of these experimental results will be shown in Chapter 4.3.

Sample	Characterization
$(\text{SnS})_{1.16}\text{TaS}_2$	
$(\text{PbS})_{1.13}\text{TaS}_2$	ARPES, STM, LEED, XPS
$(\text{PbS})_{1.14}\text{NbS}_2$	ARPES, STM, LEED, XPS, TEM ² , XRD ³ , Laue
$(\text{PbS})_{1.14}(\text{NbS}_2)_2$	ARPES, STM, LEED, XPS
$(\text{SnS})_{1.17}\text{NbS}_2$	ARPES, EDX ⁴
$(\text{SnS})_{1.17}(\text{NbS}_2)_2$	EDX ⁴
$(\text{BiS})_{1.09}\text{NbS}_2$	
$(\text{PbS})_{1.18}\text{TiS}_2$	ARPES, STM, LEED, TEM ² , EDX ²
$(\text{PbS})_{1.18}(\text{TiS}_2)_2$	ARPES, XRD ³ , TEM ² , EDX ²
$(\text{SnS})_{1.20}\text{TiS}_2$	

Table 4.1: Misfit layered compounds that were grown by CVT within this thesis. The means by which they were characterized are given, some of the results will be introduced later.

In this context it is interesting to note, that the growth of trilayer misfit compounds and of misfit compounds containing a semiconducting TMDC were not successful. In the first case the pure materials reacted and crystals were formed, but X-ray diffraction as well as TEM measurements exhibited an unordered stacking of the different layers, although other authors report about their successful growth of trilayer compounds [7]. On the other hand it was never reported about misfit layered compounds built up from semiconducting TMDC as one constituent. Although we tried to grow them with MoS_2 , WS_2 and HfS_2 as TMDC constituent and various growth parameters the starting substances would not react. In Ref. [57] the authors present stoichiometric HfPbS_3 which has formally an appropriate chemical formula, but the crystallographic structure of these crystals is completely different.

²by C. Dieker, E. Spiecker and W. Jäger

³by M. Traving, B. Murphy and J. Stettner

⁴by S. Herzog, A. Gutzmann and W. Bensch

These results are all the more astonishing as it was possible to produce epitaxial layers of PbS on the semiconducting substrate WSe₂. These considerations will be discussed in further detail in Chapter 8.1.

4.2 Molecular beam epitaxy

The second method to grow crystalline samples in this thesis is **Molecular Beam Epitaxy** (MBE). In contrast to the chemical vapor transport MBE is an epitaxial process which allows to produce thin crystalline films on an adequate substrate with dimensions reaching from a submonolayer coverage to several monolayers in a reasonable time. MBE was developed in the early 1970s as a means of growing high-purity epitaxial layers of compound semiconductors [58,59]. Since that time it has evolved into a popular technique for growing III-V and II-VI compound semiconductors as well as several other materials.

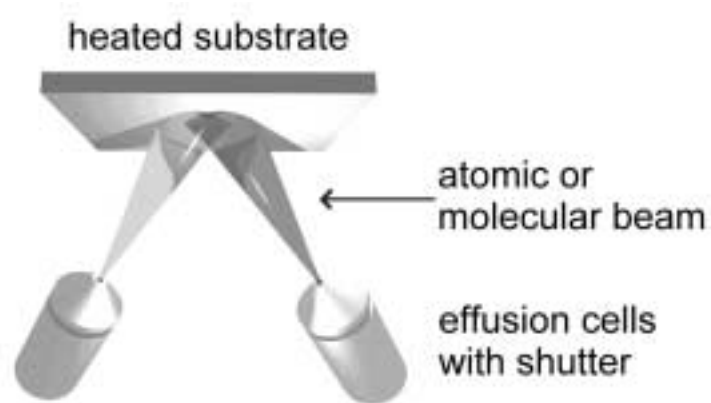


Figure 4.2: *Basic principle of molecular beam epitaxy: atoms or molecules are evaporated from different sources onto a heated substrate, from [49].*

The principle of MBE is presented in Fig. 4.2: Under ultra-high vacuum conditions the constituent materials in the form of molecular beams are deposited onto a heated substrate where they rearrange to form thin crystalline layers. The molecular beams are typically from thermally evaporated elemental sources. A special kind of MBE is the **Van Der Waals Epitaxy** (VDWE) [6,60,61] where a transition metal dichalcogenide is deposited on another or the same TMDC. In contrast to the conventional II-V or II-VI MBE the van der Waals epitaxy has the great advantage that the lattice mismatch between the substrate and the epilayer does not hinder an unstrained epitaxial growth with a low density of defects. While in conventional MBE a lattice mismatch exceeding 1% causes strong disturbances at the interface like strain, structural imperfection and dangling bonds it is possible by means of VDWE to create heterostructures where the lattice mismatch reaches to 58% [62]. Depositing a three-dimensional compound onto a two-dimensional substrate (or vice versa) implies both kinds of epitaxies and is called quasi van der Waals epitaxy, e. g. [63]. All of the described kinds of epitaxy have an equality of surface symmetry of both crystal systems in common which was generally accepted as a requirement for epitaxy. Since there are several known cases where an overlayer changes the symmetry of rotation at the interface a new term has been created recently: "xenotaxy" [64]. These xenotaxially created heterostructures consist of hexagonal epilayers on cubic or rectangular substrates, such as Ag(111)/Si(001) [65], CdTe(111)/GaAs(001) [66] or GaSe(001)/GaAs(100) [67].

With the xenotaxy (this process will be named "epitaxy" in the following anyway) of PbS on TMDC substrates preparations of cubic epilayers on a hexagonal substrate are obtained. These measurements and the resulting consequences for the topography of the PbS layers will be presented in Chapter 8.

4.3 Characterization of the relevant single crystals

As it was mentioned before misfit layered compounds were grown for the first time in our CVT facility. To ensure their correct stoichiometry, the stacking order and the orientation of both subsystem layers with respect to each other within the layer plane different experimental techniques were performed.

Bulk structure of misfit compounds

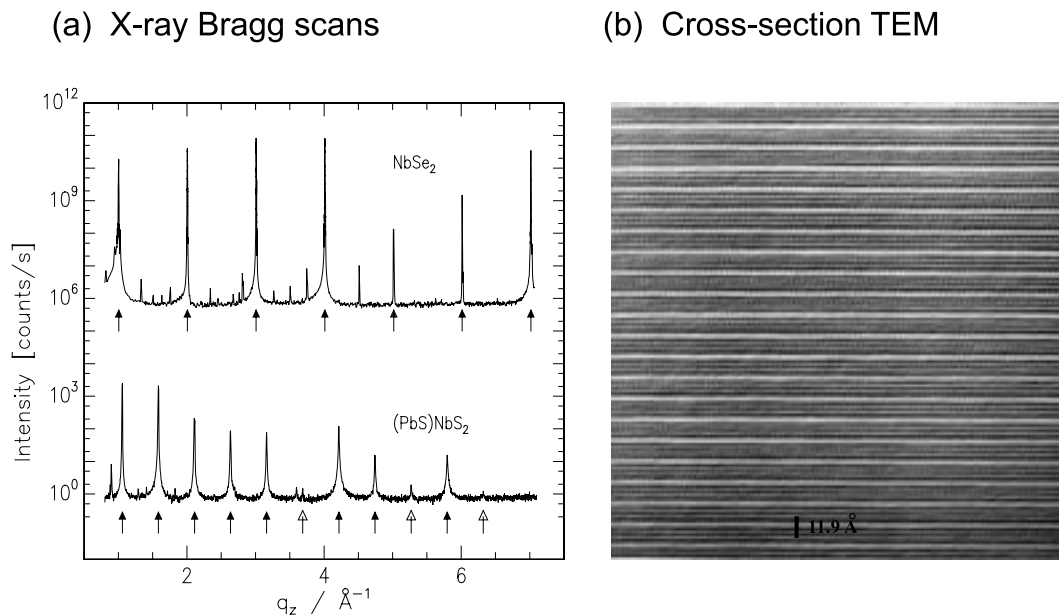


Figure 4.3: (a) X-ray Bragg scans (logarithmic intensity scale) of a single crystal NbSe_2 (upper curve) and a $(\text{PbS})_{1.14}\text{NbS}_2$ crystal (lower curve, shifted). The arrows mark the positions of the Bragg peaks caused by the periodicity of neighboring NbSe_2 and PbS layers respectively. (b) High resolution lattice TEM image of a cross-section specimen of the $(\text{PbS})_{1.14}\text{NbS}_2$ compound. The average periodicity is indicated by the scale marker. Projected view parallel to the misfit layers. (from Ref. [68])

In order to characterize bulk properties particularly the stacking sequence of the misfit compounds X-ray diffraction experiments were performed⁵ with well-collimated $\text{CuK}\alpha_1$ radiation ($\lambda = 1.54056 \text{\AA}$) of a rotating anode. The microscopic structure of the misfit compound layer structure has been investigated⁶ by lattice imaging of cross-section samples using a Philips CM30 electron microscope at 300 kV.

⁵Collaboration with M. Traving, B. Murphy and J. Stettner, DFG Forschergruppe 412/21

⁶Collaboration with C. Dieker, E. Spiecker and W. Jäger, DFG Forschergruppe 412/21

X-ray diffraction Bragg-Scans perpendicular to the layers with $Q = (0, 0, q_z)$ exclusively yield information about the crystalline structure projected onto the c -axis with an information depth of the order of some μm . Fig. 4.3 (a) shows measurements for the misfit layer compound $(\text{PbS})_{1.14}\text{NbS}_2$ (lower curve) and, for comparison, the chalcogenide layer sample NbSe_2 (upper curve). The most intense peaks of each measurement, marked by arrows, are equally spaced and related to a typical distance d_z . The comparison of the two series of peaks reveals that the vertical periodicity of the misfit layer compound is approximately twice that of NbSe_2 . For NbSe_2 the resulting value $d_z = 6.264 \pm 0.005 \text{ \AA}$ is close to the distance of neighboring NbSe_2 layers of the 2H polytype [69]. However, additional much weaker peaks indicate the presence of stacking with larger periodicity, probably different polytypes. Because the scattering of the misfit compound is dominated by the PbS contribution [70], the obtained peaks in the lower curve of Fig. 4.3 (a) yields the spacing between neighboring PbS units with $d_z = 11.92 \pm 0.03 \text{ \AA}$. This value is in agreement with $c_{\text{PbS}} = 11.90 \text{ \AA}$, which is the c -axis of the PbS sublattice for $(\text{PbS})_{1.14}\text{NbS}_2$ ('PbNbS₃') determined by G. A. Wiegers et al. [24, 70, 71] who found a single NbS_2 layer sandwiched between two PbS units. Again, additional weak peaks signal small contributions of multilayered compounds [31, 72] and different polytypes.

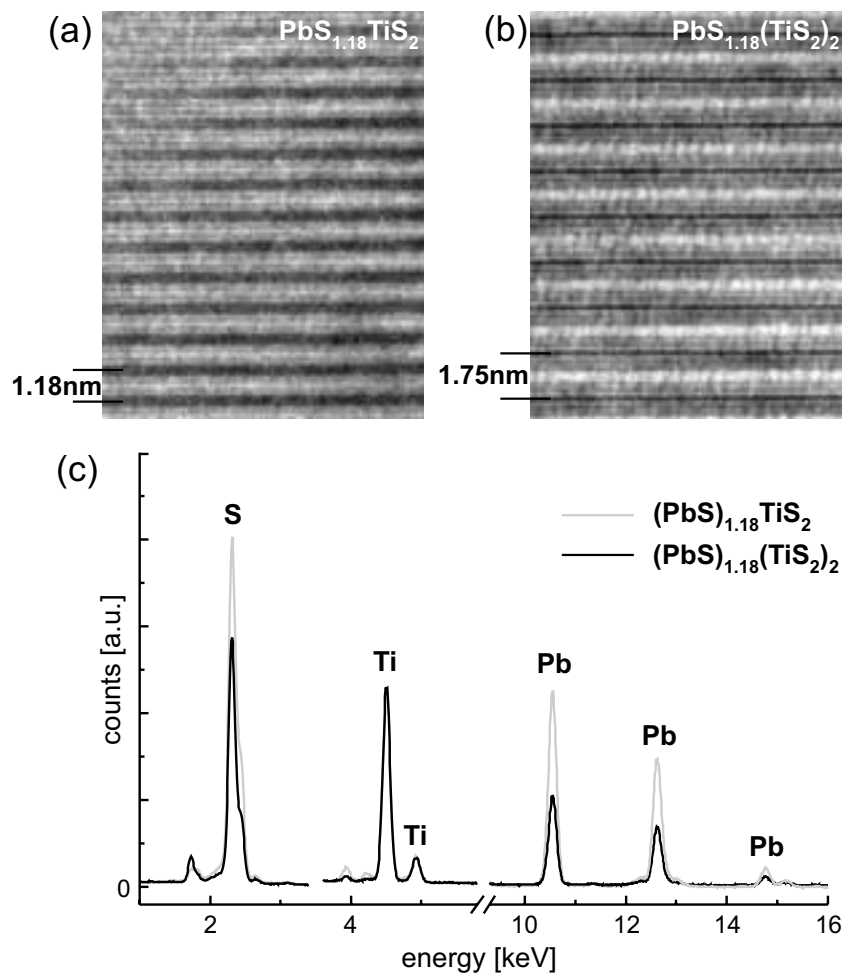


Figure 4.4: High-resolution lattice images of cross-section TEM samples of (a) $(\text{PbS})_{1.18}\text{TiS}_2$ and (b) $(\text{PbS})_{1.18}(\text{TiS}_2)_2$, (c) energy-dispersive X-ray microanalysis spectra of both misfit compounds (from [73]).

Investigations of the microscopic structure of the same misfit layer compound sample by high-resolution transmission electron microscopy show in agreement with X-ray experiments that a large fraction of the sample exhibits a high degree of structural perfection. As example, Fig. 4.3 (b) shows a high-resolution lattice image of a cross-section specimen. The layer stacking has an average periodicity of 11.9 Å, which also equals the value c_{PbS} obtained by G. A. Wiegers et al.

In Chapter 7.1 it was useful to investigate a bilayer misfit compound $(PbS)_{1.18}(TiS_2)_2$ in order to compare it to the corresponding monolayer compound. Therefore both samples were characterized by means of high-resolution TEM cross-section lattice images [73]. Both compounds reveal the same structural perfection as the NbS_2 containing misfit compound and are shown in Fig. 4.4 (a) and (b). The determination of the lattice constants c perpendicular to the layers is in accordance with Ref. [7] and reflect the number of TiS_2 layers between the PbS layers. The atomic ratio of the different constituting elements has been measured by energy-dispersive X-ray microanalysis (EDX) for both components in Fig. 4.4 (c). The spectra were normalized to a common Ti peak height. Thus we can clearly observe a 2:1 ratio of the Pb peaks as it is expected from the chemical compositions of both compounds $(PbS)_{1.18}TiS_2$ and $(PbS)_{1.18}(TiS_2)_2$. In addition, the spectrum verifies the chemical purity of the investigated samples.

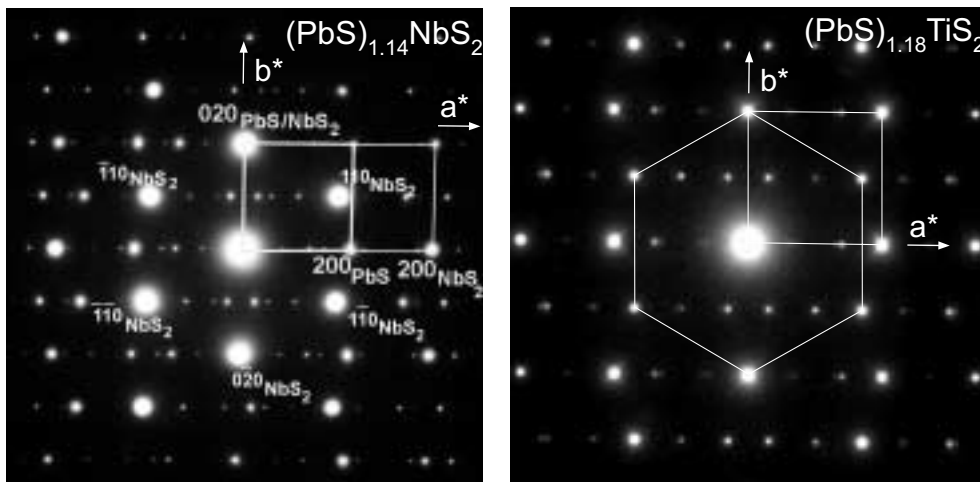


Figure 4.5: Transmission electron diffraction patterns for the misfit layered compounds $PbS_{1.14}NbS_2$ [74] (left) and $PbS_{1.18}TiS_2$ (right, from [73])

The orientation of both subsystems with respect to each other within the layer plane can be determined from plan-view transmission electron diffraction patterns. In Fig. 4.5 measurements are presented for the misfit compounds $PbS_{1.14}NbS_2$ (left) and $PbS_{1.18}TiS_2$ (right). The spots represent a direct image of the reciprocal lattice except for a lack of those reflections, that are extinguished due to diffraction theory. For $PbS_{1.14}NbS_2$ the spots are indexed and the unit cells are indicated, the square belonging to the PbS subsystem, the rectangle to the NbS_2 subsystem. Strictly speaking the unit cells are given with the doubled reciprocal lattice vectors as the lower indexed spots are not visible. Instead of the rectangular unit cell of the TMDC subsystem the hexagonal cell is indicated in the diffraction pattern of $PbS_{1.18}TiS_2$ which is generally used for TMDC although the rectangular one is more convenient for the description of misfit compounds (see Chapter 2.3). Both systems have the main features in common, i. e. the incommensurability between the two

subsystems is clearly revealed along the a^* -axis where the spots lie quasi-dense. Those weak spots in between the main reflections can be attributed to double diffraction involving both subsystems. Both diffraction patterns are consistent with the structure of these compounds as they are described in Ref. [7].

Surface properties of misfit compounds

The surfaces of both the misfit compounds and of the TMDC samples are created by cleavage of the crystals in UHV. Therefore an aluminium post is attached onto the samples before introducing them into the UHV system. There the post is removed mechanically and in case of TMDC samples a very flat surface is produced along the van der Waals gap without surface steps or other defects over several μm [75]. The cleavage planes of misfit layered compounds shall be investigated in the following: Numerous samples of $(\text{PbS})_{1.14}\text{NbS}_2$ have been cleaved and studied by means of scanning tunneling microscopy and low energy electron diffraction.

Two examples are shown in Fig. 4.6. On the left hand side of the figure ((a) - (c)) a cleaved surface is shown that is characterized by several steps that enclose large terraces as can be seen in the large scale STM image (a). A relatively large fraction of PbS is situated at the crystal/vacuum interface. The distinction between PbS and NbS_2 layers results from the shape of the surface steps. It is not possible to draw any conclusions from the height of surface steps, because the thickness of both layers is exactly the same. In the STM image (b) different steps can be seen, some of them having a 90° angle indicating the (001) surface of PbS others with angles of 120° characteristic for the hexagonal NbS_2 (0001) surface. The STM images on the right hand side ((d) and (e)) show a different surface after cleavage. It consists mainly of an undisturbed NbS_2 surface with small islands of PbS (d). The shape of these islands that are enlarged in the lower STM image (e) seem to be significant for the cleavage of misfit compounds. They have been observed for each $(\text{PbS})_{1.14}\text{NbS}_2$ sample that was cleaved and studied by STM within this thesis. If one looks very closely at the STM image in Fig. 4.6 (a) this kind of island can also be seen in the upper right part of the image. The LEED patterns in the lower part of the figure confirm the dissimilarity of the PbS coverage of different cleaved surfaces. While for the sample with a low PbS coverage on the right hand side only the hexagonal pattern of the NbS_2 subsystem is observed, additional weak spots can be seen in the LEED measurement for the sample with a relatively high PbS coverage. They are marked with white arrows. Comparing this pattern to the transmission electron diffraction pattern in Fig. 4.5 (left) the additional spots can be attributed to the tetragonal PbS subsystem. The geometric surface structure of misfit compounds after cleavage in UHV reflects directly the different properties of the two constituent subsystems. After [29] the NbS_2 part is the more rigid one of the two subsystems while the monochalcogenide part is slightly compressed e. g. by 2.5% for SnS. Together with the two-dimensionality of the geometric structure of the NbS_2 part it is evident that its sandwich layers are mainly not destructed. The PbS part on the other hand exhibits a clear three-dimensional character. There is no preference direction (as e. g. a van der Waals gap) for cleavage and the layers are therefore not kept intact.

Although the results just presented suggest the dissimilarity of the PbS coverage of different cleaved surfaces it should be noted that photoemission measurements are not affected. Similarly to STM measurements also ARPES studies have been repeated several times for different samples (not shown). The spectra exhibited the same properties for all samples,

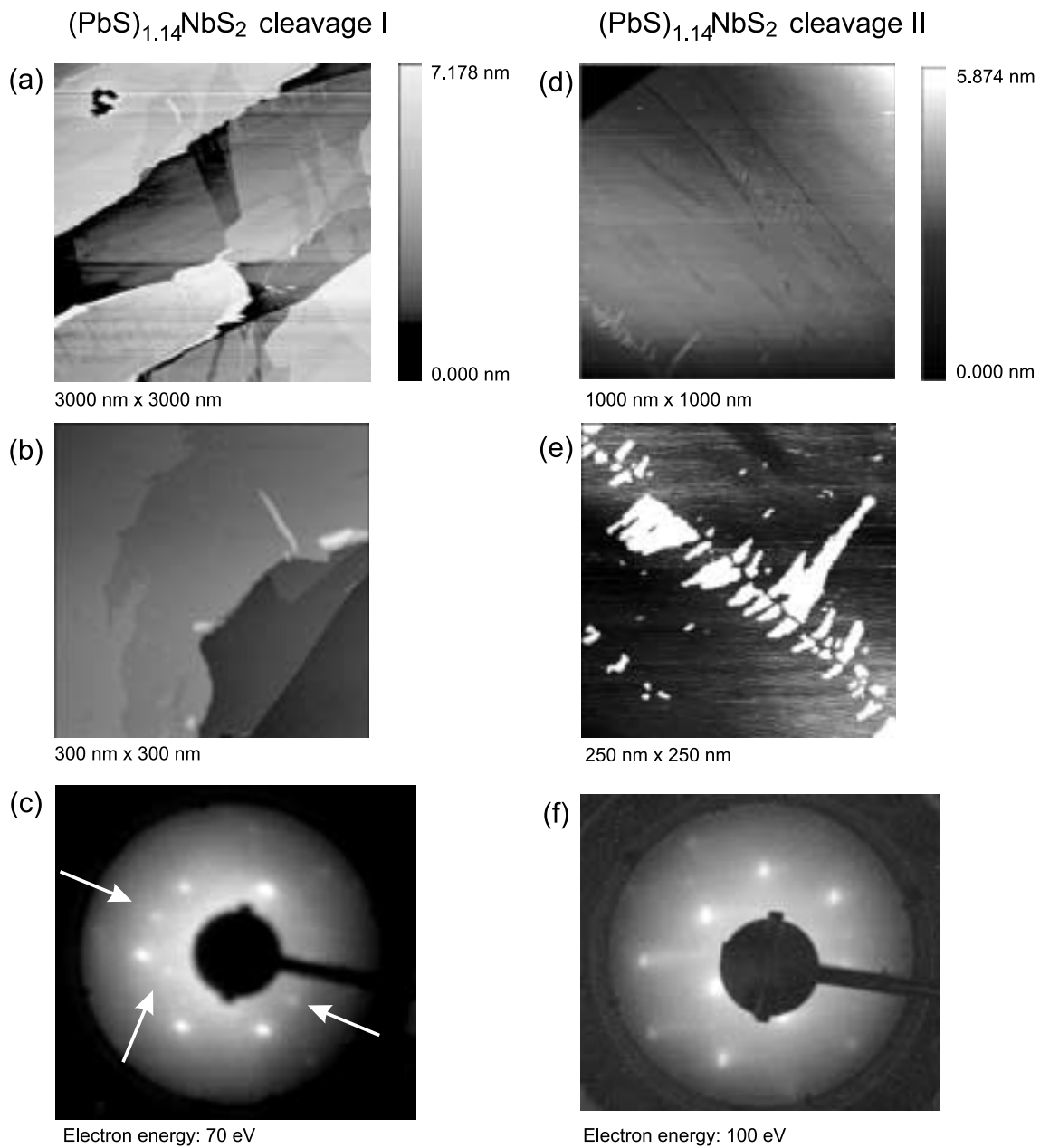


Figure 4.6: Surface structure of two different samples of $(\text{PbS})_{1.14}\text{NbS}_2$ after cleavage. The STM images were measured with the following parameters: (a) $U_{\text{gap}}=2.15$ eV, $I_t=0.38$ nA (occupied states), (b) $U_{\text{gap}}=1.85$ eV, $I_t=0.38$ nA (occupied states), (c) $U_{\text{gap}}=1$ eV, $I_t=1$ nA (occupied states), (d) $U_{\text{gap}}=0.84$ eV, $I_t=0.21$ nA (occupied states). (e) and (f) show the respective LEED patterns.

there was no evidence for an influence of different cleavages.

The chemical composition and purity of misfit layered compounds was checked by X-ray photoelectron spectroscopy. Fig. 4.7 depicts an overview of core levels in a XPS spectrum over a large energy range. The spectrum reveals clearly the main peaks of the constituent elements: the Pb 4f, S 2p and Nb 3d doublets that are labelled in the figure have a high photoionization cross section for the used excitation energy of $h\nu = 600$ eV. The other peaks that are indicated belong to the S 2s and Nb 3p core levels while the peaks at still higher

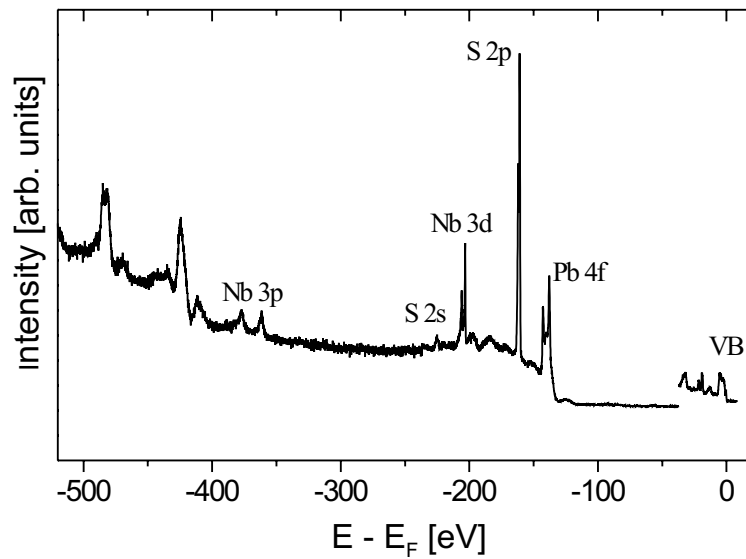


Figure 4.7: X-ray photoemission spectrum for the chemical analysis of the misfit compound $(\text{PbS})_{1.14}\text{NbS}_2$. The part of the spectrum at higher binding energies (below -40 eV) is excited with photons of energy $h\nu = 600$ eV. The part close to the valence band (above -40 eV) is measured with $h\nu = 300$ eV and multiplied by a factor of 6. The main emissions are labelled by the corresponding core level.

binding energies can be attributed to Auger processes that will not be considered here. The part of the spectrum at lower binding energies ($-40 \text{ eV} \leq E - E_F \leq 0 \text{ eV}$) is measured with a photon energy of 300 eV because the photoionization cross section of the valence band decreases dramatically with higher photon energies. Nonetheless it was necessary to multiply the count rate by a factor of 6 in order to visualize the emission structures in this energy range. Over the whole energy range no contributions from impurities could be observed as e. g. iodine (originating from the growth process (CVT)), nitrogen, oxygen or carbon. The purity of several different misfit samples was also confirmed for the bulk by energy dispersive X-ray microanalysis (EDX)⁷.

Characterization of the natural mineral galena (PbS)

For the measurements on PbS single crystals as well as for the epitaxy natural galena crystals [76] were used. They had to be characterized before. Fig. 4.8 (a) shows a typical surface of a PbS sample that was cleaved in UHV as it was described above. In contrast to TMDC and also misfit compound surfaces the cleavage plane of PbS is characterized by several surface steps that form a rectangular pattern. The steps are clearly revealed in the height profile below. The LEED pattern in Fig. 4.8 (b) indicates clearly the perfection and structural order of the cleavage plane of PbS, the sharp spots form a regular quadratic pattern that belongs to the unreconstructed (001) surface. The chemical purity of the natural mineral is particularly important for the purpose of using it as evaporation material in MBE. First attempts were made with synthetic high-purity PbS powder. Since it could not be evaporated in a controlled manner in the form of a powder it was pressed into pellets.

⁷Collaboration with S. Herzog, A. Gutzmann and W. Bensch, DFG Forschergruppe 412/21

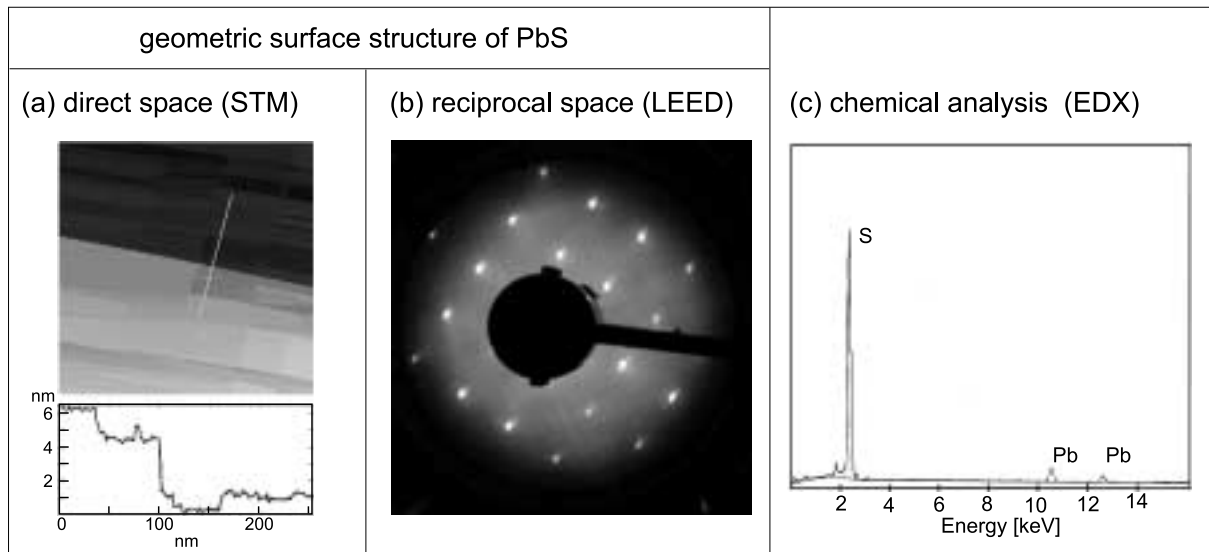


Figure 4.8: (a) STM image of $500 \times 500 \text{ nm}^2$ from occupied states ($U_{\text{gap}}=0.68 \text{ V}$, $I_t=0.2 \text{ nA}$) and height profile along the white line. (b) LEED pattern of the (001) surface ($E_{\text{electron}}=100 \text{ eV}$). (c) Energy dispersive X-ray spectrum

But this treatment led to a high density of impurities and the material did not grow stoichiometrically and crystalline on the substrate. Therefore we decided to use natural galena (PbS) crystals for the epitaxy (see Chapter 8) and analysed the chemical composition of the mineral by means of energy dispersive X-ray microanalysis (EDX)⁶ that is sensitive to the bulk. In Fig. 4.8 (c) an EDX spectrum is presented. The peaks are labelled with the originating elements lead and sulphur. No additional peaks that would indicate impurities can be observed. These results were confirmed by repeating the measurement at several spots of different samples. The spectra exhibited always the same peaks.

Comparison of NbS_2 and NbSe_2

Transition metal dichalcogenides and in particular TiS_2 , TaS_2 and WSe_2 grown in the CVT facility described in Chapter 4.1 have already been the subject of detailed studies, see e. g. [45, 48, 77]. New attempts were only made for the purpose of growing 2H- NbS_2 single crystals as one constituent of the misfit compound $(\text{PbS})_{1.14}\text{NbS}_2$. Therefore the characterization of transition metal dichalcogenides will be limited to a comparison of NbS_2 and NbSe_2 .

Fig. 4.9 presents some results from band structure calculations [78] and photoelectron spectroscopy as well as LEED. Regarding the theoretical band structures of both compounds it is obvious that the electronic structure is altered only to a minor extent. Especially the region around the Fermi level is very much alike. The niobium derived bands are unoccupied at the Γ point and pass the Fermi energy in both directions ΓM and ΓK . At the Γ point the Fermi surface is constituted by the sulphur derived p_z band that is highly dispersive in the direction perpendicular to the layers ΓA . The photoelectron spectra in Fig. 4.9 (b) are both measured in normal emission with an excitation energy of $h\nu=21.2 \text{ eV}$. Although the same structures are expected from the theoretical band structure explicit deviations in the photoemission spectra can be observed. The high background for NbS_2 indicates defects of the structural order that give rise to inelastically scattered electrons. Other changes like the

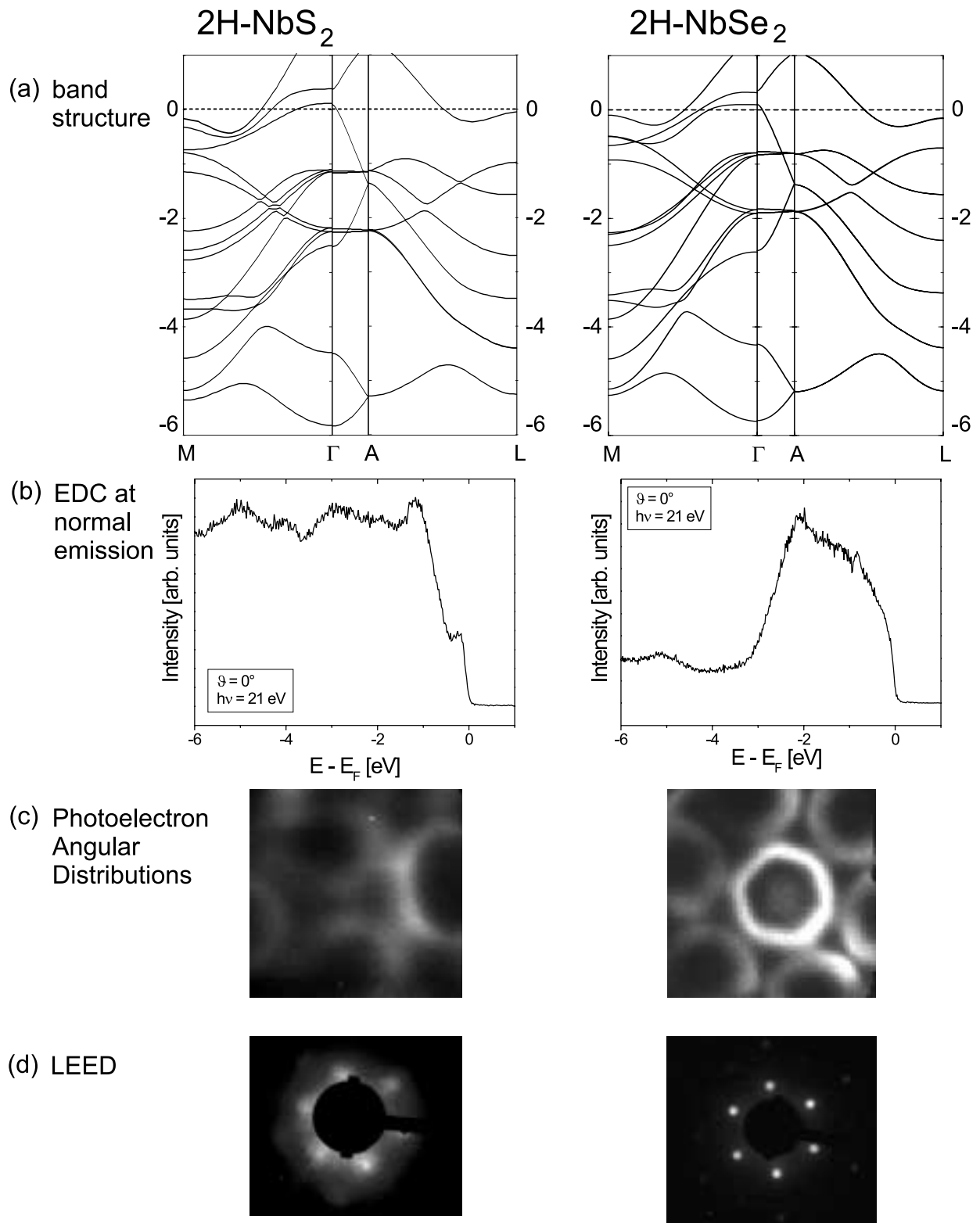


Figure 4.9: Comparison of NbS_2 with NbSe_2 : (a) band structure calculations from [78], (b) normal emission photoelectron spectra, (c) photoelectron angular distribution images near the Fermi energy excited with $h\nu=21.2$ eV (NbS_2) and $h\nu=24.5$ eV (NbSe_2), the PAD for NbSe_2 is taken from [39], (d) LEED patterns ($E_{\text{electron}}=121$ eV for NbS_2 and $E_{\text{electron}}=100$ eV for NbSe_2)

dip at a binding energy of $E-E_F \approx -0.5$ eV will be discussed in further detail in Chapter 7.2 where it is ascribed to a weak self-intercalation of NbS₂.

Nevertheless, the samples are crystalline to a sufficient high degree to draw conclusions from ARPES measurements. The photoelectron angular distribution (PAD) images presented in Fig. 4.9 (c) show clearly for NbSe₂ as well as for NbS₂ the hexagonal symmetry of the electronic structure. Taking into account that the center of the Brillouin zone of NbS₂ is close to the right edge of the image both PAD measurements are mostly alike.

The hexagonal symmetry is also reflected in the geometric structure as it can be seen in the LEED patterns in Fig. 4.9 (d). Although the spots are rather broad for NbS₂ they clearly form a hexagon which indicates a sufficient high degree of orientational order of the surface. In the context of other results of the DFG Forschergruppe on "Growth and interface properties of sulphide and selenide layer systems" it is likely that the samples consist of small crystallites that are tilted by angles less than 0.1° with respect to each other [79]. These small angles are well below the angular acceptance of the photoemission experiment and therefore not relevant for our measurements.

5 The electronic structure of PbS

Lead sulphide PbS is one of the constituents of the misfit layered compounds that will be studied in the following chapters. For the investigation of misfit layered compounds as well as epitaxial thin films of PbS on transition metal dichalcogenide substrates it is essential to achieve a profound knowledge of the properties of their subsystems. Although a systematic investigation of the electronic structure of PbS already began in early times of photoelectron spectroscopy some questions remain that are not answered completely yet or have never been considered. Probably the most prominent one concerns the electronic transitions that are responsible for the peaks in photoemission spectra. In order to solve this problem PbS served as a model system [18, 80] and will further be discussed in the following.

In Chapter 3.1 an overview over photoemission theory was given under the assumption of direct transitions between initial and final states. Then the perpendicular component of the momentum of the photoelectrons depends on the excitation energy of the photons: $\mathbf{k}_{f\perp} = \mathbf{k}_{i\perp}(\hbar\nu)$. Nevertheless it is not self-evident that the k_{\perp} component is conserved when the electrons are transmitted through the surface into the vacuum. In Ref. [80] the opposite assumption leads to the **One-Dimensional Density of States (ODDS)** model that was tested and verified for the (001) surface of PbS. Within this model the conservation of the k_{\perp} component is totally neglected. Peaks in photoemission spectra are assigned to singularities in the one-dimensional density of states:

$$I(E, \mathbf{k}_{\parallel}) \sim [dE_v(\mathbf{k}_{\parallel,v}, k_{\perp,v})/dk_{\perp,v}]_{E_v=\hbar\nu-E}, \quad (5.1)$$

where $\mathbf{k}_{\parallel,v}$ ($k_{\perp,v}$) is the crystal momentum of a valence-band state parallel (perpendicular) to the surface, \mathbf{k}_{\parallel} is the corresponding component of the photoelectron momentum and E_v the energy with respect to the vacuum level of the valence-band state. To obtain the total photocurrent equation 5.1 must be summed over all valence bands under consideration. In addition this model implies that the transition probability is only weakly dependent on energy. It can happen, however, that no final states are available for the transitions and the transition probability is zero; in this case, the corresponding structure in the photoemission spectra is not visible. One year later the same authors extended their model to the "weighted -indirect-transition model" [18] which contains the direct transition model as well as the ODDS model as limiting cases. Both singularities in the one-dimensional density of states and direct transitions may give rise to peaks in photoemission spectra.

In Ref. [81] normal emission as well as off-normal emission data of the (001) surface of PbS were measured and interpreted within the direct-transition model as it was described in Chapter 3.1. The authors conclude that no need exists to invoke indirect transitions for the interpretation of their spectra and that the direct-transition model is even superior to the ODDS model, since the latter fails to account for the normal emission data.

In order to decide which of both models is applicable to PbS it is worthwhile to reinvestigate the photon energy dependence of photoemission spectra in normal emission. In the case of direct transitions peaks should move systematically with the photon energy reflecting the dispersion of the initial states (Eq. 3.6). If on the other hand the peaks are due to singularities in the one-dimensional density of states they appear at the same binding energy, no matter which photon energy is employed. Obviously the differentiation is not possible if the sample under investigation does not exhibit dispersing states in the direction perpendicular to the surface. Therefore PbS is chosen in Refs. [18,80] as a three-dimensional

crystal in contrast to e. g. transition metal dichalcogenides which show two-dimensional properties (see Chapter 2). The three-dimensional character of the electronic structure can be seen from scalar-relativistic band structure calculations of PbS in Fig. 5.1 [78].

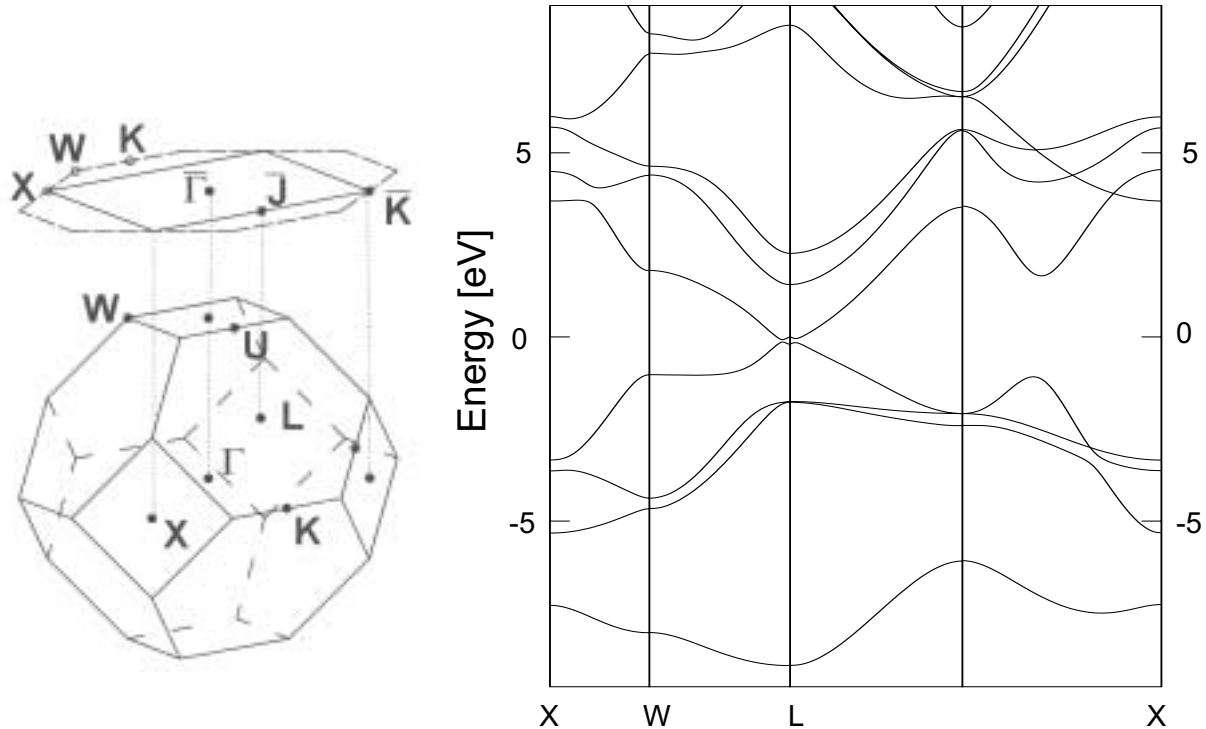


Figure 5.1: Brillouin zone and surface Brillouin zone of the (001) surface of PbS with the points of high symmetry (left) and scalar-relativistic band structure calculation of PbS from [78] (right)

In addition the bulk Brillouin zone with the points of high symmetry corresponding to the directions appearing in the calculation is depicted as well as the surface Brillouin zone of the (001) surface of PbS which represents the geometric setup of the subsequent measurements. The theoretical band structure clearly reveals both the valence band maximum and the conduction band minimum at the L point. Therewith it is in contrast to II-VI semiconductors where the direct band gap is located in the center of the Brillouin zone (Γ point). This anomalous behavior is explained in Ref. [82] by the occurrence of the Pb s band below the top of the valence band, setting up coupling and level repulsion at the L point. Furthermore we can observe strongly dispersive bands along all directions of the Brillouin zone indicating the three-dimensional character of the electronic structure of PbS. In particular the directions XW and Γ X are concerned which represent the directions perpendicular to the (001) surface. In the following we will emphasize on the direction Γ X, since it corresponds to normal emission ARPES measurements which are presented in Fig. 5.2. The data is normalized to the light intensity and the total time of measurement. The spectra are dominated by a very intense peak at a binding energy of $E - E_F \approx -1.6$ eV that remains dispersionless throughout the whole range of photon energies. In Ref. [81] this peak is ascribed to a surface state due to its dispersionless character. The emission structures at higher binding energies are much lower in intensity. Therefore the spectra are shown once more smoothed by averaging over five neighboring data points and with a stretched intensity axis.

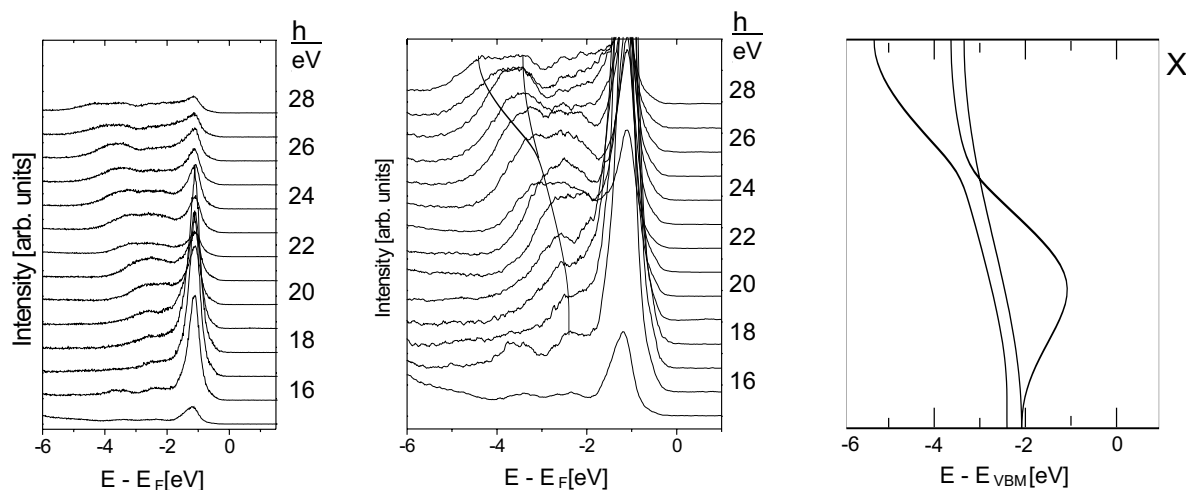


Figure 5.2: Energy distribution curves of the (001) surface of PbS in normal emission and varying photon energies. The overall energy resolution was chosen to $\Delta E=60$ meV. The intensity axis is stretched by a factor of five at the middle panel with respect to the left panel and the spectra are smoothed by averaging over five data points. On the right the theoretical band structure is shown along the ΓX direction.

In this representation the weaker features at binding energies between -2 eV and -5 eV can be studied and compared to the theoretical band structure. Clearly an electronic state can be identified that disperses from $E - E_F \approx -2.4$ eV at $h\nu = 16$ eV to higher binding energies $E - E_F \approx -4.4$ eV at $h\nu = 28$ eV. At $h\nu = 23$ eV a second state can be distinguished that is lowered in binding energy only to $E - E_F \approx -3.6$ eV. These bands are marked in the experimental data set by black lines and are in very good agreement with the theoretical band structure along ΓX , only the lowest band does not disperse to as low binding energies as in theory within the measured photon energy range. It is very likely that the dispersion proceeds to higher photon energies. The third band that is seen in the band structure calculation is not so easy to be identified in the photoemission spectra because it is hidden by the strong peak arising from the surface state at $E - E_F \approx -1.6$ eV. Nevertheless we can observe weak shoulders at the lower energy side of this peak at $E - E_F \approx -2.0$ eV for $h\nu = 19$ eV and $h\nu = 20$ eV. In Ref. [81] this energy region was fitted with two peaks, one of them following the theoretical band in very good agreement while the other remains stationary upon changing the photon energy. Altogether those results concerning normal emission ARPES can precisely be confirmed by our measurements.

But on the other hand the discrepancies that led to the ODDS model were observed in off-normal emission [80]. Therefore we mapped both high symmetric directions of the surface Brillouin zone of the (001) surface $\bar{\Gamma}\bar{J}$ and $\bar{\Gamma}\bar{K}$ in Fig. 5.3. These spectra were measured with a constant photon energy of $h\nu = 21.22$ eV and an energy resolution of $\Delta E = 60$ meV. In order to compare these experimental results to theoretical calculations some relations between surface and bulk Brillouin zone have to be noted (see Fig. 5.1): The $\bar{\Gamma}\bar{J}$ ($\bar{\Gamma}\bar{K}$) direction originate from the projection of the ΓL (ΓX) line onto the (001) surface Brillouin zone and correspond to the crystallographic directions $[010]$ ($[100]$). Therefore the experimental data is compared to the calculated band structure along ΓL and ΓX on the one hand. These directions correspond to a well defined component of the wave vector

of the electrons perpendicular to the surface (e. g. $k_{\perp}=0$ in the case of $\bar{\Gamma}\bar{K}$). Actually this assumption is not justified since the perpendicular component of the wave vector remains undetermined within the photoemission process assuming direct transitions. But in Ref. [18, 81] it can be seen that the surface parallel dispersion is barely affected by a variation of the photon energy. On the other hand the experimental data is compared to the one-dimensional density of states along these lines. It was calculated by keeping the parallel component of the wave vector constant and summing the initial states over all irreducible points of the Brillouin zone in the direction perpendicular to the surface according to Equation 5.1 [78].

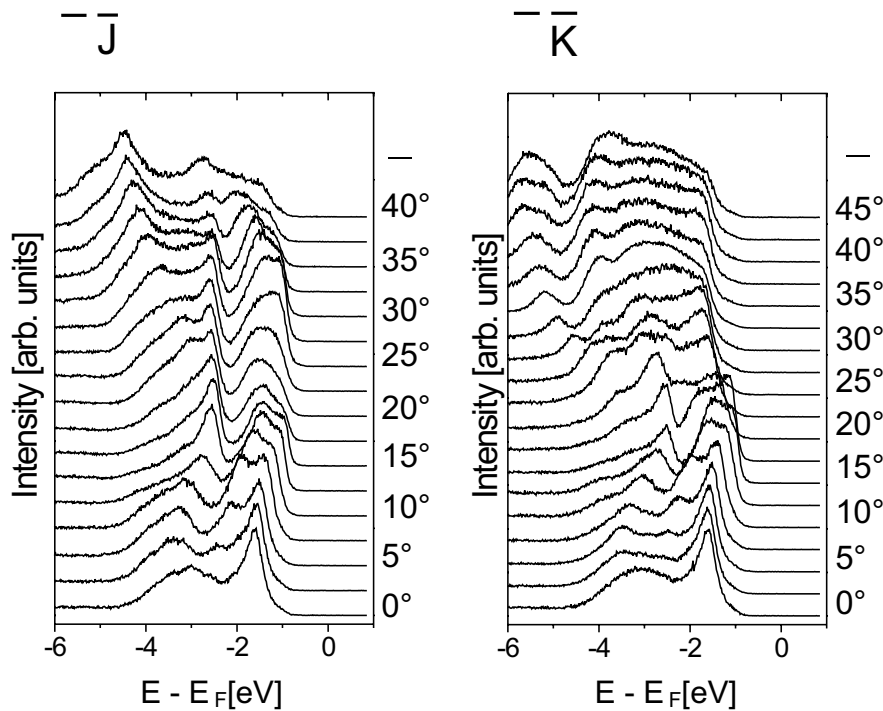


Figure 5.3: Energy distribution curves of the (001) surface of PbS along $\bar{\Gamma}\bar{J}$ and $\bar{\Gamma}\bar{K}$ measured with a photon energy of $h\nu=21.22$ eV. The overall energy resolution was chosen in all spectra to $\Delta E=60$ meV.

The results of this comparison are depicted in Fig. 5.4 for the directions $\bar{\Gamma}\bar{K}$ (a) and $\bar{\Gamma}\bar{J}$ (b). The experimental photoemission spectra from Fig. 5.3 are presented on the left as grey scale images where white belongs to high photoelectron intensity. The images are deformed according to Equation 3.5 in order to obtain the experimental band structure $E(\mathbf{k}_{\parallel})$. On the right hand side the theoretical one-dimensional density of states is presented as grey scale images for the same energy and \mathbf{k}_{\parallel} range as well. Both images are overlaid by the theoretical band structure in the directions $\bar{\Gamma}X$ (a) and $\bar{\Gamma}L$ (b) as white lines. Thus it is possible to find the deviations of the one-dimensional density of states from the band structure at well defined k_{\perp} first and then to decide which of both models (direct transitions or ODDS) is in better agreement with the experimental results.

In the right images some of the peaks in the one-dimensional density of states follow closely the initial state bands. But there are several more peaks that have no counterpart in the band structure along $\bar{\Gamma}X$ or $\bar{\Gamma}L$ respectively. The density of states originates therefore from other parts of the Brillouin zone with deviating k_{\perp} . Regarding the experimental

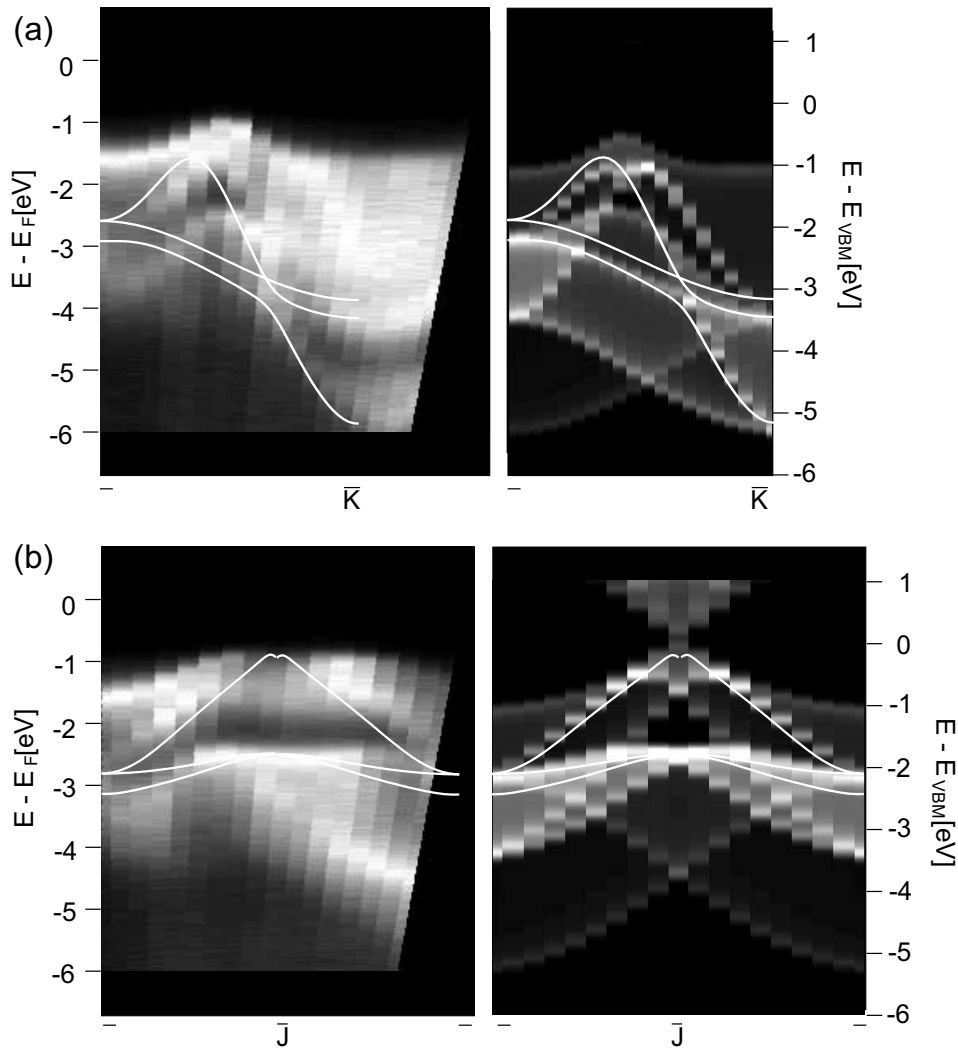


Figure 5.4: Comparison of experimental and theoretical data. On the left the spectra along the $\bar{\Gamma}\bar{K}$ line (a) and the $\bar{\Gamma}\bar{J}$ line (b) of Fig. 5.3 are depicted as grey scale image. The one-dimensional density of states along these lines is presented on the right. In both experimental and theoretical images the calculated bands along ΓX (a) or ΓL (b) are given as white lines.

band structure on the left hand side of the figure we can state a nearly perfect agreement between the experimental data and the peaks of the one-dimensional density of states. Almost every emission structure has its counterpart in the ODDS image while the band structure calculation suffers from a lack of several electronic states that can be observed in the photoemission spectra. However, those bands that are predicted by the theoretical band structure are well reproduced by the experiment in analogy to the correspondencies between the band structure and the ODDS dispersion. Going more into detail we can find some interesting differences between experiment and theory though. In the $\bar{\Gamma}\bar{K}$ direction the structures coincide to a very large extent. The $\bar{\Gamma}\bar{J}$ direction on the other hand exhibits some unexpected properties. The measurements exceed beyond the \bar{J} point and nearly reach the second $\bar{\Gamma}$ point. From band structure theory the first and the second $\bar{\Gamma}$ point are equivalent, this is reflected by the mirror plane along the \bar{J} point in both the band structure calculation and the one-dimensional density of states. The experimental data

reveals the lowest band dispersing from $E - E_F \approx -2.5$ eV at \bar{J} to $E - E_F \approx -4.5$ eV near $\bar{\Gamma}$ in the second Brillouin zone in good agreement to theory. In contrast to theory the band is not to be seen in the first Brillouin zone. A similar effect can be observed at the valence band maximum at the \bar{J} point. We can clearly identify the electronic band that disperses from the $\bar{\Gamma}$ upwards to higher energies but towards the \bar{J} point the emissions loose intensity and the band is not visible any more above $E - E_F = -1.0$ eV. Both effects are not reflected by the theoretical results because they are inherent to the photoemission process. The transition probability depends via the matrix element on the direction of the incoming light with respect to the electron momentum and on the availability of final states (see Chapter 3.1 Eq. 3.2). Therefore certain electronic states can not be observed in ARPES under certain experimental conditions or they are strongly reduced in intensity. Due to the good agreement between photoemission spectra and one-dimensional density of states we can draw conclusions about the energetic position of the valence band maximum with respect to the Fermi level. It should be noted that the energy axes are referenced to the Fermi energy and to the valence band maximum respectively. By fitting experimental and theoretical results we can locate the valence band maximum at an energy of approximately 0.7 eV below the Fermi level ($E - E_F \approx -0.7$ eV). The position of the Fermi level within the band gap of a semiconductor depends on different circumstances, e. g. dopants or surface properties that induce band bending. In both cases the electronic structure should be shifted as a whole and the band gap of $E_{gap} = 0.41$ eV must be conserved. Therefore a band bending can not explain the large shift because it would not exceed an energy corresponding to the band gap. Furthermore a back bending induced by illumination of the sample has not been observed (**S**urface **P**hotovoltage (SPV) effect). However, due to the large energetic shift the conduction band must be occupied by electrons at a binding energy of $E - E_F = -0.3$ eV at the latest.

Since the states that constitute the valence band maximum are strongly decreased in intensity we mapped the $\bar{\Gamma}\bar{J}$ direction a second time with special concern on the energetic range around the Fermi level. The corresponding energy distribution curves are depicted in Fig. 5.5. In the left panel a larger energetic range is shown with the dispersing peak with high intensity that has already been observed in Fig. 5.3. The energetic position of this peak coincides perfectly with the former results. At the \bar{J} point we can discern here the valence band maximum at $E - E_F \approx -0.7$ eV as a weak shoulder of the strong peak. Within the highlighted range around the Fermi level no emissions can be observed. The spectra within this energy range have been strongly smoothed by averaging over ten next data points and the intensity axis has been stretched in the middle panel. Here, we can clearly observe emission features at the Fermi energy around the \bar{J} point that can thus be ascribed to electrons from the conduction band. The spectrum at the \bar{J} point has been measured again with higher count rate in the right panel. A Fermi edge can clearly be recognized here without any manipulation of the original data. An exact determination of the energetic position of the conduction band minimum requires the study of the photon energy dependence of this peak. As we have seen before direct transitions have to be taken into account for discussing normal emission spectra of PbS. Since the direct band gap of PbS is as small as $E_{gap} = 0.41$ eV it is likely that the peak still disperses to lower binding energies in the direction perpendicular to the surface.

In order to decide whether the occupation of conduction band states is a surface effect or whether it is also valid for the bulk we performed optical transmittance measurements in

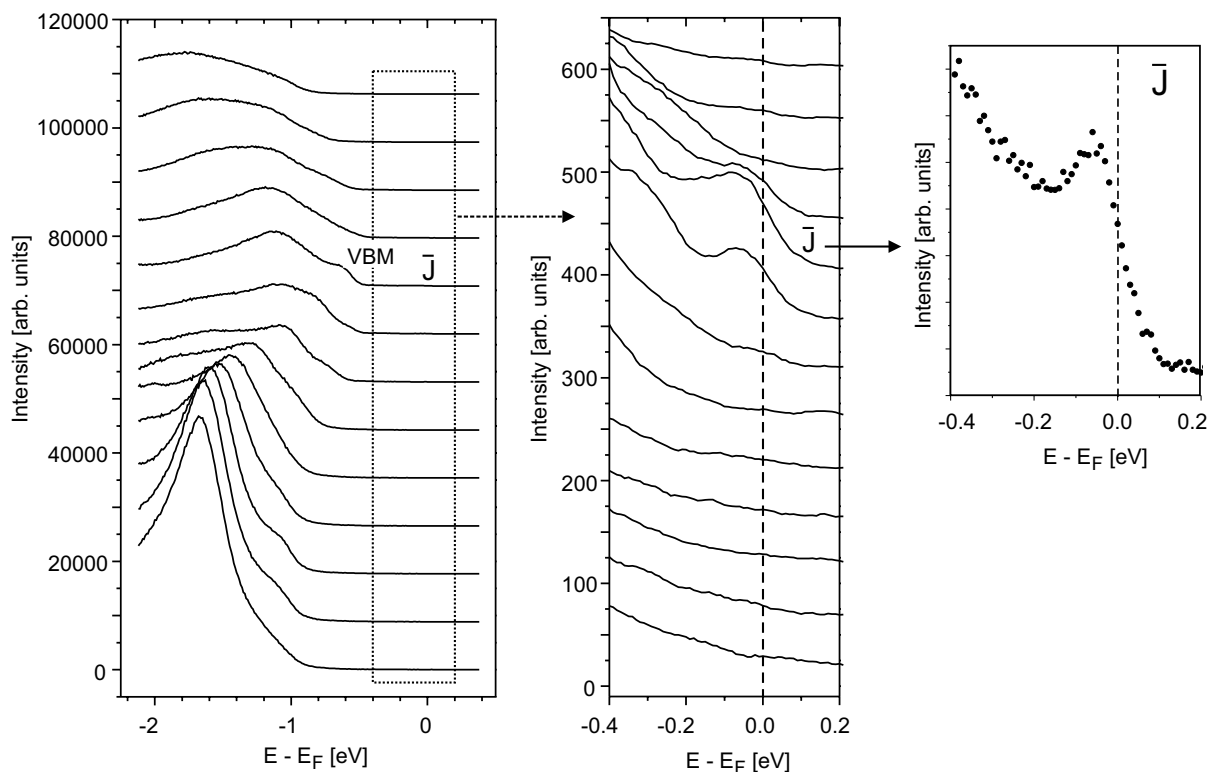


Figure 5.5: Energy distribution curves along the line $\bar{\Gamma}\bar{J}$ of the (001) surface Brillouin zone of PbS. The energetic range close to the Fermi level was strongly smoothed and stretched and is depicted in the middle panel. The spectrum at the \bar{J} point has been measured again with a higher count rate; the original data is shown in the right panel.

the mid-infrared energy range⁸. For this purpose PbS was finely ground and mixed with dry potassium bromide powder. The mixture was then pressed into a pellet and introduced into the measurement facility. The measurement was repeated for a different amount of PbS mixed into the KBr pellet. The results are depicted in Fig. 5.6 (a). The upper curve is measured with a smaller amount of PbS, the transmittance is higher and structures corresponding to the KBr can be distinguished. At energies of approximately 0.20 eV and 0.43 eV we observe dips in the curve that can be ascribed to vibrational modes of water that is incorporated in the KBr. The lower curve is taken for a larger amount of PbS in the mixture. The sample is nearly opaque for light exceeding an energy of 0.15 eV. The KBr spectrum can not be observed any more. In particular at an energy of 0.41 eV that corresponds to the band gap of PbS both curves are smooth and no evidence for an enhanced absorption of light can be seen. In comparison spectra for the III/V semiconductor InAs are shown in Fig. 5.6 (b), again for different amounts of InAs in the InAs/KBr mixture. Especially in the upper curve more structures are revealed. Very clearly we can discern the vibrational modes of water that we know already from the PbS spectra. InAs is a narrow gap semiconductor with a direct energy gap of $E_{gap} = 0.35$ eV at the Γ point [83]. The corresponding energy range is enlarged on the right where we can observe distinct dips in the transmittance spectrum at energies between 0.35 eV and 0.36 eV that correspond to

⁸Collaboration with U. Cornelissen and F. Tuzek, DFG Forschergruppe 412/21

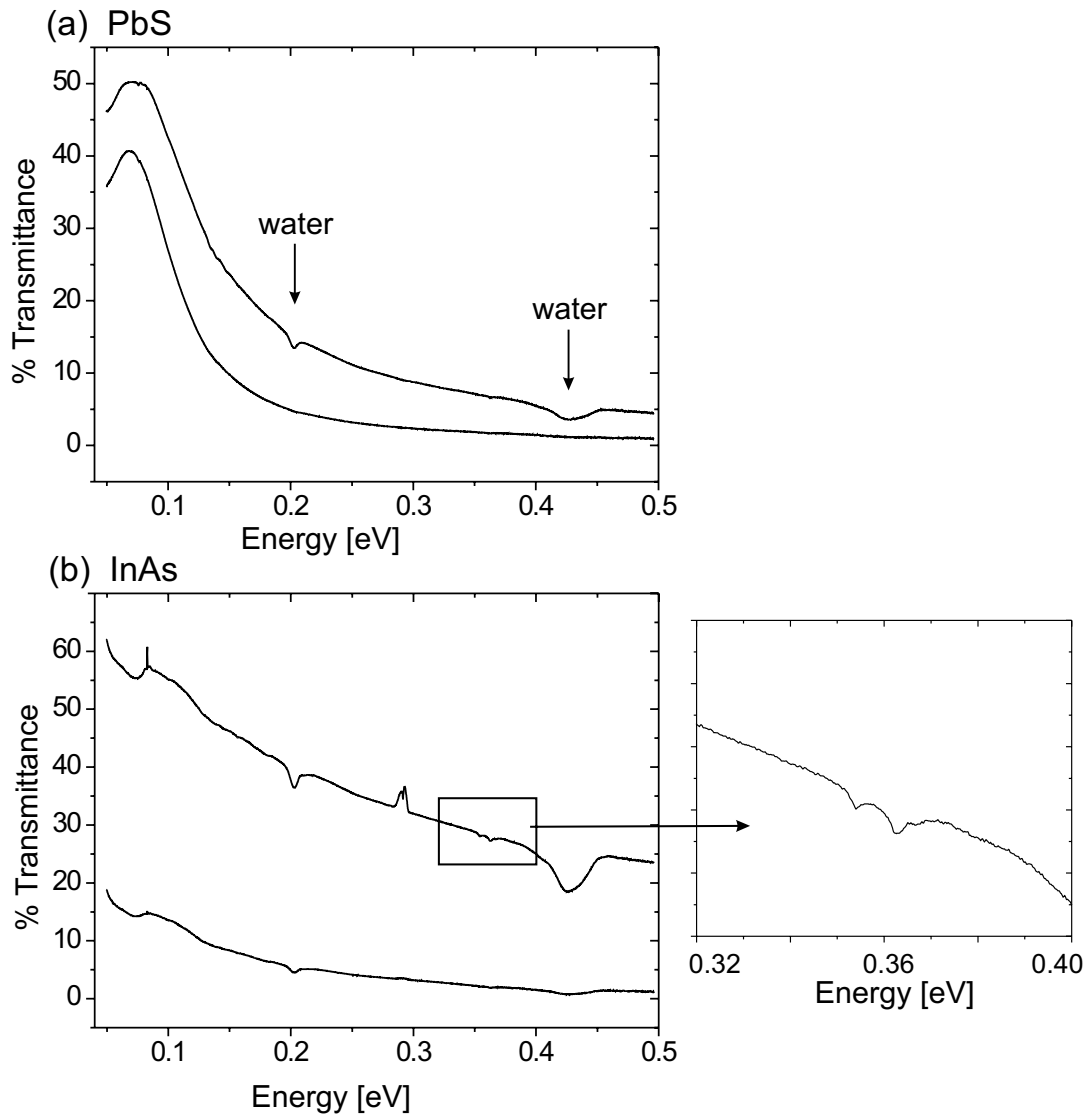


Figure 5.6: Mid-infrared transmittance spectra of (a) PbS and (b) InAs. The upper curves correspond to smaller amounts of PbS or InAs respectively. For InAs the energetic region around the band gap at 0.35 eV is enlarged on the right.

an energy where electrons can be excited by the infrared radiation over the band gap into unoccupied states in the conduction band. This is in contrast to the measurements on PbS where no structures in the spectra could be found that are connected to the band gap at 0.41 eV. Obviously photons with energies below the band gap can be absorbed by the PbS sample. This observation is in accordance to the assumption of the conduction band being partly occupied by electrons also in the bulk.

Surface sensitive photoemission measurements as well as bulk sensitive infrared spectroscopy measurements show an occupation of the conduction band minimum of PbS making it a degenerate semiconductor. The bulk sensitive optical measurements prove that this is not a surface induced effect but it is valid in the bulk as well. Furthermore, we can exclude this effect to be present only in our natural galena crystals, since all known photoemission measurements on natural PbS samples [18, 84–86] as well as on synthetically grown crystals [81, 87] are in perfect agreement with our photoemission results. In Ref. [84] a shift of

the spectra by $\Delta E=0.8$ eV to lower binding energies relative to the valence band maximum was recognized and attributed to a charging of the sample due to an inadequate sample contact. With our results we can now negate this explanation.

Conclusions

We investigated the electronic structure of natural PbS single crystals by means of angle-resolved photoelectron spectroscopy. We found dispersing bands in the direction perpendicular to the PbS (001) surface that coincide with calculated bands in the ΓX direction. These findings are inconsistent with the simple ODDS (one-dimensional density of states) model for electronic transitions that was introduced by Grandke et al in 1977 [80]. However, photoelectron spectra in normal emission are dominated by a strong peak that is associated with a surface state at an energy of $E - E_F \approx -1.7$ eV. Going to off-normal photoemission measurements we found convincing agreement between experimental results and one-dimensional density of states calculations. Contrarily, taking only initial states at defined k_{\perp} into account, i. e. assuming direct transitions under the conservation of the k_{\perp} component of photoelectrons, several emission features in the photoemission spectra could not be explained. These findings prove the failure of the direct transition model that neglects other transitions than direct ones. An appropriate model was presented by Grandke et al in 1978 [18]: the weighted ODDS model. This model implies that both singularities in the one-dimensional density of states and direct transitions may give rise to peaks in photoemission spectra. They showed that direct transitions are most important in normal emission while the relevance of the one-dimensional density of states increases to off-normal emission. These predictions are precisely verified by our measurements.

Due to the perfect agreement between experiment and theory we could determine the position of the valence band maximum at an energy of 0.7 eV below the Fermi level. Since the band gap of PbS at room temperature is as small as $E_{gap} = 0.41$ eV it is evident that the conduction band must be occupied turning PbS into a degenerate semiconductor. Despite the strongly decreased intensity of conduction band electrons we could clearly reveal occupied electronic conduction band states just below the Fermi level at the \bar{J} point. The electronic occupation of the conduction band was confirmed by transmittance spectroscopy in the mid-infrared energy range that additionally exclude an interpretation of the photoemission results as surface effect.

6 Tracing the incommensurability of misfit layered compounds

A special feature of misfit layered compounds has already been mentioned: Due to the incommensurability of one in-plane lattice constant of the two subsystems a one-dimensional misfit is constituted. Both subsystems cannot be regarded as independent since each of them is modulated with the periodicity of the other. Thus, misfit layered compounds have no three-dimensional translational symmetry although they exhibit a long-range order. They have these properties in common with quasicrystals. Quasicrystals (or quasiperiodic crystals) were discovered in 1982 [88] and enforced a new definition of crystals. They had been defined as being periodic arrangements of atoms before. With the observation of fivefold and tenfold symmetry axes which are incompatible with periodicity crystals were redefined by the International Union of Crystallography to be "...any solid having an essentially discrete diffraction diagram" [89]. Among the family of quasiperiodic crystals two special categories are identified [8]: incommensurately modulated crystals that consist of a basic (or average) ordered structure that is perturbed periodically with an incommensurate period of the modulation and incommensurate intergrowth crystals. Misfit layered compounds belong to the latter category. Their diffraction patterns are characterized by the existence of two or more subsets of main reflections, caused by the average structures of the different subsystems, and a set of weak reflections caused by the modulations (see Fig. 4.5).

The electronic structure of quasicrystals has ever since been a topic of scientific interest and its determination an experimental challenge [90,91]. Contrary to conventional metallic alloys the thermal and electrical conductivities have been found to be unusually low. A pseudogap at the Fermi energy and a dense concentration of weakly dispersive bands in its close vicinity were meant to be the main features of their electronic structure [92,93]. Recently it was found for the decagonal quasicrystal $\text{Al}_{71.8}\text{Ni}_{14.8}\text{Co}_{13.4}$ that the s, p and d states exhibit band-like behavior with the symmetry of the quasiperiodic lattice and that the Fermi level is crossed by dispersing d bands [94]. These results suggest that the electronic states of quasicrystals are not dominated by localization despite the lack of periodicity which makes the Bloch concept not applicable.

However, experimental studies of the electronic valence band structure of incommensurate intergrowth compounds are rare. In particular, to my knowledge, no photoemission studies have been published in view of the influence from the incommensurability on the band structure of misfit layered compounds. Due to the one-dimensional misfit and the mutual modulation of both subsystems the translational symmetry in misfit layered compounds is - strictly speaking - absent. The consequences for the electrons in similar structures was investigated theoretically, resulting partially in localization [95] or in a nonuniform distribution of electronic spectral weight over a complex eigenvalue spectrum [96]. For misfit layered compounds theoretical considerations predicted the influence of the misfit on the electronic band structure to be rather weak [29]. Nevertheless, it is essential to study experimentally effects that alter the electronic states due to the incommensurability before we will go more into detail concerning the stability of misfit compounds in Chapter 7 and 8.

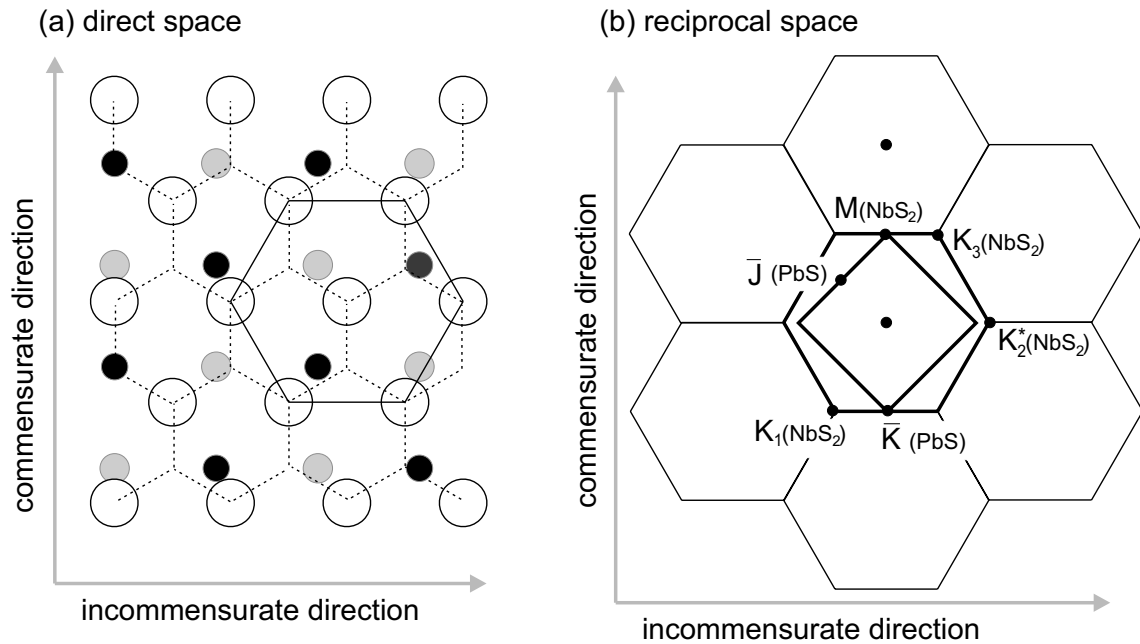
6.1 Symmetries in the electronic structure of $(\text{PbS})_{1.14}\text{NbS}_2$ 

Figure 6.1: Schematic representation of the misfit in (a) direct space and (b) reciprocal space. In (a) the TMDC subsystem is represented by the chalcogen atoms as open circles. The PbS subsystem is denoted by smaller black and grey circles, representing Pb and S, respectively. (b) shows the hexagonal reciprocal lattice of the TMDC system and the square surface Brillouin zone of PbS. In both images the commensurate and incommensurate axes are indicated.

Fig. 6.1 shows the geometric conditions in misfit layered compounds. The direct lattice is given in (a). For the sake of clarity only the upper sulphur atoms are shown as open circles representing the TMDC subsystem. Smaller black and grey circles denote the lead and sulphur atoms of the PbS subsystem, respectively. Both commensurate and incommensurate directions are indicated (see also Chapter 2.3). In Fig. 6.1 (b) the geometric structure is transformed into reciprocal space. The hexagonal first Brillouin zone of the TMDC subsystem, e. g. NbS_2 , is given with its points of high symmetry Γ , K and M. The PbS subsystem is represented by its quadratic surface Brillouin zone of the (001) surface and the corresponding high symmetry points \bar{J} and \bar{K} . Strictly speaking these Brillouin zones are only valid in the unperturbed constituent subsystems. Taking the mutual modulations of both subsystems into account the strict periodicity of conventional crystals is lost and a Brillouin zone cannot be given. In Ref. [29] a twofold Brillouin zone was used for band structure calculations that was obtained from an approximant $(\text{SnS})_{1.20}\text{NbS}_2$. In our case it is more convenient to stick to the Brillouin zones of the single subsystems. However, the twofold symmetry is taken into account by indicating the commensurate axis parallel to one ΓM direction of the TMDC subsystem. Thus, the six M points of the first Brillouin zone that are equivalent in pure NbS_2 are divided into two groups of inequivalent M points. Either the M point is orientated along the commensurate axis or not. The same considerations are applicable to the K points of the NbS_2 subsystem with respect to the orthogonal axis which is indicated as incommensurate. In Fig. 6.1 (b) three K points are highlighted that will play an important role in the following measurements: The K_2 point is in line with the

incommensurate axis and is therefore here and in the following marked with a star (*).

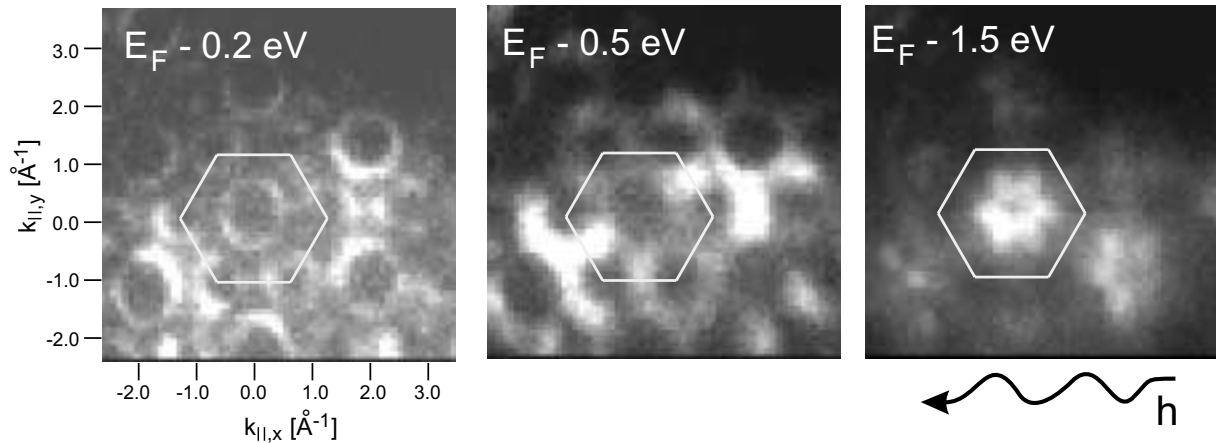


Figure 6.2: Photoelectron angular distributions of $(\text{PbS})_{1.14}\text{NbS}_2$ at the given binding energies with an excitation energy of $h\nu = 157.3$ eV

To get a first overview over the electronic structure of misfit layered compounds and in particular of $(\text{PbS})_{1.14}\text{NbS}_2$ we measured photoelectron angular distributions (PAD) with a high excitation energy of $h\nu = 157.3$ eV that are given in Fig. 6.2. The images represent a horizontal cut through reciprocal space at constant binding energies where white indicates a high intensity of photoelectrons (see Chapter 3.1). Thus, we get an insight into symmetries of the electronic structure in reciprocal space. The first Brillouin zone of the NbS_2 subsystem is indicated by the white hexagon, respectively. The images reveal clearly the sixfold symmetry characteristic for the TMDC subsystems. In particular we can identify in the first two images the ringlike structures around the Γ and K points of the Brillouin zone that we know from NbS_2 and NbSe_2 (see Chapter 4.3 and Ref. [39]). They can be attributed to the Nb 4d band. This band is unoccupied at the center of the Brillouin zone. Towards the border of the Brillouin zone it lowers in energy and gives rise to the ringlike emission feature when it passes through the Fermi energy. Towards the K points of the Brillouin zone the d band disperses upwards in energy and passes the Fermi energy again so that it is unoccupied at the K points. The dispersion of the d band results in the ringlike structures around the K points. The emissions in the last image originate from electrons of the sulphur band at a binding energy of $E = E_F - 1.5$ eV exhibiting the hexagonal symmetry as well. By comparison of these measurements with the corresponding measurements of pristine NbS_2 and NbSe_2 we can state that the electronic structure is significantly dominated by the NbS_2 subsystem. The deviations will be discussed in Chapter 7 with regard to the bonding between both subsystems. The symmetry of the electronic structure is perfectly hexagonal within experimental accuracy, i. e. an influence of the one-dimensional misfit can not be recognized by a deviation of the hexagonal symmetry. Even in higher Brillouin zones of the NbS_2 subsystem the hexagonal pattern of the electronic structure is not disturbed at all. It is therefore reasonable to use the Brillouin zone of the TMDC subsystem to describe the electronic structure as it is done in Chapter 7.

6.2 Misfit induced modification of the Fermi surface

The influence of the incommensurability on electronic properties of the misfit layered compound $(\text{SmS})_{1.19}\text{TaS}_2$ has been studied by electrical and magnetic transport measurements [97, 98]. The results pointed to an electrical transport that is carried out by charge carriers in the TaS_2 layers only. This effect was ascribed to a localization of electrons in the SmS layers that results from the incommensurability. In semiconducting misfit compounds containing VS_2 as TMDC subsystem it was found that the carrier localization is realized in the VS_2 layers as well [99]. The lattice incommensurability yields a quasiperiodic potential that generates energy gaps in the conduction band in one dimension or zone-folding effects in two-dimensional systems. The position in reciprocal space where these effects occur is determined by the periodicity of the modulation. In the case of $(\text{PbS})_{1.14}\text{NbS}_2$ photoemission measurements are dominated by the NbS_2 subsystem. Its modulation is given by the lattice constant of the PbS subsystem. An effect of the incommensurability on the electronic structure of $(\text{PbS})_{1.14}\text{NbS}_2$ should thus be expected at the Fermi energy and at a location in reciprocal space that is given by the PbS system and the incommensurate axis (see Fig. 6.1). In the following photoemission measurements with a special emphasis on this region will be presented.

Fig. 6.3 (a) shows photoelectron angular distribution images with an enhanced energy and momentum resolution with respect to Fig. 6.2. They were obtained by excitation of the electrons with a lower photon energy of $h\nu = 21.22$ eV. Consequently only the first Brillouin zone is visible. Again, we can clearly observe the ringlike structure around the Γ point at and close to the Fermi energy. In case of the emission features around the K points of the first Brillouin zone we can only distinguish four of these rings. In the direction that is labelled K_2^* and in the opposite direction no intensity is observed. Nonetheless, the observable K points are located precisely on the border of the hexagonal Brillouin zone of NbS_2 . The photoelectron angular distribution at the binding energy of $E = E_F - 1.4$ eV exhibits the emissions from the sulphur derived valence band and resembles the hexagonal pattern from Fig. 6.2.

The hexagonal symmetry is clearly confirmed by the azimuthal angle scan depicted in Fig. 6.3 (b). The scan has been measured along the white circle that is given in the PAD image at the Fermi energy in (a). The polar angle was chosen to $\vartheta = 30^\circ$ which corresponds with equation 3.5 to a parallel component of the photoelectron wave vector of $k_{\parallel} = 1.06 \text{ \AA}^{-1}$ at the Fermi energy. This is exactly the k_{\parallel} component of the $\bar{\text{K}}$ point of the PbS subsystem. Three of the high symmetry directions of the NbS_2 subsystem are marked by arrows. They are labelled simply with K_1 , K_2^* and K_3 , although – strictly speaking – the K points of the NbS_2 system are located at a higher absolute value of k_{\parallel} (see Fig. 6.1 (b)). For the sake of simplicity we will stick to this nomenclature in the following. The high symmetry points of the NbS_2 system were identified by the intensity minima according to the PAD image. Each minimum is separated exactly by an angle of $\Delta\varphi = 30^\circ$ from the next which corresponds to the angle between neighboring K and M points in the Brillouin zone. Only in the angular range between 0° to 70° the overall intensity is too low to clearly identify the minima, because the incoming light is shadowed by the spectrometer. On the other hand the AAS reveals reasonable high intensity in the angular range between 180° to 270° , so that the missing emission structures at K_2^* in the PAD can not be explained by an artefact of the measurement geometry. In Fig. 6.3 (c) energy distribution curves were measured at a temperature of $T = 70$ K and an overall energy resolution of $\Delta E = 60$ meV along the lines

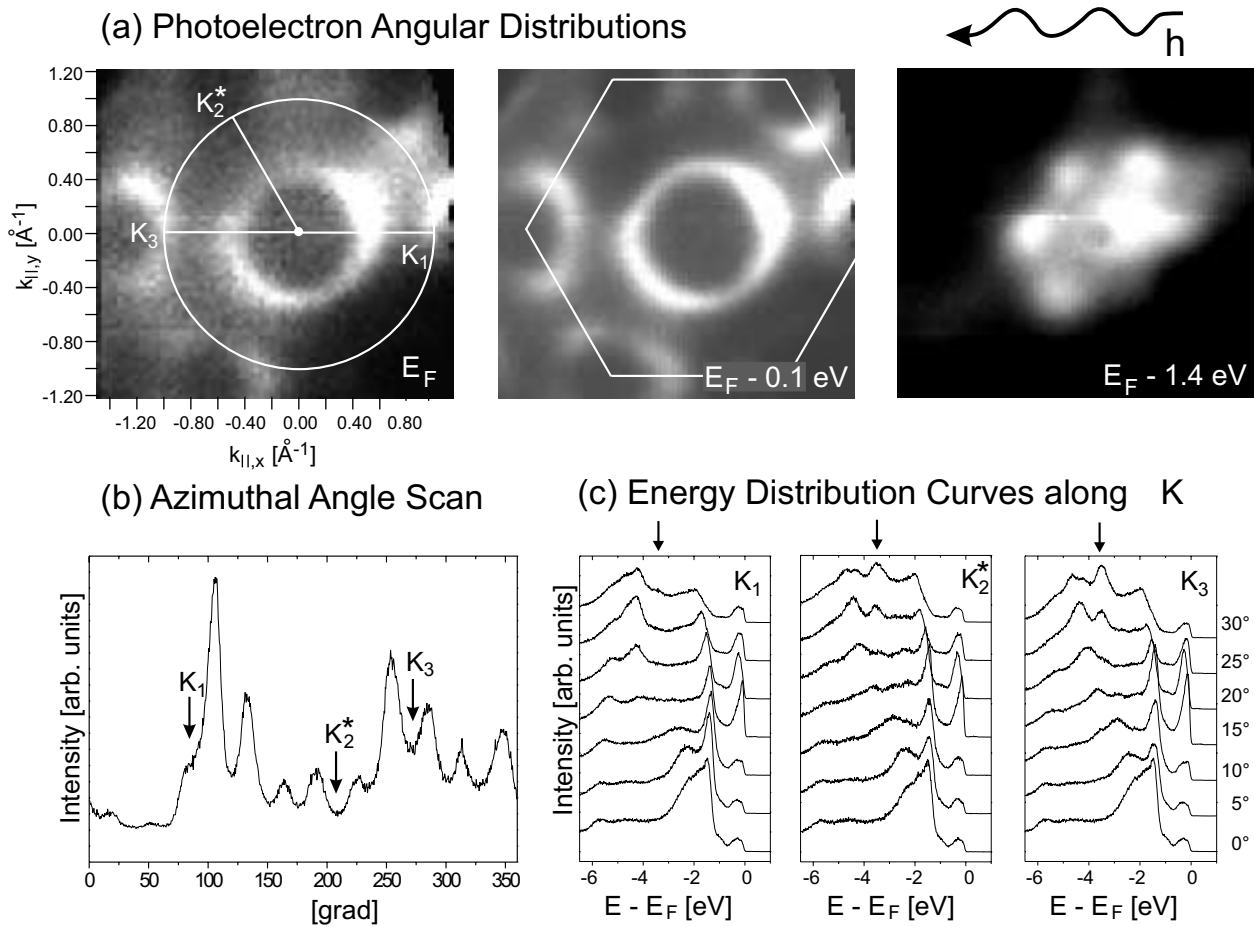


Figure 6.3: (a) Photoelectron angular distributions of $(PbS)_{1.14}NbS_2$ at the given binding energies, (b) azimuthal angle scan close to the Fermi energy ($E - E_F = -0.05$ eV) and (c) energy distribution curves along the directions that are indicated in (a). All measurements were performed with a photon energy of $h\nu = 21.22$ eV. The direction of the incident light is indicated in (a) and corresponds to an azimuthal angle of $\varphi = 90^\circ$.

$\Gamma K_{1,2,3}$. These directions are indicated in the photoelectron angular distribution and the azimuthal angle scan. Although the directions $\Gamma K_{1,3}$ on the one hand and ΓK_2 on the other seem to be inequivalent from the PAD the overall dispersion of electronic states is similar in all three directions as it is expected for the undisturbed NbS_2 subsystem. Measurements that are not shown here prove that this is the case for all directions ΓK . The only difference that can be observed here is the strongly decreased intensity of a peak at a binding energy of $E - E_F = -3.5$ eV in the direction ΓK_1 at $\vartheta = 25^\circ$ and 30° . This peak is marked by arrows in the figure. By the measurement of this specific peak at every K point and under different azimuthal angles of light incidence we could attribute the intensity variation to an influence of the incident light. A detailed analysis of these intensity variations will be presented in Chapter 6.3. In contrast to the different ΓK directions we could observe no differences along the inequivalent directions ΓM . Therefore they are not considered here and will be presented later in Chapter 7.

A second difference along the different directions ΓK becomes obvious by looking closer at the niobium derived 4d band. The spectra at $\vartheta = 30^\circ$ of Fig. 6.3 (c) in an energy range close

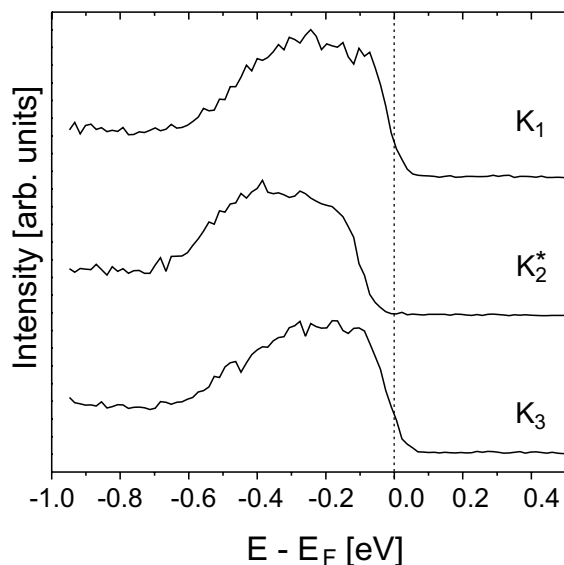


Figure 6.4: Comparison of the Nb 4d derived electronic state at $\vartheta = 30^\circ$ for the three directions indicated in Fig. 6.3. The spectra were measured at $T = 70$ K and an overall energy resolution of $\Delta E = 60$ meV.

to the Fermi level are depicted in Fig. 6.4. We can clearly observe an energetic shift of the peak to lower energies for the direction ΓK_2^* with respect to the directions ΓK_1 and ΓK_3 . This energetic shift from the Fermi level to higher binding energies explains the asymmetry of the photoelectron intensity in the photoelectron angular distributions at binding energies close to the Fermi level.

In order to get insight into the origin of the energetic shift of the niobium derived band close to the Fermi level we performed a rather unusual mode of photoemission. The results are depicted in Fig. 6.5 (b). The image represents energy distribution curves close to the Fermi level that are depicted as grey scale images where white indicates a high intensity of photoelectrons. The spectra were normalized to the photon flux.

The spectra were measured at constant polar angle $\vartheta = 30^\circ$ which again corresponds to a parallel component of the photoelectron wave vector that coincides with the \bar{K} point of the PbS subsystem and thus with the modulation periodicity. The azimuthal angle φ was varied so that this photoemission mode resembles an azimuthal angle scan where a whole spectrum is taken at each point of the azimuth. This photoemission mode is visualized in the upper left part of Fig. 6.5. The Brillouin zones of the NbS₂ subsystem (hexagon) and the PbS subsystem (square) are depicted. The incomplete circle represents the line where in steps of $\Delta\varphi = 5^\circ$ the spectra were measured. Also the different K points of the NbS₂ system are indicated. K_2^* again denotes the incommensurate direction. The direction of the incident light is marked here and corresponds to an azimuthal angle of $\varphi = 90^\circ$.

In the representation of Fig. 6.5 (b) we can follow the dispersion of the niobium derived band along a line in reciprocal space with constant polar angle (and thus with constant absolute value of k_{\parallel}) instead of only studying the intensity at a constant energy. Note that this measurement was performed for a different sample than in Fig. 6.3 so that the azimuthal angles of the high symmetry points are different. The angular range of this scan has been chosen such that it comprises three K points of which at least one is inequivalent

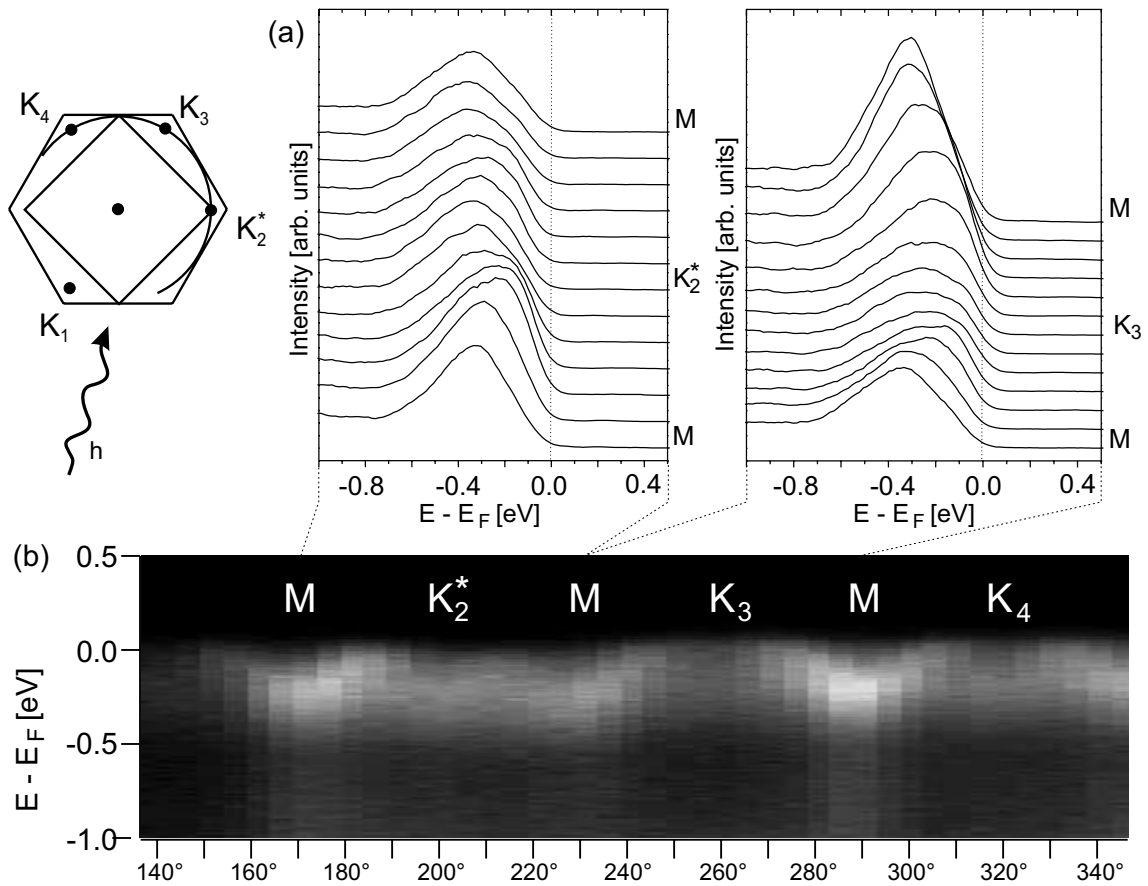


Figure 6.5: (a) Energy distribution curves at a constant polar angle $\vartheta = 30^\circ$ around two inequivalent K points ($h\nu = 21.22$ eV). (b) Dispersion of the Nb derived band within a large polar angle range. The spectra are depicted as grey scale image where white belongs to high photoelectron intensity.

with respect to the misfit (see Fig. 6.1). The shift in a specific direction ΓK_2^* could well be reproduced at an angle of $\varphi = 200^\circ$ with respect to the $K_{3,4}$ points at $\varphi = 260^\circ$ and $\varphi = 320^\circ$. Following the dispersion of the Nb 4d band we can clearly observe it passing through the Fermi level at the two latter K points (K_3 and K_4). At the K_2^* point it exhibits a completely different behavior. From the neighboring M point it disperses upwards to higher energies but at approximately $\frac{1}{2}$ MK the dispersion is reversed and reaches a new minimum at the respective K_2^* point. The electronic band does not cross the Fermi energy and remains occupied so that it is not part of the Fermi surface any more as we have seen in Fig. 6.3 (a). The energy distribution curves around two inequivalent K points K_2^* and K_4 are depicted in Fig. 6.5 (a). The spectra were smoothed by averaging over five adjacent data points. The backward dispersion of the Nb derived band towards K_2^* point can clearly be observed in contrast to the dispersion of the band through the Fermi level at the K_4 point.

With these measurements we could verify the localization of charge carriers in the incommensurate direction of misfit layered compounds that was predicted due to the analysis of transport properties [97, 98]. With angle-resolved photoemission measurements we could

for the first time directly observe an energy gap at the Fermi level and a reversed dispersion of the Nb 4d band in the incommensurate direction. This modification of the Fermi surface of $(\text{PbS})_{1.14}\text{NbS}_2$ can be ascribed to the quasiperiodic modulation of the potential in the NbS_2 with a periodicity corresponding to the PbS lattice.

6.3 Photoelectron diffraction from localized valence band states

Photoemission spectroscopy yields not only information about the electronic structure of crystal surfaces but by the detection of the angular dependence of scattered photoelectrons it also offers structural information about the sample. Conventionally, the excitation energy of photoelectrons lies in the X-ray regime for this purpose. This method is called **X-ray Photoelectron Diffraction (XPD)** and has widely been used in recent years, e. g. Ref. [100, 101]. In the usual interpretation of XPD the emission of a spherical electron wave from a lattice site is crucial [102]. Therefore, XPD measurements were mostly restricted to electrons that were excited from localized core levels. In Ref. [103] this case was generalized to treat emissions from delocalized valence states. The interpretation of photoemission proceeds there via the construction of the photoelectron state Ψ with energy E_{fin} which can be written at the detector located in the direction of the polar (ϑ) and azimuthal (φ) emission angles as

$$|\Psi\rangle = \sqrt{D} G(E_{fin}, \vartheta, \varphi) (\mathbf{A} \cdot \mathbf{p}) |\Psi_{in}\rangle, \quad (6.1)$$

where D is the surface density of states (SDOS), G is the propagator, \mathbf{A} is the vector potential and \mathbf{p} is the momentum operator. The propagator describes the electron scattering from the point of excitation through the crystal to the detector. The combined consideration of both energy positions that reflect the SDOS and intensity patterns influenced by the propagator was applied to interpret angle-scanning data of the GaAs(110) surface in the VUV regime.

In order to investigate the angular dependence of photoelectrons of the misfit layered compound $(\text{PbS})_{1.14}\text{NbS}_2$ we studied the peak at a binding energy of $E - E_F = -3.5$ eV which exhibited a strong dependence from the incident light. The electrons were excited with linearly polarized synchrotron radiation of an energy $h\nu = 21.22$ eV.

The results are shown in Fig. 6.6 (solid dots) as a polar diagram where the radial distance to the center indicates the photoelectron intensity in dependence of the azimuthal angle φ . The angle of incidence of the light was at $\varphi = 90^\circ$ as in all previous measurements. In this orientation of the sample with respect to the incoming light the incommensurate axis of the misfit sample was determined along $\varphi = 225^\circ$. The open dots represent exactly the same measurement after the sample was rotated by $\Delta\varphi \approx 45^\circ$, so that the incommensurate axis is orientated along the direction $\varphi = 270^\circ$ which coincides with the angle of incidence of the synchrotron radiation which has not been altered. For both measurements the sample was adjusted accurately with respect to the Γ point beforehand.

The intensity patterns are totally different for both sample orientations. Starting with the azimuthal angle scan measured for the arbitrarily orientated sample (solid dots) the photoelectron intensity is on a first view evenly distributed over the whole azimuth. In the opposite direction to the light incidence the intensity is enhanced which is in accordance to the intensity variations of the corresponding peak in the energy distribution curves in Fig. 6.3 (c). Nonetheless, a sixfold symmetry can not be distinguished so that the intensity distribution seems not to be dominated by band structure effects. After the sample was

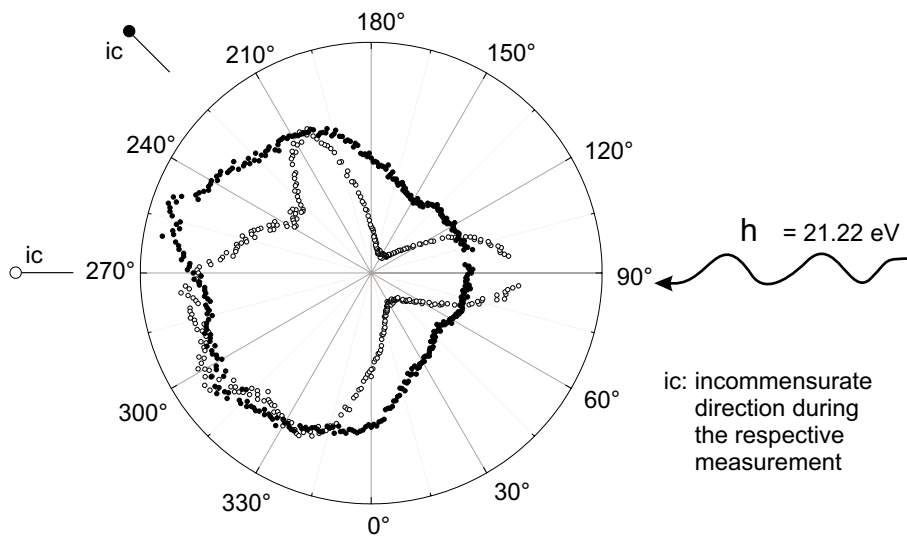


Figure 6.6: Azimuthal angle scans at $\vartheta = 30^\circ$ and at a binding energy of $E - E_F = -3.5$ eV. The photon energy is $h\nu = 21.22$ eV. Between the first scan (solid dots) and the second scan (open dots) the sample was rotated by $\Delta\varphi \approx 45^\circ$ counter-clockwise so that the incommensurate axis is in the plane that is spanned by the light incidence and the polarization vector. The polar angle of the incident light was in both cases 55° to the surface normal.

rotated by $\Delta\varphi = 45^\circ$ so that the incommensurate axis is in line with the incoming polarized light the photoelectron intensity pattern is largely changed. Only in the angular range between $\varphi = 270^\circ$ and $\varphi = 360^\circ$ the intensity remains mainly constant with weak maxima at $\varphi = 275^\circ$, 305° and 335° , which might be attributed to the band structure and would then correspond to the M and K points, respectively. The remaining larger part of the intensity pattern is clearly structured. Two distinct maxima can be distinguished at $\varphi = 0^\circ$ and $\varphi = 210^\circ$ that are separated by a deep minimum at $\varphi = 150^\circ$. A second minimum can be found at $\varphi = 30^\circ$. Except for the high intensity at $\varphi = 305^\circ$ the whole pattern is highly symmetric with respect to a mirror plane along the angle of incidence of the light which coincides with the incommensurate axis of the misfit sample. In order to exclude band structure effects as the origin of this symmetry we rotated the sample for a second time counter clockwise by $\Delta\varphi \leq 10^\circ$ and measured the corresponding azimuthal angle scan. Since no significant difference could be observed it is not shown here. The angles of the intensity extrema were absolutely identical, indicating their origin not to be found in the band structure. Comparing it to typical photoelectron diffraction patterns as in Refs. [100, 103, 104] there is strong evidence that the angular intensity variations originate from scattered photoelectrons. As it was pointed out before the localization is meant to be crucial for photoelectron diffraction. When it was, nonetheless, observed from valence band states it was explained in Ref. [105] by a strong degree of hole localization in high energy valence band photoemission. In Ref. [106] this explanation was doubted, the observation of the diffraction pattern was deduced to the k-space integration during the photoemission process due to the use of high excitation energies ($h\nu \geq 1200$ eV) and a rapidly oscillating phase factor in the matrix elements which ensures that only the local contributions are important, just as in core level excitations.

In the here described case the electrons were excited with synchrotron radiation in the

VUV regime where k-space integration is negligible. Furthermore the diffraction pattern could only be observed when the incommensurate axis of the sample was in line with the incident light and thus with the polarization vector of the radiation. With regard to the matrix element in Equation 6.1 we can state that in this experimental setup the vector potential of the radiation and the momentum of the electrons in the incommensurate direction are planar. Assuming the localization of electrons to be crucial for photoelectron diffraction it is evident that the electrons with momentum in the incommensurate direction of misfit compounds seem to be localized to a certain extent. However, for a closer study of this phenomenon and more stringent conclusions an adequate theoretical support is indispensable.

6.4 Conclusions

Using angle scanning modes of angle resolved photoelectron spectroscopy we studied symmetries in the electronic structure of the misfit layered compound $(\text{PbS})_{1.14}\text{NbS}_2$. It exhibits a perfect hexagonal symmetry and resembles largely the electronic structure of the constituent layered dichalcogenide NbS_2 . Also in energy distribution curves we can clearly identify emissions from electronic states of the NbS_2 subsystem that will be discussed in detail in the following chapter. An effect of the incommensurability can thus not be found in an altered symmetry of the electronic structure in reciprocal space. The influence of the misfit could be found in the dispersion of the niobium derived band at the Fermi level. It passes through the Fermi energy towards the K points in pristine NbS_2 and also at the K points that are not in line with the incommensurate axis of the misfit compound. In the incommensurate ΓK direction this band remains below the Fermi level. It exhibits a reversed dispersion and does not contribute to the Fermi surface there any more. We can ascribe these zone folding effects to the quasi-periodic potential in the incommensurate direction, all the more so as these effects occur in locations of reciprocal space that are determined by the PbS subsystem that is the origin of the modulation.

Furthermore we observed a direct connection between the scattering of photoelectrons and the orientation of the misfit axis with respect to the polarization of the synchrotron radiation that excites the electrons. A distinct photoelectron diffraction pattern can only be observed when the incommensurate axis of the misfit compound is orientated along the plane that is spanned by the direction of the incoming light and its polarization vector, i. e. when the vector potential of the light and the electron momentum of the matrix element in Eq. 6.1 are planar. Since localized electronic states are meant to be crucial for photoelectron diffraction this is a clear evidence that the electrons are localized in the incommensurate direction of misfit compounds.

7 What makes misfit compounds stick together?

Misfit layered compounds are built up by two different subsystems (see Chapter 2.3) that differ not only by their electronic properties (semiconducting/metallic) but also the geometric structure and symmetry at the interface of both interpenetrating sublattices is completely different. Nevertheless, these crystals grow as natural minerals and they can also be grown synthetically by chemical transport techniques with a high degree of structural perfection (Chapter 4.3). The different layers are stacked regularly in an alternating way indicating strong interactions that compensate for the low entropy inherent to such an ordered stacking. The mechanisms that keep the layers together are not well understood though. Basically, three models are used to explain the great stability of misfit layered compounds:

Charge transfer A charge transfer from the MX part to the transition metal dichalcogenide would result in an electrostatic attraction. It was confirmed by transport measurements for the compounds with M representing rare earth metals or bismuth [107], whereas in misfit compounds containing lead or tin, this question is still controversially discussed and not finally answered yet [29, 108, 109]. Although a higher filling of the conduction band related to the transition metal dichalcogenide could be observed [108], lead has never been found in a +4 oxidation state that should indicate a charge transfer to the neighboring TX_2 layer [110].

Cationic coupling Therefore another bonding mechanism has been proposed and confirmed by precise chemical analyses [31]: The divalent cations Pb or Sn of the MX layer are partially substituted by excessive transition metal atoms of the TX_2 layers which adopt a +3 oxidation state there. An equal amount of transition metal atoms in the adjacent TX_2 layer that transform from a +4 to a +3 oxidation state maintain the balance of charge. This model explains the filling of the TX_2 conduction band because each T^{3+} cation brings one additional electron to the TX_2 slab. This model results in a local electrostatic attraction at those positions where a Pb or Sn atom is exchanged and can therewith explain the modulation of both layers with the periodicity of the other.

Covalent bonding The third kind of interlayer bonding was suggested by Ettema and Haas [111]. By XPS measurements they excluded a charge transfer in lead and tin containing misfit layer compounds and attributed their stability to the presence of covalent interlayer bonds. This interpretation was confirmed by an analysis of the covalent bonding and valency of the metal atoms in the compounds with the bond-valence method [112].

7.1 Charge transfer in $(\text{PbS})_{1.18}\text{TiS}_2$ and $(\text{PbS})_{1.18}(\text{TiS}_2)_2$

In order to investigate the electronic structure of misfit compounds in view of a charge transfer the misfit compound $(\text{PbS})_{1.18}\text{TiS}_2$ was chosen for the special properties of its conduction band. The band structure of the TMDC 1T- TiS_2 has been discussed controversially, the main contentious issue was whether it is intrinsically semimetallic or semiconducting. In ARPES measurements, e. g. Ref. [113], weak emission features could be observed at the Fermi energy near the M point in reciprocal space that were attributed to electrons in the Ti 3d conduction band. But no holes in the S 3p bands were seen and this fact was

taken as evidence for the semiconducting behavior of TiS_2 , the electrons in the conduction bands were explained as originating from point defects, i. e. excess Ti atoms [114]. On the other hand transport measurements revealed clearly a T^2 dependence of the resistivity over a range of 10...400 K which is ascribed to electron-electron scattering and is thus a hint to metallic conduction [115]. Theoretical band structure calculations led to different results, e. g. a full-potential linear augmented-plane-wave method results in the semimetallic behavior of TiS_2 [116] in disagreement to pseudopotential calculations [117].

A compromise was found by Fang et al. [118]. Their calculations using the localized spherical wave method led to semimetallic behavior for bulk TiS_2 , while thin films of TiS_2 up to 11 sandwich layers were semiconducting with decreasing band gap for an increasing number of layers. However, the proximity of the Ti 3d conduction band to the Fermi energy makes misfit layered compounds containing TiS_2 sandwich layers especially suitable for studying a charge transfer.

Fig. 7.1 shows energy distribution curves along the high symmetry line ΓM (AL) in reciprocal space. In addition, the spectra are depicted as grey scale images $E(k_{\parallel})$, where white belongs to high intensity. The grey scale image belonging to TiS_2 is overlaid by the theoretical band structure as white lines. We can observe a good overall agreement between experimental and theoretical results. With respect to a charge transfer it should be noticed that the lowest unoccupied Ti 3d derived band touches the Fermi energy at the M-point. This band can be observed in the photoemission spectra as small peak near the edge of the Brillouin zone at approximately 30° in accordance to earlier ARPES studies that were mentioned before [113]. The highest occupied sulphur p derived bands have an energy maximum at the Γ point in the center of the Brillouin zone. While the calculated bands even reach the Fermi energy the measured emissions remain 0.6 eV below the Fermi level. This can be explained by taking into account that the k_{\perp} component of the wave vector of the photoelectrons remains undetermined and that the sulphur band is highly dispersive in the direction perpendicular to the surface (ΓA). Obviously the band structure is predominantly conserved in the misfit compounds. Nevertheless, two main differences can clearly be observed. The Ti 3d band is filled and shifts under the Fermi energy resulting in a conspicuous peak towards the M point. The second change concerns the highest sulphur band, which is decreased significantly in intensity. These effects are more distinct for the monolayer misfit compared to the bilayer compound: The emission from the Ti derived band at the Fermi energy is increased and extends closer to the Brillouin zone center, indicating a higher filling of the conduction band. Also the intensity of the highest sulphur derived band at the Γ point is further decreased.

Both features are well known to occur in intercalated transition metal dichalcogenides, i. e. TMDCs, where the intercalate (e. g. alkali metals) is inserted into the van der Waals gap between the layers. In Ref. [119] the electronic structure of TiS_2 is investigated in comparison to the Na and Cs intercalation compounds. The main modifications were determined as a filling of the conduction band, the opening of a gap between Ti derived d states and S derived p states (p-d gap) and a reduced S 2p band width. All these changes were attributed to a charge transfer from the alkali metals to the host material, making the Ti-S bonding more ionic. Following this argumentation we can therefore state that excess electrons occupy the conduction band of the transition metal dichalcogenide. But it is not clear yet whether these electrons originate from a charge transfer from the PbS to the TiS_2 layer or if they result from the change of Ti^{4+} into Ti^{3+} that is connected to a cationic coupling.

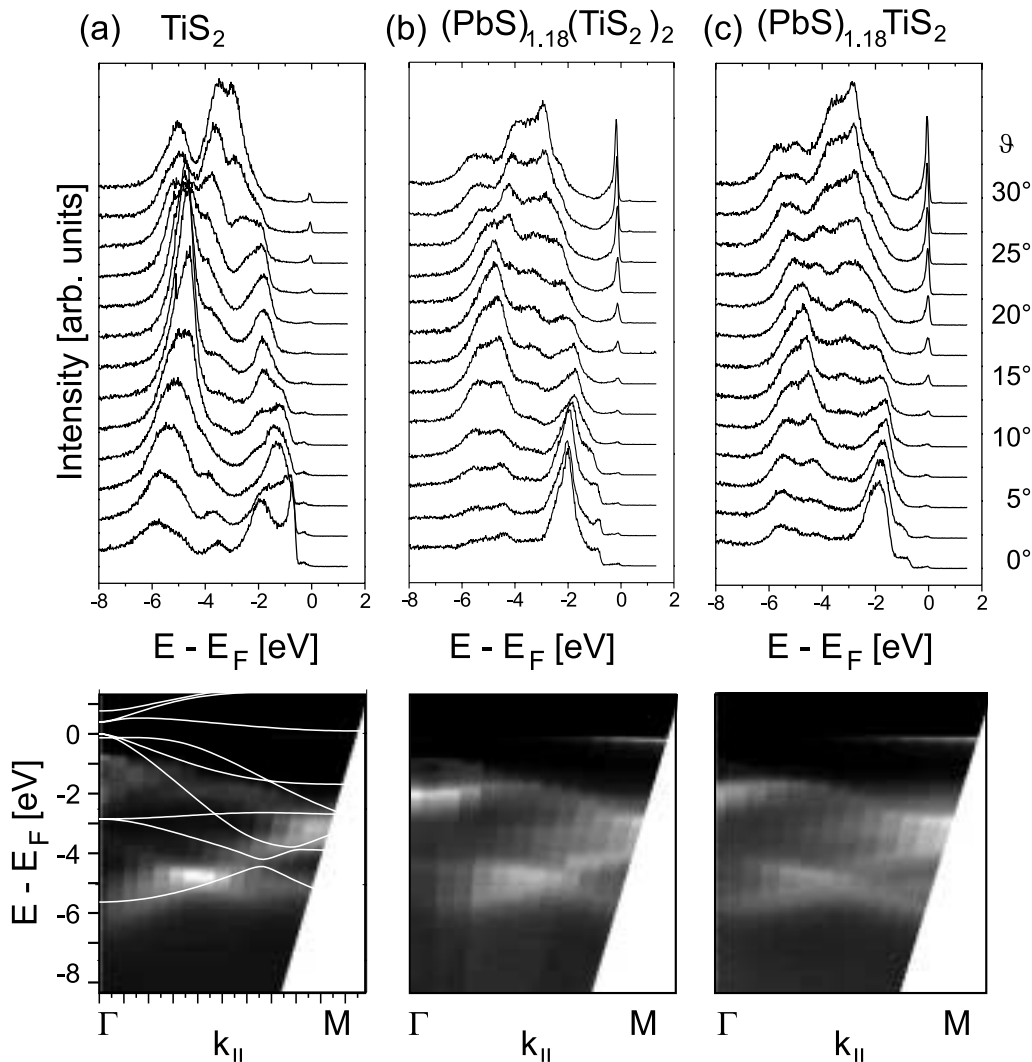


Figure 7.1: Energy distribution curves along ΓM (AL) of (a) TiS_2 (b) $(\text{PbS})_{1.18}(\text{TiS}_2)_2$ and (c) $(\text{PbS})_{1.18}\text{TiS}_2$. Below, the spectra are depicted as grey scale images $E(k_{\parallel})$, where white belongs to high intensity. For TiS_2 the theoretical band structure is overlaid as white lines. The spectra were measured with a photon energy $h\nu = 21.22$ eV and an overall energy resolution of 60 meV.

The increase of excess charge in the TMDC layer from the bilayer to the monolayer compound can be well understood in both cases. One has to consider that the number of PbS/ TiS_2 interfaces is equally increased: While in the bilayer compounds every TiS_2 sandwich layer is only neighbored by one PbS double layer, in the monolayer compound the TiS_2 layer is surrounded by two double layers of PbS. Assuming a charge transfer from PbS to TiS_2 (analogous to intercalation compounds) the number of transferred electrons would increase with an increasing number of PbS/ TiS_2 interfaces. In the case of a cationic coupling the substitution percentage of Ti for Pb in the PbS layer in both mono- and bilayer misfit compounds is about 10 at. % (see Ref. [31]). Thus it is evident that the number of transition metal atoms within one sandwich layer that transform from a tetravalent to a trivalent valency and that deliver the excess electrons is higher in the monolayer compared to the bilayer compound.

Since the experimental results can be explained by both models it was essential to ver-

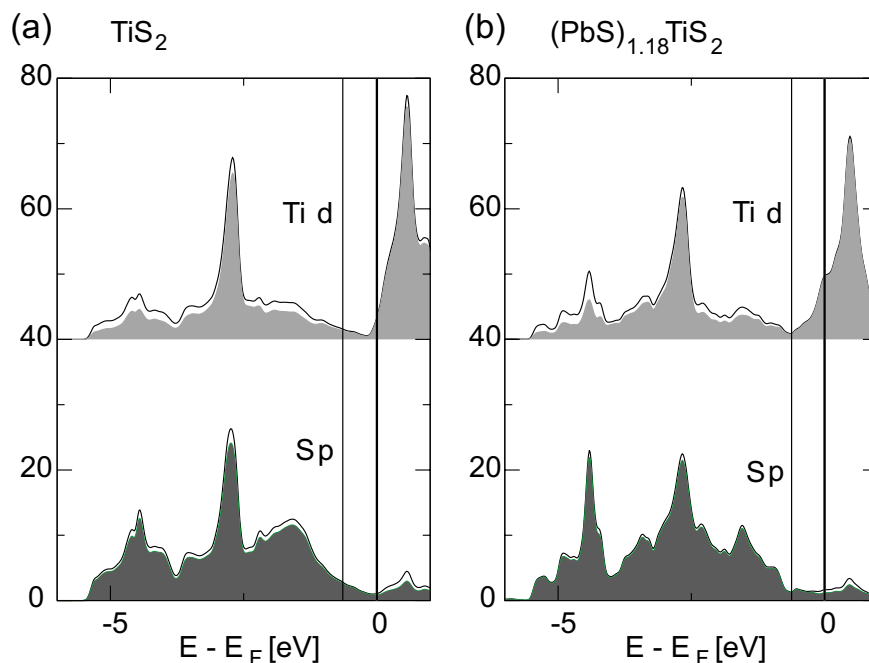


Figure 7.2: Calculated density of states (DOS) for (a) TiS_2 and (b) $(\text{PbS})_{1.18}\text{TiS}_2$. The upper panels show the DOS related to the titanium d states, the lower panels are related to the sulphur p states.

ify them by theoretical considerations⁹. The band structure calculations for the misfit compound were performed with the extended linear augmented plane wave $\mathbf{k} \cdot \mathbf{p}$ method (ELAPW- $\mathbf{k} \cdot \mathbf{p}$). [120–122] with a monoclinic base centered supercell with $a = 5.88 \text{ \AA}$, $b = 17.07 \text{ \AA}$ and $c = 23.52 \text{ \AA}$, which comprised 10 titanium, 32 sulphur, and 12 lead atoms, thereby offering a chemical composition of $(\text{PbS})_{1.2}\text{TiS}_2$ [73]. Fig. 7.2 depicts the calculated density of states for both the pure TiS_2 and the monolayer misfit compound $(\text{PbS})_{1.18}\text{TiS}_2$. The upper panels show the contribution of the titanium derived states, the lower panels show the contributions of the sulphur bands. At the Fermi energy the contribution of the Ti band is drastically increased for the misfit compound. The density of states is calculated for the undisturbed misfit compound, in particular without an exchange of any cations. Therefore the filling of the Ti 3d conduction band can be attributed to a charge transfer from the PbS to the TiS_2 layer just as it is known from intercalation compounds. It is not necessary to assume cationic coupling to explain the filling of the conduction band. Also the opening of the p-d gap resulting from this charge transfer is verified by the calculations. At a binding energy of -0.6 eV (thin line) the density of states of the TiS_2 crystal has nearly vanished in the misfit compound.

7.2 Bonding mechanisms in $(\text{PbS})_{1.14}\text{NbS}_2$

In Ref. [29] the electronic structure of the misfit layered compound $(\text{SnS})_{1.17}\text{NbS}_2$ was studied theoretically, particularly in view of the origin of their high stability. The authors found evidence for a charge transfer of 0.4 eV per formula unit $(\text{SnS})_{1.2}\text{NbS}_2$ but considered the resulting electrostatic interaction as not strong enough to explain the stability. Their band-

⁹Collaboration with E. E. Krasovskii and W. Schattke, DFG Forschergruppe 412/21

structure calculations show that there is covalent bonding between the two subsystems. A comprehensive experimental study of the electronic structure of the misfit layered compound $(\text{PbS})_{1.14}\text{NbS}_2$ will be given in the following chapters and shall be confronted with the theoretical results from Ref. [29]. The electronic structure of the misfit compound will be compared to the electronic structure of its TMDC constituent NbS_2 and NbSe_2 which mainly dominate the photoelectron spectra (see also Chapter 7.1).

Electronic structure parallel to the layers

Fig. 7.3 shows photoelectron spectra of the misfit crystal $(\text{PbS})_{1.14}\text{NbS}_2$ and its constituent NbS_2 and NbSe_2 . They were recorded with an excitation energy of 21.22 eV along the ΓM (AL) direction of the reciprocal space for the transition metal dichalcogenides. In case of the misfit compound the direction is determined by the respective direction of the NbS_2 layers.

The spectra of the stoichiometric NbSe_2 and of the misfit layered compound were fitted by a superposition of Voigt profiles that were convoluted with a Gaussian to take instrumental and phonon broadening into account. The peak positions are given in Fig. 7.4 as filled (strong emissions) and open (weak peaks) circles together with the theoretical band structure. The self-consistent band structure calculations¹⁰ were performed with the extended linear plane wave $\mathbf{k} \cdot \mathbf{p}$ method (ELAPW- $\mathbf{k} \cdot \mathbf{p}$) [120–122]. The misfit compound was thereby simulated by a monoclinic supercell that comprises five unit cells of the NbS_2 layer and three unit cells of the PbS layer which leads to a chemical composition of $(\text{PbS})_{1.2}\text{NbS}_2$. Starting with NbSe_2 (Fig. 7.3 (a)), that represents the stoichiometric undisturbed constituent of the misfit compound, we can observe the sharpest structures among the photoelectron spectra. The Nb 4d derived conduction band that is unoccupied at the Γ point, reaches the Fermi level at about 15° . In the center of the Brillouin zone, the Fermi surface is constituted by the lower lying Se 4p bands that show a strong dispersion to binding energies of approximately 5.5 eV in fairly good agreement to the calculations (see Fig. 7.4 (a)). In the ΓA direction two highly dispersive bands span the binding energy range from the Fermi level to -2.5 eV and give rise to emission peaks that have no connection to the band dispersion along the lines ΓM or AL.

The most significant difference in the corresponding NbS_2 spectra (Fig. 7.3 (b)) is the lowering of the sulphur bands, that do not reach the Fermi energy any more, opening thus a gap between the S 3p derived bands and the Nb 4d derived conduction band. According to band structure calculations (see Fig. 4.9 and Ref. [123]), the sulphur bands should have the same dispersion as the Se bands in NbSe_2 , in particular, they should reach the Fermi energy at the Γ point. Nevertheless, a distinct emission just below the Fermi level can be observed, which can be attributed to the Nb 4d derived band, that remains occupied and mainly dispersionless up to the Γ point and consequently does not cross the Fermi energy. Apart from these changes the band dispersion remains more or less the same. Passing to the misfit compound we can observe the same effects which are more pronounced though. The gap between sulphur and niobium derived bands is widened, the intensity drops close to zero there and the sulphur bands are further lowered in energy. Also the emission just below the Fermi energy is broadened. In contrast to NbSe_2 , in the misfit compound no highly dispersive bands perpendicular to the layers are available between E_F and -1 eV

¹⁰Collaboration with E. E. Krasovskii and W. Schattke, DFG Forschergruppe 412/21

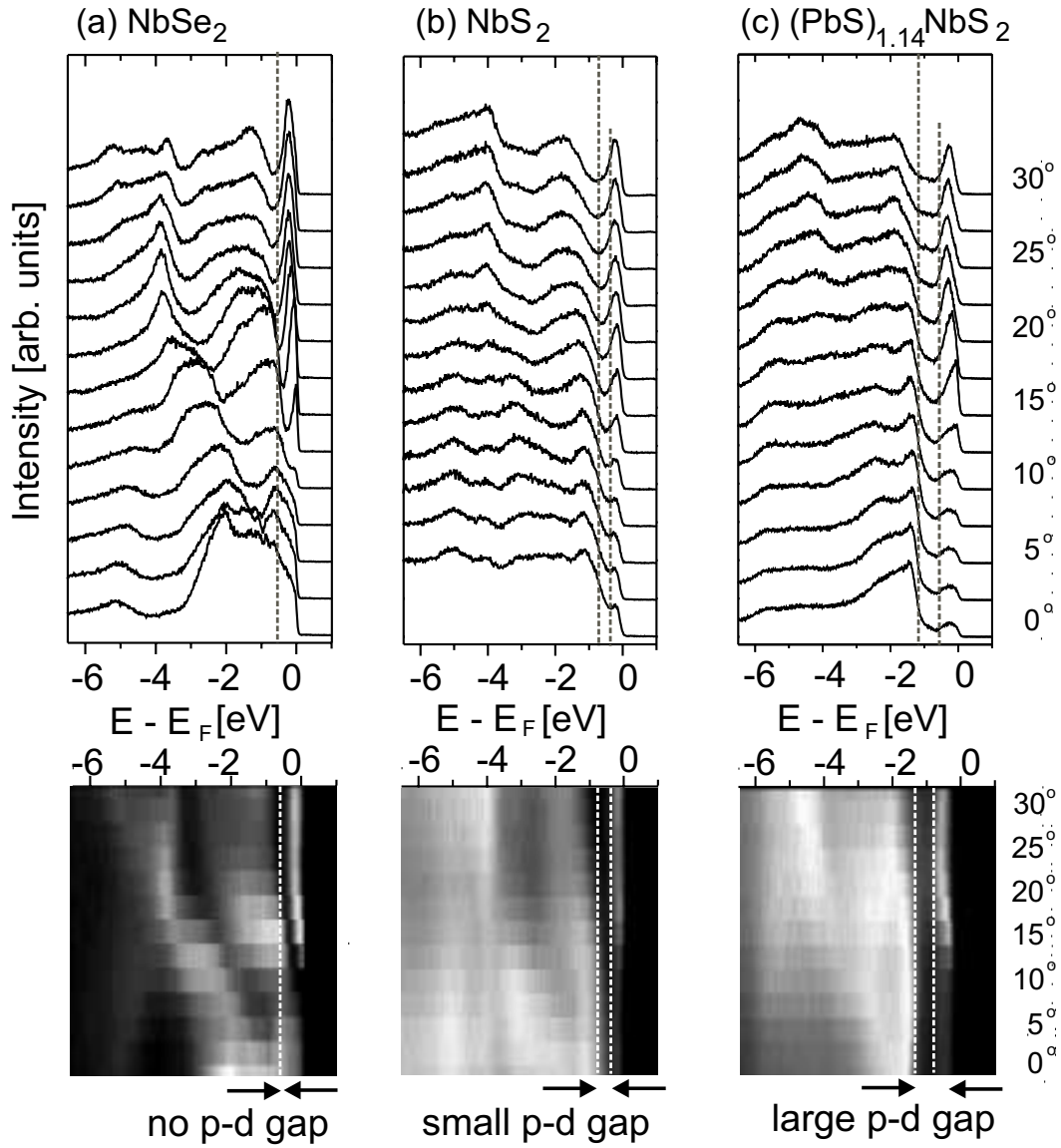


Figure 7.3: Energy distribution curves along ΓM (AL) of (a) NbSe_2 (b) NbS_2 and (c) $(\text{PbS})_{1.14}\text{NbS}_2$. Below, the spectra are depicted as grey scale images where white belongs to high intensity. The spectra were measured with a photon energy of $h\nu=21.22$ eV and an overall energy resolution of $\Delta E=60$ meV.

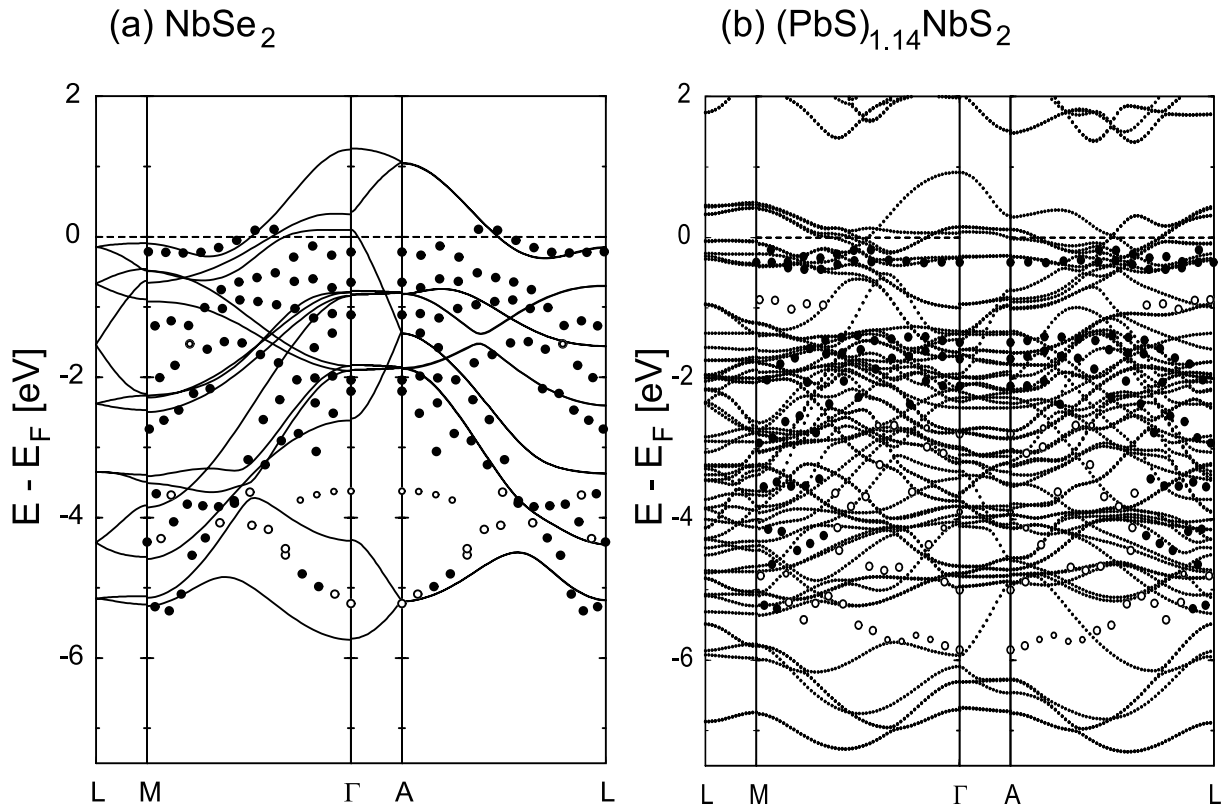


Figure 7.4: Comparison of experimental and theoretical band structures of (a) NbSe_2 and (b) $(\text{PbS})_{1.14}\text{NbS}_2$ along the direction ΓM in reciprocal space. (from Ref. [68])

binding energy. As a result, the experimentally observed spectral structures follow much closer the lines in ΓM or AL direction of the theoretical band structure (Fig. 7.4 (b)).

In Fig. 7.5 the ΓK (AH) has been mapped to make sure, that the occurring changes are not unique to one direction in reciprocal space. The overall dispersion is very similar in both directions for all samples. Again the gap between chalcogen and niobium derived bands increases from the stoichiometric NbSe_2 over NbS_2 to the misfit compound. Similarly the Nb derived emission just below the Fermi level can be pursued throughout the whole ΓK direction in NbS_2 and $(\text{PbS})\text{NbS}_2$, being broader at the latter sample.

Both the opening of a gap between Nb derived d bands and the chalcogen derived p bands and the filling of the conduction band are common features that were also observed in intercalation compounds of transition metal dichalcogenides, e. g. alkali metals or nickel in TiS_2 [119,124,125], ZrSe_2 [126] or VSe_2 [127] (see also Chapter 7.1). Together with a drastic decrease of the dispersion in the direction perpendicular to the layers they led the authors to the conclusion that a charge transfer from the intercalant to the host occurs. Misfit layered compounds have often been described as intercalates [128]. Apart from the similarity in electrical transport properties our measurements clearly indicate a close relationship between them particularly concerning the electronic band structure. Furthermore we can directly attribute the differences of the band structure between stoichiometric NbSe_2 and NbS_2 to a weak self intercalation of niobium atoms into the van der Waals gap of NbS_2 confirming previous results (see e. g. [31]).

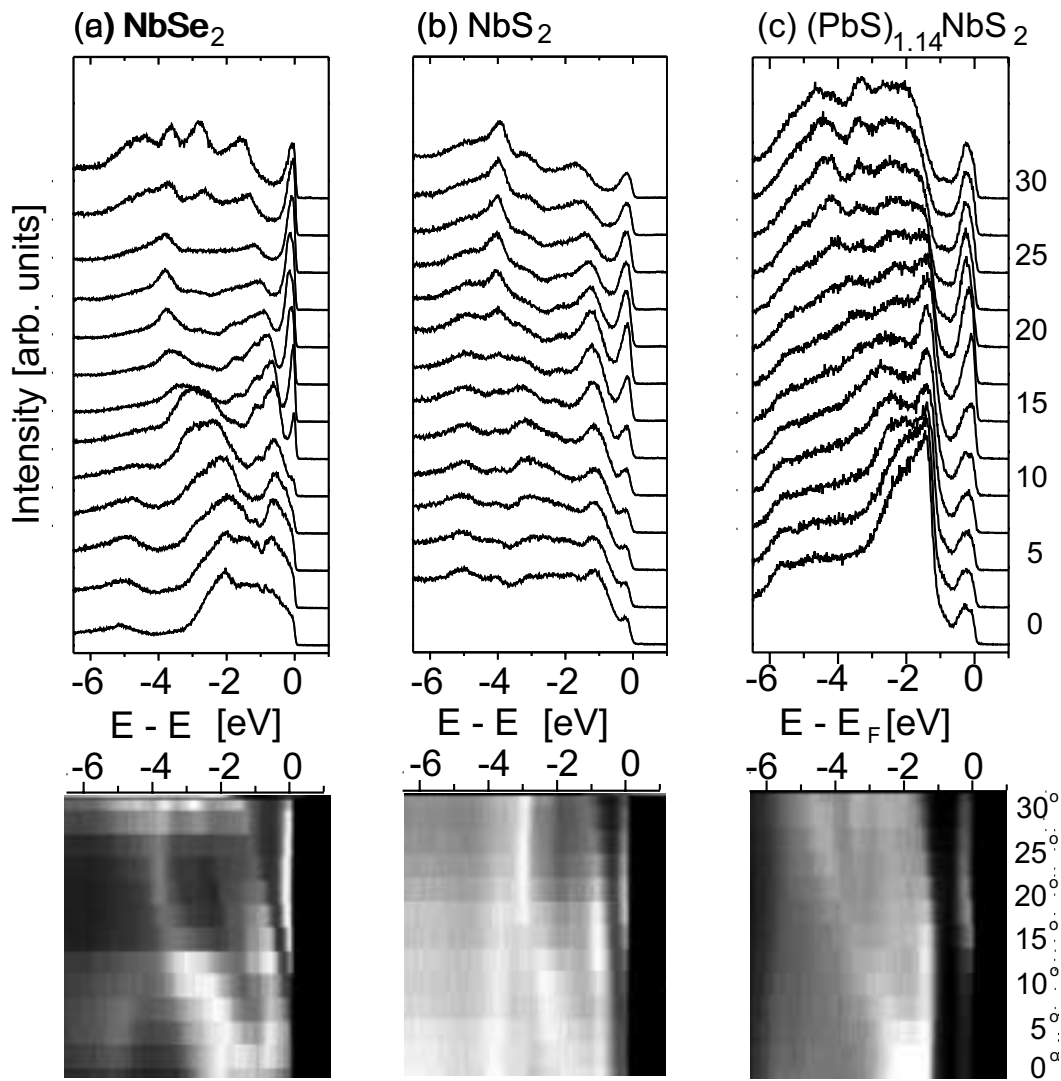


Figure 7.5: Energy distribution curves along ΓK (AH) of (a) NbSe_2 (b) NbS_2 and (c) $(\text{PbS})_{1.14}\text{NbS}_2$ and grey scale images, where white belongs to high intensity ($h\nu=21.22$ eV; $\Delta E=60$ meV).

Electronic structure perpendicular to the layers

A special emphasis was laid on the electronic band structure perpendicular to the layers, i.e. in the direction ΓA in reciprocal space, because this direction is most important for the comprehension of bonding mechanisms between the different layers.

Although transition metal dichalcogenides are often described as two dimensional, in Fig. 7.6 a clear dispersion of the bands can be observed both for NbSe_2 and NbS_2 . It is obvious from these measurements that an overlap of the selenium resp. sulphur orbitals across the van der Waals gap exists, though this does not contribute to the bonding, as both bonding and antibonding states are occupied. In contrast to previous studies of alkali metal intercalated transition metal dichalcogenides, where a total loss of dispersion perpendicular to the layers was stated even after a small amount of intercalants was exposed, we do observe dispersing bands in the self intercalated NbS_2 . Passing to the misfit compound the dispersion is finally lost completely.

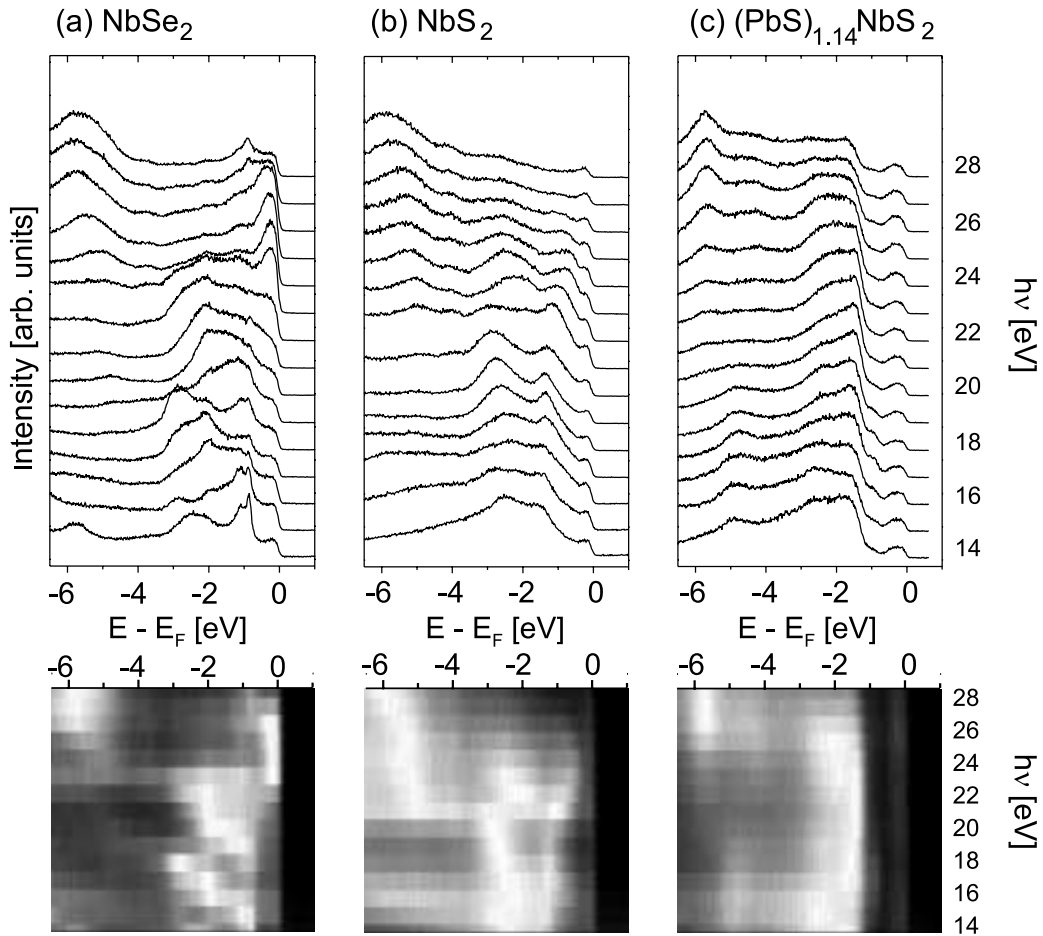


Figure 7.6: Energy distribution curves along ΓA of (a) $NbSe_2$ (b) NbS_2 and (c) $(PbS)_{1.14}NbS_2$ and grey scale images, where white belongs to high intensity (normal emission; $\Delta E=60$ meV).

In Fig.7.7 we traced the band structure over a larger range of the ΓA direction. In the photon energy range between 40 eV and 50 eV the two dominating emission features originating from sulphur derived states can clearly be distinguished at binding energies of -1.5 eV and -2.6 eV. At the first glance the higher bonded peak appears to disperse by approximately 0.5 eV to lower binding energies.

Additionally the same measurements were performed for the double layer misfit compound $(PbS)_{1.14}(NbS_2)_2$. Regarding only the NbS_2 layers, which are responsible for the photoemission peaks, the c -axis perpendicular to the layers is approximately by a half larger ($c=35.87$ Å) than in the single layer misfit compound ($c=22.8$ Å) [7]. The corresponding Brillouin zone is therefore smaller in this direction by the same factor and should result in a different characteristic of the layer perpendicular dispersion. In order to follow the band structure more accurately the spectra were fitted with a superposition of Voigt profiles. The peak positions are depicted as a function of the photon energy that determines the k_{\perp} component of the electron momentum for both compounds in Fig. 7.7 (c). Filled symbols represent strong peaks while open symbols mark the position of weak emissions. Both compounds $(PbS)_{1.14}NbS_2$ (circles) and $(PbS)_{1.14}(NbS_2)_2$ (squares) show a very sim-

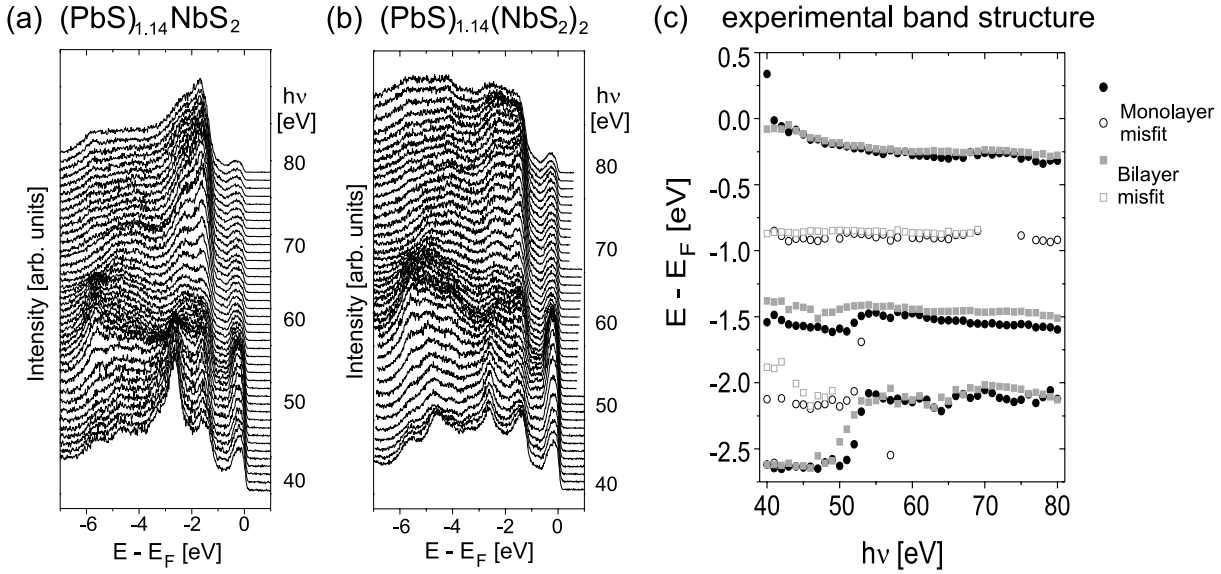


Figure 7.7: Photoelectron spectra of (a) the monolayer misfit compound $(\text{PbS})_{1.14}\text{NbS}_2$ and (b) the bilayer misfit compound $(\text{PbS})_{1.14}(\text{NbS}_2)_2$ at normal emission and with the photon energy varying over a large energy range. (c) Peak positions as a function of the photon energy for both misfit compounds as determined from the spectra in (a) and (b)

ilar electronic structure perpendicular to the layers. The energetic position of the bands coincide within experimental accuracy. It can be clearly seen that the bands remain flat throughout the whole photon energy range in agreement to the results for lower energies (see Fig. 7.6). Even the peak at a binding energy of $E_B \approx -2.0$ eV does not show any dispersion to lower photon energies but only decreases in intensity. Simultaneously a new peak appears at $E_B \approx -2.5$ eV so that it looks like the band would disperse by 0.5 eV. But since the same behavior of the electronic states is observed both for the monolayer and the bilayer misfit compound at the same photon energy it is evident that this behavior can not be attributed to dispersion but to a variation of intensities.

For the misfit compound $(\text{PbS})_{1.14}\text{NbS}_2$ we can state that there are no electronic states dispersing perpendicular to the surface along ΓA , i. e. at $k_{\parallel} = 0$. In order to learn more about the k_{\perp} band structure also at $k_{\parallel} \neq 0$ we used a special mode of angle resolved photoemission [129]. We measured the photoelectron intensity $I(k_{\parallel}, h\nu)$ as a function of the photon energy $h\nu$ and the k_{\parallel} component of the momentum of the photoelectrons at constant initial states. We obtain thus a vertical cross section through the electronic structure in the bulk Brillouin zone. Here, the sample was orientated such, that the k_{\parallel} component was varied along K Γ K.

The results are depicted in Fig. 7.8 as grey scale images where white belongs to high intensity. At the Fermi energy and 0.1 eV below we cut through the niobium derived 4d band. The Fermi surface is very similar to NbSe_2 [39], constituted by the cylindrical Fermi surface sheet centered at the ΓA line at $k_{\parallel} = 0$. Differently to NbSe_2 we do not observe the chalcogen derived pocket at the Γ point due to the opening of the p/d gap mentioned in chapter 7.2. The images exhibit clearly the two-dimensional character of the niobium derived band which is nearly straight in the k_{\perp} direction. The lower image shows a cut through the Brillouin zone at a higher binding energy of $E_B = -1.4$ eV. We can observe

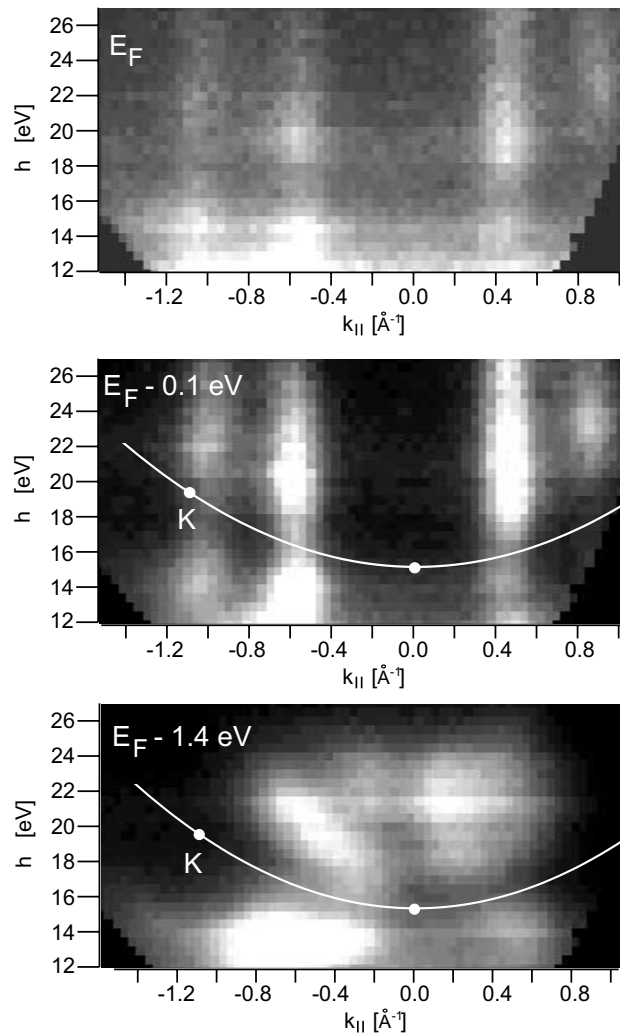


Figure 7.8: Vertical cross-sections through the bulk Brillouin zone of $(\text{PbS})_{1.14}\text{NbS}_2$ obtained by polar angle scans along $K\Gamma K$ at different photon energies. The photoelectron intensity is given in grey scales (white belongs to high intensity) as a function of the $k_{||}$ component of the photoelectrons and the photon energy $h\nu$. The initial state is kept constant for each image at the given binding energy.

distinct emissions originating from sulphur derived bands. They form a regular pattern which is centered at the ΓA line at $h\nu \approx 15.5$ eV, where we can locate the Γ point. If we consider the final states as free-electron like bands the white line represents a line with $k_{\perp} = \text{const}$ with the M points at $k_{||} = \pm 1.0 \text{ \AA}^{-1}$. In contrast to the flat two-dimensional character of the niobium band this image points to a more three-dimensional behavior of the sulphur states. Following the (vertical) ΓA line there are no variations in the photoelectron intensity to be seen. This result is in accordance with the ARPES measurements along this direction (see Fig. 7.6 and 7.7) and can be explained by the special properties of the band structures of the subsystems. In Chapter 5 we have learnt that the valence band maximum of PbS is not located at the Γ point but at the L point of the bulk Brillouin zone. According to Ref. [29] these are the states which are able to participate in covalent bonding and they are located at $k_{||} = 0.75 \text{ \AA}^{-1}$ in reciprocal space which coincides with the region of high intensity in the lowermost panel of Fig. 7.8. Actually the bonding conditions are even

more complex due to the different symmetries of the two subsystems at the interface (see Chapter 2.3). The resulting consequences have been discussed in Chapter 6. However, these measurements are a first experimental hint to covalent bonding in misfit layered compounds which were only predicted from theoretical considerations [29,112] or the exclusion of other bonding mechanisms [111].

Core level analysis

In the previous sections we investigated the valence band structure of the misfit compound $(\text{PbS})_{1.14}\text{NbS}_2$. But also the study of core levels is a valuable tool for understanding interactions between the atoms in a crystal. In Ref. [111] an extensive study of the core levels of different misfit compounds is given. However, these investigations suffer from a poor energy resolution so that line shapes, energetic shifts as well as the splitting up of peaks have not been analyzed. In Fig. 7.9 we present high-resolution core level spectra of the elements that constitute the misfit layered compound. They were measured at a temperature of 20 K and an overall energy resolution of better than 140 meV. The spectra were fitted by four (six in the case of the sulphur core levels) Lorentzian peaks, respectively and convoluted with a Gaussian for taking instrumental and phonon broadening into account. The single peaks are given as dotted lines together with the fitted linear background. The straight line is the sum of all contributions; the difference of experimental and fitted data is shown below the spectra.

The Nb 3d doublet splits into two contributions, the difference in binding energy amounts 350 meV (Nb $3d_{5/2}$) and 550 meV (Nb $3d_{3/2}$) respectively. The ratio of peak areas is 16% for the Nb $3d_{3/2}$ and 30% for the $3d_{5/2}$ peak. Assuming a cationic coupling between the PbS and the NbS_2 layers, i. e. the exchange of Pb atoms through Nb atoms in the PbS layers, we can attribute the two contributions to two different oxidation degrees of the niobium atoms. The respective higher bonded peak can then be ascribed to a valency of 4 for the Nb atoms in the NbS_2 layer, the peak at lower binding energies to a valency of 3 for the Nb atoms in the PbS layers. In Ref. [31] the amount of excess niobium atoms was estimated to 12% which is roughly reflected by the ratio of peak areas. This interpretation must be regarded with great care though. In Ref. [111] the Nb 3d core levels were measured for different misfit compounds as well as for the constituent NbS_2 all of them exhibiting the asymmetry on the low energy side. But the authors admitted that the growth of NbS_2 single crystals was unsuccessful, so that they used powders that were compressed into pellets for their measurements. It is known that NbS_2 tends to selfintercalation of Nb atoms into the van der Waals gap which could contribute to the core level spectra (see Chapter 7.2). The Nb 3d core levels have been measured by K. Rosnagel for NbSe_2 with a higher photon energy $h\nu=950$ eV and a lower energy resolution so that the direct comparison is difficult. Nevertheless, these peaks do not exhibit the asymmetry. In order to exclude effects that depend rather on the kinetic energy than on the binding energy like Auger transitions and satellite peaks from second order excitations the core levels were measured with different photon energies between 300 eV and 600 eV. The four peaks could be seen in all spectra, their intensities not varying significantly with respect to each other.

The sulphur 2p doublet was fitted by six Lorentzians. Nevertheless the agreement between the experimental data and the fit is rather poor. This can be understood due to the incommensurability which should mostly affect the sulphur atoms. Additionally sulphur atoms are constituents of both subsystems. Thus it is clear that they exist in different

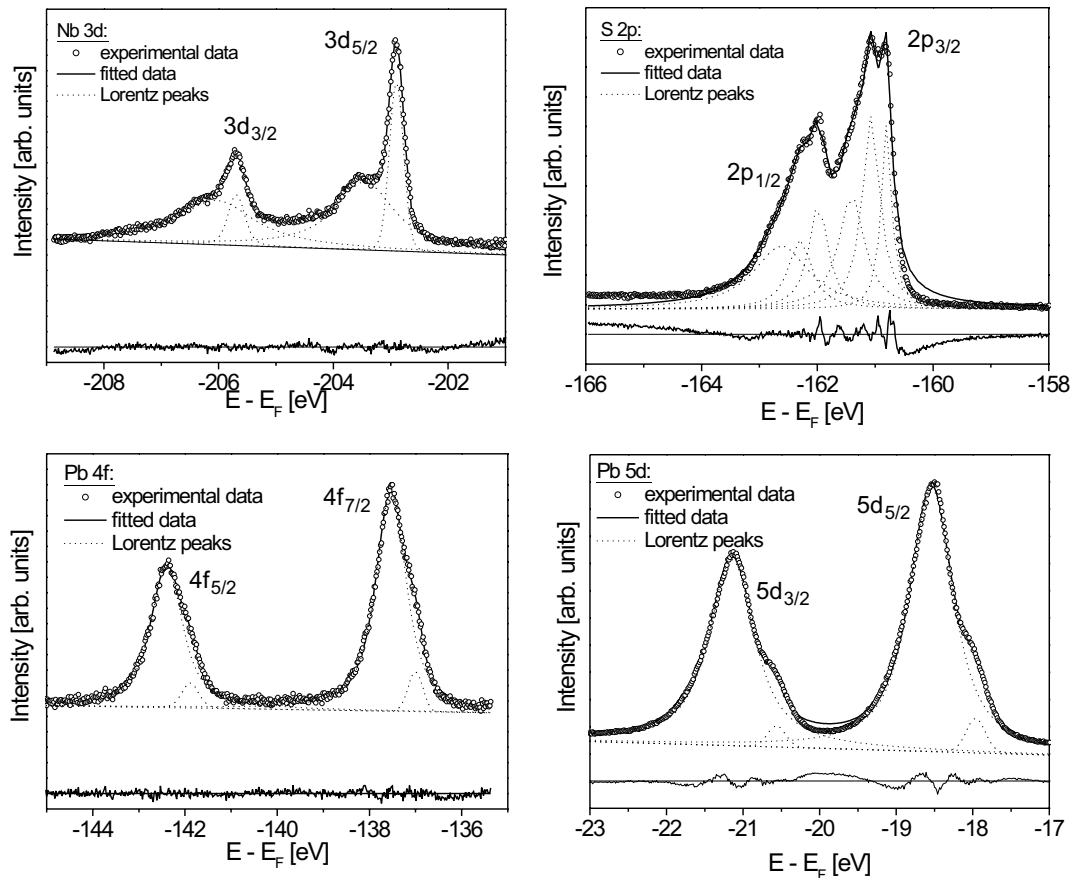


Figure 7.9: Core level spectra of the different elements of the misfit compound: Nb 3d, S 2p, Pb 4f and Pb 5d. The original data is given as circles while the fit with four or six Lorentzian peaks is represented as straight line, the single peaks are shown as dotted line. Below the spectra the difference between experimental and fitted data is indicated. The excitation energy is $h\nu=273.4$ eV for Nb 3d and Pb 4f, $h\nu=215.5$ eV for S 2p and $h\nu=79.0$ eV for Pb 5d.

chemical environments which is mirrored by different energy shifts.

The Pb 4f doublet yields two strong Lorentzian peaks depicted in the lower left panel of Fig. 7.9. Clearly an asymmetry on the higher energy side of both peaks can be observed. Fitting them with two more Lorentzians and adding them to the main peaks results in a very good agreement between the fit and the experimental data. The ratio of the peak areas is 3.2 % and 3.6 %, the difference of binding energy amounts 510 meV and 530 meV respectively. The second contribution can be seen even clearer in the Pb 5d levels on the right, where the splitting amounts $\Delta E=580$ meV and the ratio of peak areas is 4.9% and 3.8% respectively.

To ensure that the asymmetry is an effect inherent to the misfit compound the 4f core levels of pristine PbS and of $(\text{PbS})_{1.14}\text{NbS}_2$ are depicted in Fig. 7.10. Both measurements were done at room temperature with the same photon energy of $h\nu=273.4$ eV and the same energy resolution. It can clearly be seen that the peaks of the pure PbS are much narrower and symmetric. This is in agreement with Ref. [130], where the Pb 5d levels are

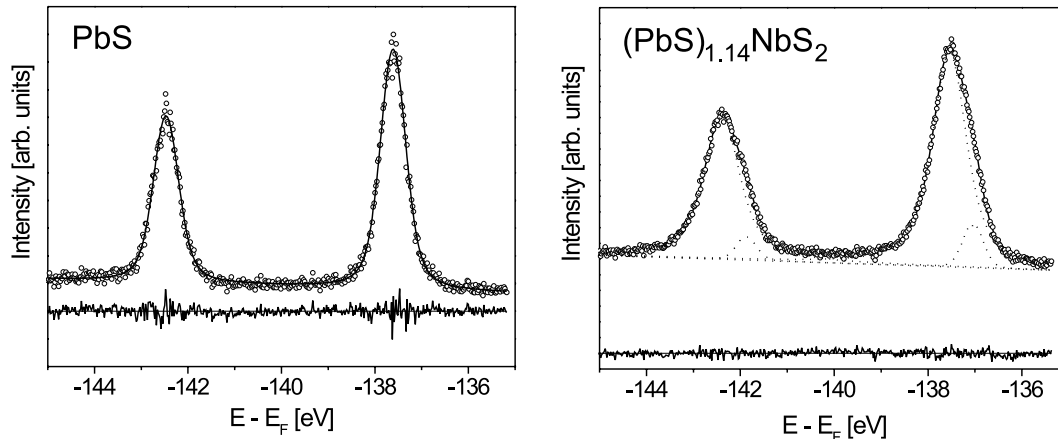


Figure 7.10: *Pb 4f* core levels of *PbS* (left) and of the misfit compound $(\text{PbS})_{1.14}\text{NbS}_2$ (right), measured at room temperature with $h\nu = 273.4$ eV.

studied. They could also be fitted very accurately with two single peaks. For the misfit compound also at room temperature the second contribution to the peaks is clearly visible. In a regular misfit compound (without exchange of cations) all lead atoms have the same chemical environment apart from minor changes due to the incommensurability. But this modulation results only in a broadening of the core peaks, it cannot explain the asymmetry in the peaks. A difference between surface and bulk lead atoms can also be excluded since there is no surface core-level shift in *PbS* [130].

Altogether our XPS studies reveal deviations of the core levels of misfit compounds from the respective core levels of the pure components. Different possibilities to explain occurring asymmetries like Auger excitations, second-order satellites or surface effects could be excluded. A cationic coupling could be the origin of the observed characteristics, but core level analysis is a rather indirect and complex method to draw conclusions on stoichiometries so that the results should not be overestimated.

7.3 Conclusions

Summarizing, the obtained results shall briefly be discussed in the context of the three models that were introduced in the beginning. For both misfit compounds $(\text{PbS})_{1.18}\text{TiS}_2$ and $(\text{PbS})_{1.14}\text{NbS}_2$ a filling of the conduction band could undoubtedly be demonstrated and attributed to a charge transfer from the *PbS* layer to the transition metal dichalcogenide subsystem. Apart from the filling of the conduction transition metal (Ti, Nb) band other changes occurred in the electronic structure that are known from intercalated TMDC and that also prove a charge transfer. The experimental results could clearly be confirmed by band structure calculations. The transferred charge gives rise to an electrostatic attraction between the layers, but it cannot account for the mutual modulation of both layers. Furthermore it is uncertain whether the electrostatic bonds are strong enough to explain the high stability. Although the core level studies can be explained by assuming a cationic coupling XPS is a too complex process in order to be regarded as stringent proof. We have also seen that cationic coupling has not to be assumed to explain the filled conduction bands. In

Ref. [29] the contributions of both electrostatic and covalent bonding in $(\text{SnS})_{1.17}\text{NbS}_2$ were estimated from theoretical considerations. The electrostatic interlayer bonding amounts $\Delta E=0.02\text{--}0.2$ eV, while the interlayer covalent binding energy is noticeably larger with $\Delta E=0.84$ eV. By employing a new mode of angle-resolved photoelectron spectroscopy we found the first experimental evidence for a covalent bonding between the different layers and could therewith confirm results that were up to now only obtained theoretically.

8 Epitaxy of PbS on layered TMDC

Contrarily to the usual opinion that the electronic structure of misfit layered compounds is a simple superposition of the electronic states of its constituent subsystems we have found in Chapter 7 that the band structure has suffered changes that go far beyond a superposition and the rigid band model. Some of these changes hinted to the model of regarding misfit compounds as completely intercalated transition metal dichalcogenides with the PbS double layer as intercalant. Other deviations could not be explained in this simple model and were attributed to a covalent interaction between both subsystems.

A promising approach in this context is the creation of a similar system with the same constituting compounds and a similar geometric structure at the PbS/TMDC interface. This is achieved by the epitaxial growth of PbS films on TMDC crystals. With regard to misfit layered compounds they represent a similar system, but they also exhibit fundamental differences that allow to distinguish electronic properties that are unique to misfit samples. The geometric characterization of the PbS thin films on transition metal dichalcogenides and the study of the influence of the preparational conditions are essential requirements to draw reliable conclusions from photoemission results. For this purpose extensive investigations on the geometric structure of PbS films on different substrates were performed by means of scanning tunneling microscopy and electron diffraction. Exemplarily, well characterized samples PbS on TiS_2 were used for the study of their electronic structure and the interaction between the substrate and the epilayer. The comparison of the epitaxial samples with the pure component crystals PbS and TiS_2 on the one hand and with the misfit compound $(\text{PbS})_{1.18}\text{TiS}_2$ on the other leads to new insights concerning the stability of misfit compounds.

In order to avoid immoderate confusion in view of the large number of epitaxial samples the preparations that are introduced in the following are summarized in Table 8.1. The parameters are given for each preparation and the corresponding measurements are referenced so that they can easily be found.

no.	substrate	t_{exp}	T_{sub}	STM	LEED	ARPES
6	TiS_2	10 min	RT	Fig. 8.1(a), (b)		
12	TiS_2	5 min	100°C	Fig. 8.2(a)	Fig. 8.3(b)	Fig. 8.7(a), 8.10(b), 8.11(b), 8.12
7	TiS_2	10 min	100°C	Fig. 8.1(c)		
9	TiS_2	15 min	100°C	Fig. 8.2(c)	Fig. 8.3(c)	Fig. 8.7(b), 8.12
17	TiS_2	15 min	100°C			Fig. 8.8(b), 8.13
11	TiS_2	30 min	100°C	Fig. 8.2(d)	Fig. 8.3(d)	Fig. 8.7(c), 8.8(b), 8.12
8	WSe_2	10 min	RT	Fig. 8.5		
14	TaS_2	5 min	RT	Fig. 8.6(a)	Fig. 8.6(b)	

Table 8.1: Overview over the epitaxial samples PbS on transition metal dichalcogenides that will be introduced within this chapter. The parameters for each preparation are given and the corresponding measurements are referenced.

8.1 Geometric structure of epitaxial thin films of PbS

Geometric characterization of PbS films on TiS_2

The first step in order to investigate thin films of PbS on layered crystals is to determine their geometric structure, since electronic properties are strongly dependent on layer thickness and the growth mode of the epilayers as it was pointed out in Ref. [131]. There, PbS was deposited on the III/V compound InP. The layer thickness was measured with a quartz crystal thickness monitor during growth, the growth mode was determined by means of XPS. Both methods are rather indirect and uncertain. A more precise method to characterize the growth of PbS films and their geometric structure can be achieved by scanning tunneling microscopy. In the following the influence of various growth parameters such as the temperature of the substrate, the time of PbS exposure and the use of different substrates shall be investigated by means of STM.

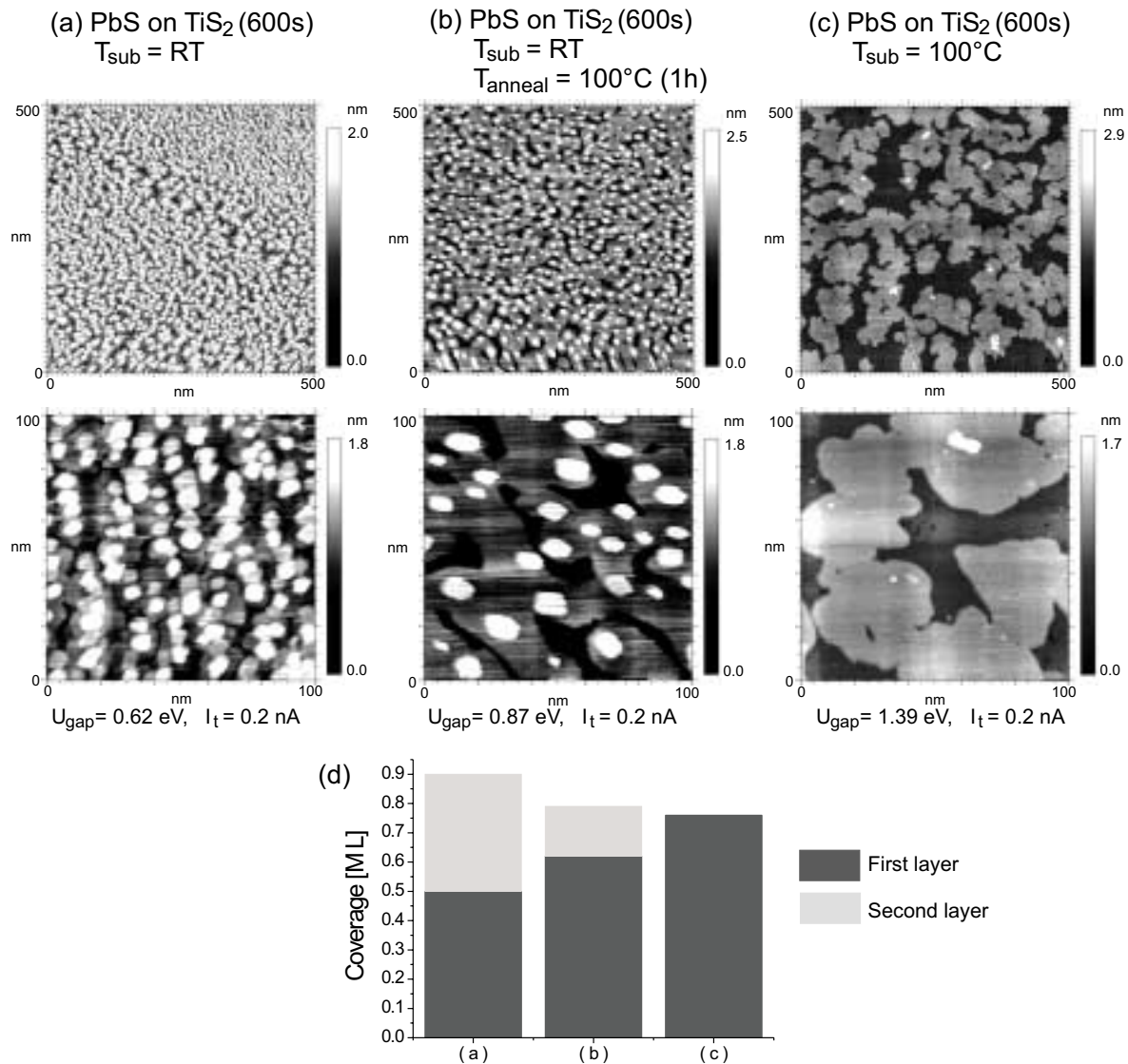


Figure 8.1: (a)-(c) STM images of thin PbS films on TiS_2 produced with various substrate temperatures. (d) Analysis of the PbS coverage of the samples.

All epitaxial samples that are introduced in this chapter were produced in the deposition chamber that was described in Chapter 3.4 with the effusion cell which was constructed in Ref. [50]. Each substrate crystal was analyzed by STM and LEED before the deposition of PbS in order to ascertain a sufficient quality of the surface. After growth they were transferred immediately into the STM chamber. Several samples were reinvestigated days or even months after growth exhibiting no indications of surface contamination or degeneration.

Fig. 8.1 displays STM images of different samples PbS on TiS₂ that give information about the influence of the substrate temperature T_{sub} . All the other parameters as time of exposure (10 min) and PbS flux adjusted by the temperature of the effusion cell $T_{eff} = 570^\circ\text{C}$ were kept constant. The coverage of the TiS₂ samples with PbS was determined from the STM images as it is described in Ref. [9, 50]. The first sample (a) was prepared at room temperature. The TiS₂ surface is covered with small evenly distributed islands of PbS. It can be seen in the lower STM image that on every island of the first layer (grey) the growth of a second layer (white) has already begun. Exactly the same sample was annealed afterwards at 100°C for one hour and reinvestigated by STM. The results are depicted in Fig. 8.1 (b). The small islands of the first layer have grown covering now a larger fraction of the substrate. They seem to have formed a continuous plane with holes where the substrate can still be seen. The coverage in the second layer is strongly decreased. The last TiS₂ sample of this series was heated to 100°C before PbS was deposited. Here, the first layer of PbS forms still larger islands that seem to have merged into a few continuous areas that can hardly be separated. The coverage of the second layer is negligibly small. Fig. 8.1 (d) depicts the analysis of the coverage derived from these STM measurements. It confirms more quantitatively the results that we already estimated before. The highest absolute coverage of 90% was obtained for the sample of Fig. 8.1 (a) which was grown at room temperature. The amount of PbS in the first layer is with 0.5 nominal monolayers (ML) only slightly larger than in the second layer (0.4 ML) indicating a three-dimensional growth. After annealing at moderate temperatures the coverage in the first layer increases significantly to the disadvantage of the second layer. The deposition of PbS on a heated substrate leads to a still higher coverage in the first layer, the island growth in the second layer has not begun yet. The total amount of PbS decreases from the RT sample (a) over the annealed sample (b) to the heated sample (c). Obviously a temperature of 100°C is already sufficient to reactivate the PbS molecules, they can diffuse over the surface and overcome step edges in order to form larger continuous islands. A certain fraction of the PbS molecules re-evaporates into the vacuum. These observations demonstrate the weak interaction between the substrate and the epitaxial PbS layer. A three-dimensional growth can be prevented by increasing the substrate temperature and a layer-by-layer growth is achieved.

The dependence of the PbS coverage from the time of exposure is demonstrated in Fig. 8.2. The STM images (a)-(d) are taken from samples that were produced under the same conditions ($T_{sub}=100^\circ\text{C}$, $T_{eff}=570^\circ\text{C}$), only the preparation time was varied. Except for the first picture we can see clearly the shape of the PbS islands in the STM images: large continuous planes in the first layer ((b) and (c)) as well as in subsequent layers (d). The STM images were analysed in view of the coverage of the single layers. In Fig. 8.2 (e) the amount of PbS in the single layers is given for each sample. Regarding sample (a) it is clear that the preparation was not successful with respect to a layer-by-layer growth. A considerable amount of PbS can be found in the second layer although the first layer is not

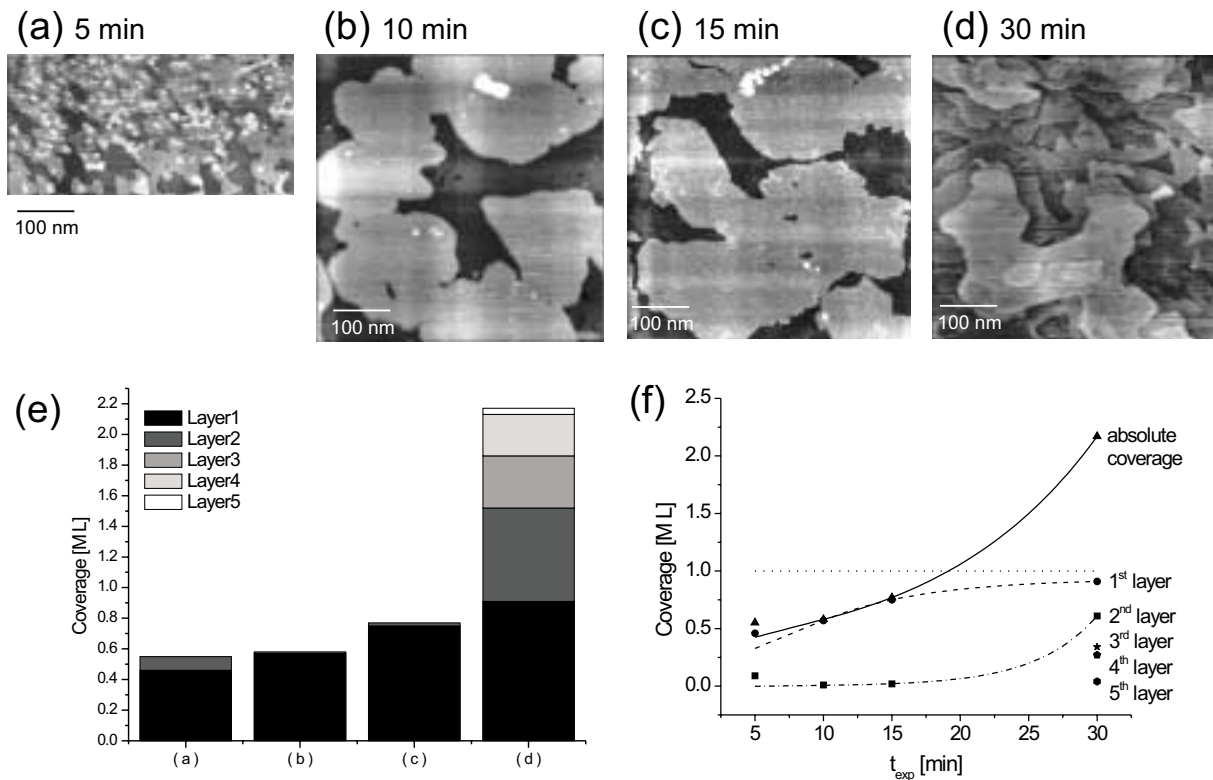


Figure 8.2: Dependence of the PbS coverage from time of PbS deposition. STM images of samples that were exposed to PbS for (a) 5 min, (b) 10 min, (c) 15 min and (d) 30 min. The coverage in the single layers is depicted in (e) for these four samples. The data is presented as a function of time in (f).

completed at all. It is likely that the substrate had not reached a sufficient high temperature. Sample (a) has therefore not been taken into account for the following considerations limiting the analysis to three samples which is certainly not enough to draw stringent conclusions. Nevertheless, we can follow some trends in Fig. 8.2 (f). The total amount of adsorbed PbS is not linear with the time. This can either be explained by assuming the effusion cell not to deliver the same amount of PbS over the time. Since the cell has always been heated over a period of at least 10 minutes and the shutter was not opened before the effusion cell had undoubtedly reached operation temperature this explanation is not likely. We can rather assume the cause being inherent to the growth process. The increase of the adsorbed PbS with time is stronger than linear and hints to a higher probability of the PbS molecules to stick to other PbS molecules than to the TMDC substrate. We will come back to this point later in context with the bonding between PbS and TiS_2 that was studied by means of photoelectron spectroscopy (see Chapter 8.2). Despite the uncertainty due to the limitation on three data points it can be seen that the growth of the first layer is different from the subsequent layers. While the first layer is nearly completed before the second layer starts to grow the third, fourth and fifth layer growth begins earlier leading to a more three-dimensional growth mode. However, for a more detailed analysis of the growth mode the data set is too small. Furthermore, it is not relevant for the interpretation of photoemission data in the following chapters.

Atomic model of epitaxial PbS on transition metal dichalcogenides

So far we have investigated PbS thin films on a more mesoscopic scale with regard to the island shapes and multi-layer growth. In order to get insight into the microscopic structure, i. e. the arrangement of the lead and sulphur atoms of the PbS epilayer with respect to the substrate, electron diffraction and microscopy techniques were used.

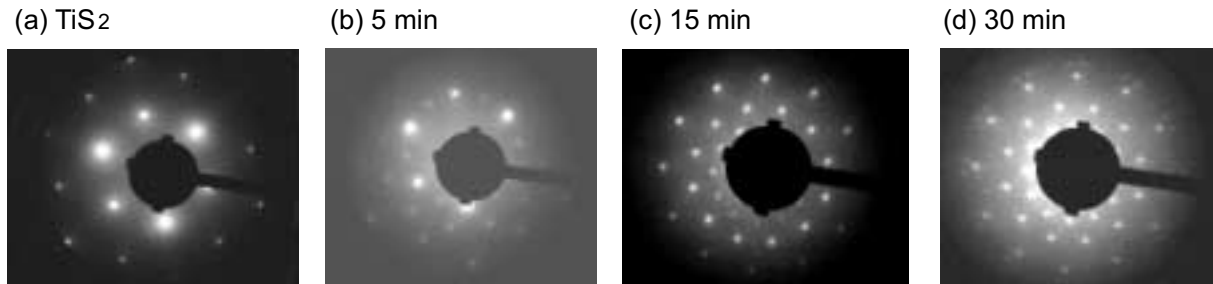


Figure 8.3: LEED patterns of pure TiS_2 (a) and of epitaxial PbS on TiS_2 , deposited within 5 min (b), 15 min (c) and 30 min (d) on the heated substrate. The energy of the electrons is 100 eV for each measurement.

All of the epitaxial samples exhibited the same LEED patterns, no matter whether PbS was deposited onto the substrate at room temperature or at higher temperatures. The sharpness of the spots indicates the high quality of the epitaxial thin films and ensures the crystalline growth of PbS on TMDC substrates. Only the intensity of the different spots depends on the amount of deposited PbS. In Fig. 8.3 LEED measurements of a pure TiS_2 sample and epitaxial samples of different coverage are presented. For the sake of better comparability all measurements were performed with electrons of a kinetic energy of 100 eV. In the LEED pattern of the sample with the lowest PbS coverage (b) we can clearly identify the reflections that originate from the underlying substrate (a). Additional spots from PbS islands are of lower intensity. With increasing coverage these spots get brighter and more reflections can be recognized.

From these patterns we can deduce the geometric structure of the PbS epilayer and its orientation with respect to the substrate. The results were confirmed by transmission electron microscopy¹¹ and are depicted in Fig. 8.4. For comparison the LEED pattern is shown again in (a). If PbS grows with its fourfold (001) surface on the hexagonal TiS_2 (0001) surface three equivalent directions of the substrate exist that are rotated by 120° to each other. Assuming three domains of the PbS layer with lattice constants close to $\sqrt{3} \cdot a_{\text{TiS}_2}$ as it is in misfit compounds (see Fig. 2.4) the LEED pattern can be reconstructed according to Fig. 8.4 (b). In this image similar small circles belong to the same domain of the PbS layer. The three domains are thus represented by black, white and grey circles respectively. Each of them forms an independent quadratic pattern which coincides with the LEED pattern of pure PbS (see Fig. 4.8 (b)). Larger circles represent the hexagonal reciprocal lattice of the TiS_2 subsystem. The reciprocal unit cells of all three PbS domains are depicted as solid black, dashed and grey quadrates, also the hexagonal reciprocal unit cell of TiS_2 can be seen. The reconstruction under the above mentioned assumption is in perfect agreement with the experimental LEED pattern. The resulting geometric structure in direct space is sketched in Fig. 8.4 (c). White circles denote the sulphur atoms of the TiS_2 substrate, while

¹¹Collaboration with E. Yücelen, E. Spiecker and W. Jäger, DFG Forschergruppe 412/21

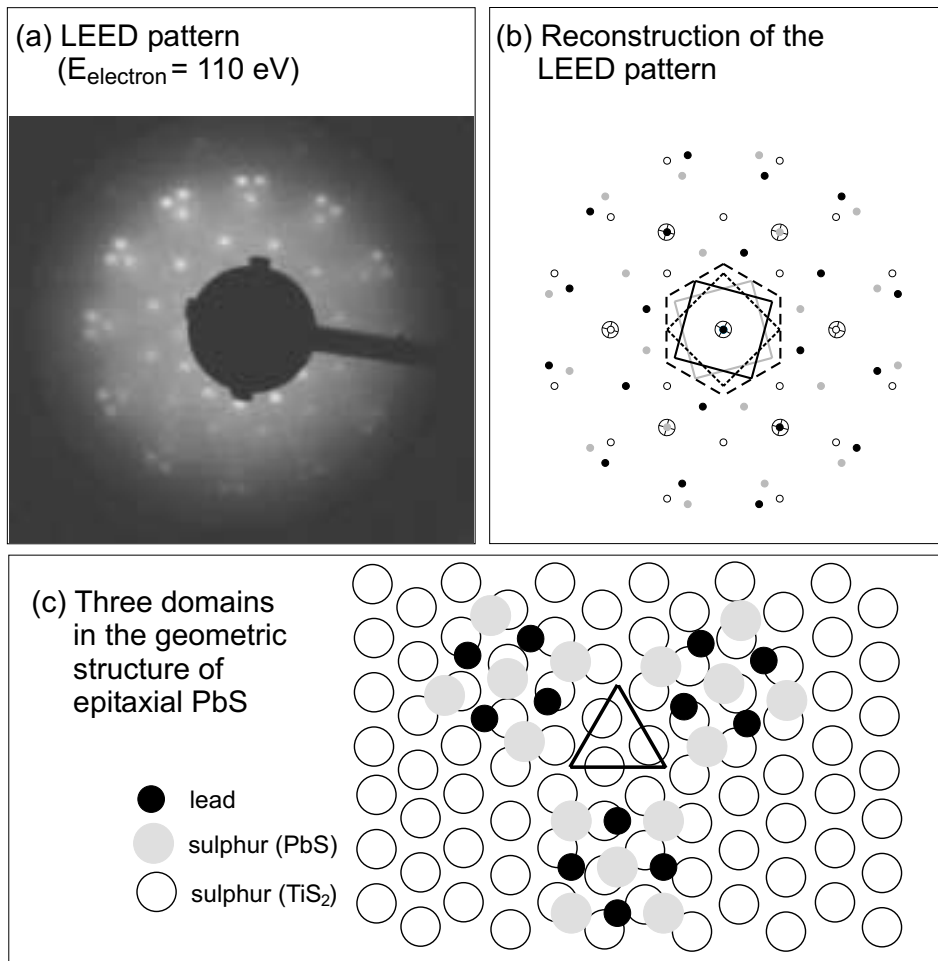


Figure 8.4: (a) LEED pattern of epitaxial PbS on TiS_2 measured on the sample of Fig. 8.2 (d). (b) Reconstruction of the LEED pattern assuming the three domain structure of the PbS film in (c). Spots belonging to the same domain of PbS are denoted as small black (white, grey respectively) circles. Spots originating from the TiS_2 subsystem are marked with larger circles. The reciprocal unit cells are indicated for the hexagonal TiS_2 subsystem as well as for the three domains of PbS (squares). (c) Three domain structure of the PbS epilayer on TiS_2 . The triangle indicates the three commensurate directions (see text).

grey circles represent the sulphur atoms of the PbS epilayer, smaller black circles represent lead atoms. Again the three domains can be recognized. The atoms of each PbS domain are arranged on the substrate in a way that one lattice constant matches commensurately to the TiS_2 layer indicated by the sides of the central triangle that comprises the three 120° angles by which the domains are rotated with respect to each other. The second lattice constant of each domain is then incommensurate to the underlying lattice. Regarding only one of the three domains we arrive at the arrangement of the PbS layer according to the geometric structure of misfit layered compounds (see Fig. 6.1). In this context it is worthwhile to remember that the PbS layer in misfit compounds is perfectly ordered along one of these directions (see Fig. 4.5) although the geometric conditions resemble strongly those of the epitaxial samples. The discrepancies can be found during growth since epitaxy is a non-equilibrium process where a thermodynamic approach towards stability considerations must fail. In order to explain the growth of PbS on TiS_2 during epitaxy

a kinetic model should be applied. In contrast, misfit layered compounds were grown by chemical vapor transport techniques where thermodynamical considerations are applicable. With regard to the stability we can then assume the CVT grown misfit compounds to be in a configuration that corresponds to a global minimum of the free energy. Contrarily to them the epitaxial films of PbS on transition metal dichalcogenide substrates are less stable, presumably their configuration has found a local minimum of the free energy. These energy considerations will find correspondencies in the electronic structure of both systems and will affect the bonding between the subsystems being different for either the misfit compound and the epitaxial PbS films.

PbS thin films on other TMDC substrates

PbS on WSe₂ We shall now come back to the question that arised in Chapter 4.1. It was mentioned there that no misfit compounds containing a semiconducting TMDC as second subsystem could be grown by CVT. No such compounds are known in literature either.

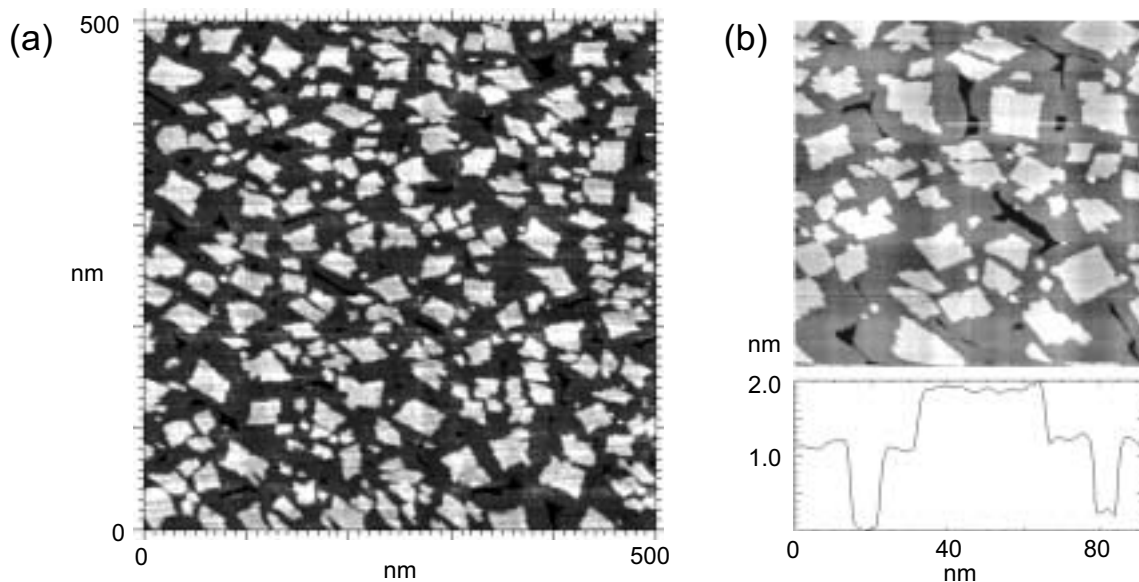


Figure 8.5: *STM images of epitaxial PbS on the semiconducting TMDC WSe₂ and height profile along the white line of the right image ($U_{gap}=1.52$ V, $I_t=0.2$ nA (occupied states)).*

In Fig. 8.5 the successful growth of PbS islands on the semiconductor WSe₂ is shown. The large scale STM image on the left exhibits PbS islands in the first and second layer that were grown by epitaxy at room temperature during 10 min. The total coverage amounts 1.4 nominal monolayers and is therewith even larger than for PbS on TiS₂ with the same preparation conditions (see Fig. 8.1 (a) and (d)). The first layer is nearly complete (0.96 nominal monolayers) while the second layer consists of numerous islands (0.43 nominal monolayers). The height profile along the white line in Fig. 8.5 (b) clearly reveals both layers. The layer thickness can be determined from the second layer ¹² to $d \approx 0.7 \pm 0.2$ nm which is in agreement with the lattice constant of PbS $a = 5.93$ Å [132]. Comparing the

¹²The first layer appears to be higher because height information obtained from STM is a mixture of topography and density of states. WSe₂ is a semiconductor with a larger band gap than PbS and a lower density of states in the vicinity of the Fermi level. Therefore, the tip is approached closer to the sample surface before the feedback loop is activated.

growth to the epitaxial films on the metallic substrates TiS_2 and also TaS_2 (see below) we can state a higher coverage of the first layer of PbS directly adjacent to the substrate with respect to the second layer. This fact hints to a stronger interaction between PbS and a semiconducting substrate compared to metallic substrates although this behavior seems to contradict the results from the CVT growth. The contradiction can be solved by assuming different bonding mechanisms in CVT grown misfit compounds and epitaxially produced PbS layers on TMDC.

PbS on TaS_2 The third MBE grown system that was investigated within this thesis deals with a very low coverage of PbS on the charge density wave system TaS_2 . Due to their quasi-two-dimensional character transition metal dichalcogenides tend to the formation of **Charge Density Waves (CDW)**. A charge density wave is a periodic modulation of the conduction electron density in a metal and is always accompanied by a **Periodic Lattice Distortion (PLD)** of the same periodicity. TaS_2 belongs to the most famous CDW systems since it exhibits an interesting phase transition behavior and CDW are established already at room temperature. Therefore, this system has extensively been studied [133–135], a comprehensive introduction into this topic can be found exemplarily in Ref. [45]. Charge density waves can be influenced by different means, e. g. the phase angle of the CDW can be pinned by defects [136] or the CDW superlattice is changed by electrochemical intercalation [137,138]. In our context the most interesting changes occur upon the formation of nanowire networks on the TaS_2 surface [139–141]. It is found there, that the transformation of the CDW superstructure from the $(\sqrt{13} \times \sqrt{13})R13.9^\circ$ for the clean surface to $c(2\sqrt{3} \times 4)\text{rect.}$ or 3×3 is driven by stress which is induced by the nanowires. The newly obtained superstructure depends on the type of network that is applied onto the TaS_2 surface. In other words, the CDW superstructure is an excellent indicator for the applied stress on a TMDC surface.

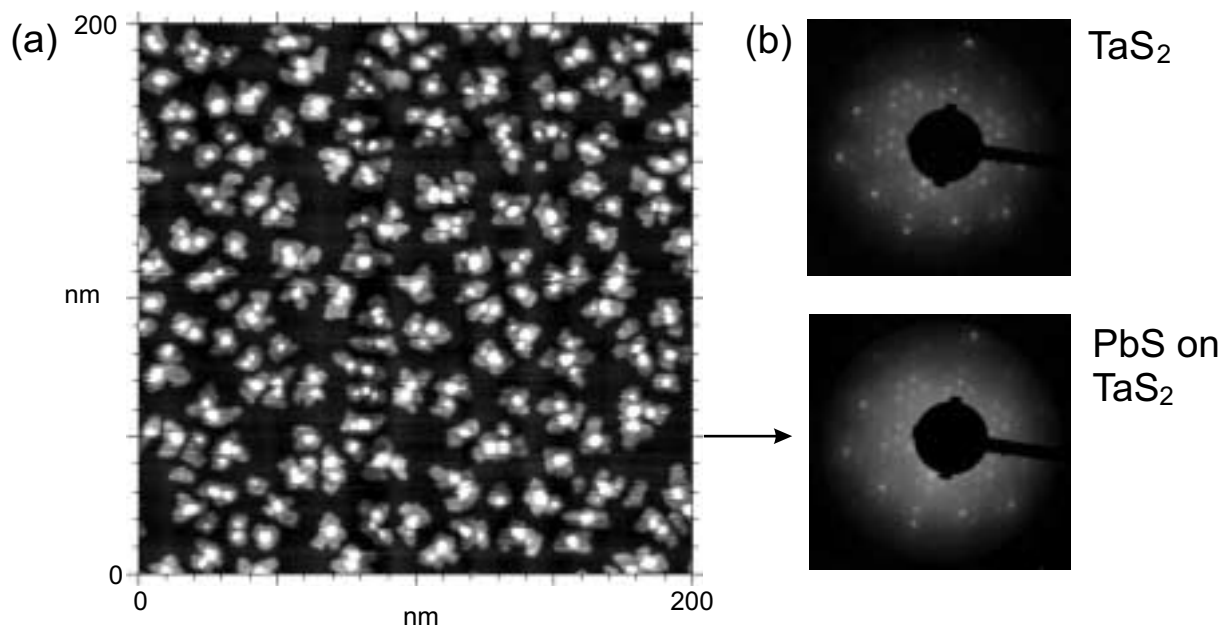


Figure 8.6: (a) STM image of epitaxial PbS on TaS_2 ($U_{\text{gap}}=1.41$ V, $I_t=0.2$ nA (occupied states)). (b) LEED patterns of the sample before (upper image) and after (lower image) the deposition of PbS ($E_{\text{electron}}=150$ eV).

The main interest in the PbS/TaS₂ sample was therefore laid on the influence on the substrate. Only a small amount of PbS was deposited onto the TaS₂ substrate at room temperature within 5 min. The result can be seen in the STM image in Fig. 8.6 (a). Although the coverage is very low indeed a second layer has already begun and indicates a different growth of PbS on metallic substrates in contrast to semiconducting substrates (see above). The uncovered fraction of TaS₂ is still large enough to clearly observe the diffraction pattern of the superstructure in LEED (Fig. 8.6 (b)). The upper image shows the LEED pattern of the clean TaS₂ surface. We can clearly identify the spots that reflect the above mentioned $(\sqrt{13} \times \sqrt{13})R13.9^\circ$ superstructure belonging to the nearly commensurate CDW phase of TaS₂ at room temperature. The lower image is taken from the epitaxial sample. It coincides perfectly with the upper pattern, no deviations can be found. It is evident that the PbS coverage is too low to be observed in LEED when we remember the LEED measurement of the PbS/TiS₂ sample with the lowest coverage. The spots originating from the PbS epilayer were rather weak there, although the absolute coverage was much higher than in this case. All reflections can be attributed thus to the TaS₂ substrate which has suffered no changes, in particular the PbS islands do not affect the CDW superstructure. We can therefore state that contrarily to misfit compounds the TMDC layer is not modulated by the PbS epilayer. The driving force for the modulation in misfit compounds can be excluded for epitaxial PbS films on TMDC substrates.

8.2 Electronic structure of epitaxial PbS films on TiS₂

We have already seen in the previous chapter that the type of bonding between the different subsystems of misfit compounds appears to be fundamentally different from the bonding between epitaxial PbS films on TMDC substrates. The most direct technique to investigate the stability of crystals that can be deduced from their electronic properties is the angle-resolved photoelectron spectroscopy. On the other hand we have learnt that the PbS epilayer consists of three domains that are rotated by 120° with respect to each other. From TEM dark field measurements [74] we know that these domains are rather small with less than 100 nm in diameter. This is by magnitudes smaller than the spot of light that is used in photoemission experiments. Consequently ARPES measurements average over numerous domains and the analysis of band dispersions of PbS derived states along directions parallel to the surface is very complex if not impossible. Nevertheless special photoemission modes remain that can be applied to these complex systems which yield reliable information.

Symmetries in the electronic structure

As a first approach to the electronic structure the angular distribution of the photoelectrons (PAD, see Chapter 3.1) was measured which yields information about the symmetry of electronic states in reciprocal space. Fig. 8.7 depicts PADS from three different samples that had been characterized by means of STM and LEED before (see Fig. 8.2 and 8.3). The electrons were excited with a photon energy of $h\nu = 21.22$ eV from the indicated initial states and detected in dependence of their emission angles. In the images the emission angles have already been transformed into the layer parallel component of the wave vector of the photoelectrons $k_{\parallel,x}$ and $k_{\parallel,y}$ according to Equation 3.5.

With increasing coverage the photoelectron intensities change drastically. Starting with the lowest coverage in (a) we can ascribe the emissions to the underlying substrate TiS₂ whose

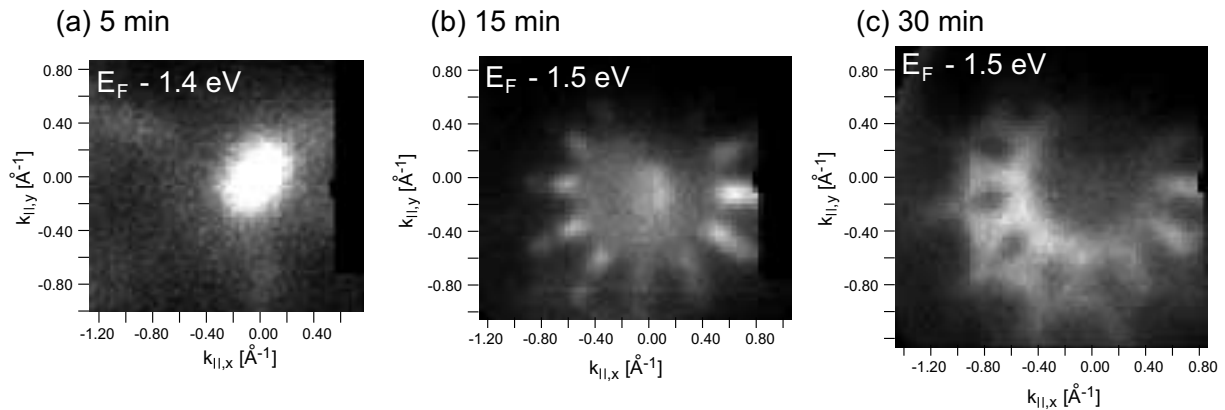


Figure 8.7: Polar angle distribution (PAD) images from samples with different coverage of PbS that were introduced in Fig. 8.2. The electrons were excited with a photon energy of $h\nu = 21.22$ eV from the indicated initial states which are located nearly at the same binding energy for each sample.

valence band reaches a maximum at the Γ point, i. e. in the center of the Brillouin zone at $k_{\parallel} = 0$ (see Chapter 7.1). Very weakly we can distinguish emission features towards the borders of the Brillouin zone that exhibit a sixfold symmetry which is characteristic for the TMDC substrate as well. The strong emission in the Brillouin zone center gets weaker with increasing coverage and has finally lost intensity completely in Fig. 8.7 (c). In return, new emissions appear stretching from the center outwards. They form a regular pattern with a quasi-twelfold symmetry. With higher coverage these structures get more intense, the twelve arms are connected inwards by a ring, smaller rings are formed at the outer sides of each arm. A closer look on the latter sample is given in Fig. 8.8 (b) where it is compared with the corresponding electronic states of pure PbS (a). The surface Brillouin zone of the PbS (001) surface is presented in the first image. A difference of 0.1 eV between the initial states of both samples was chosen because of an energetic shift of the spectra of the epitaxial sample with respect to pure PbS (see next chapter). With the knowledge about the geometric structure of the epilayer we can explain the photoelectron angular distributions of the epitaxial sample. As it was expected they can be described as a superposition of the three domains of PbS which is demonstrated exemplarily for the PAD at $E - E_F = -1.5$ eV (-1.6 eV) in Fig. 8.8 (c). The PAD image of PbS was inverted and rotated twice by an angle of 120° and 240° respectively. Then these three images were superposed yielding the middle image. Comparing it to the inverted image of the epitaxial sample we can state a perfect agreement between both images even into detail such as the twelve outer rings or the small spacings between the arms. Accordingly the other images of the epitaxial sample can be reconstructed from the electron distributions of PbS.

Furthermore the exact agreement between the electron distributions of the PbS film and the PbS single crystal indicate the absence of strong interactions between the PbS epilayer and the substrate. The kind of interaction will be determined in Chapter 8.2.

We will now come back to the thinner PbS film on TiS_2 . We have already seen in Fig. 8.7 (b) that the electronic structure is not completely formed yet, the angular distribution of the electrons differs from the thicker PbS film towards the border of the Brillouin zone. In order to investigate the electronic structure in higher Brillouin zones we measured photoelectron angular distributions with a higher photon energy of $h\nu = 138.2$ eV. The results are depicted

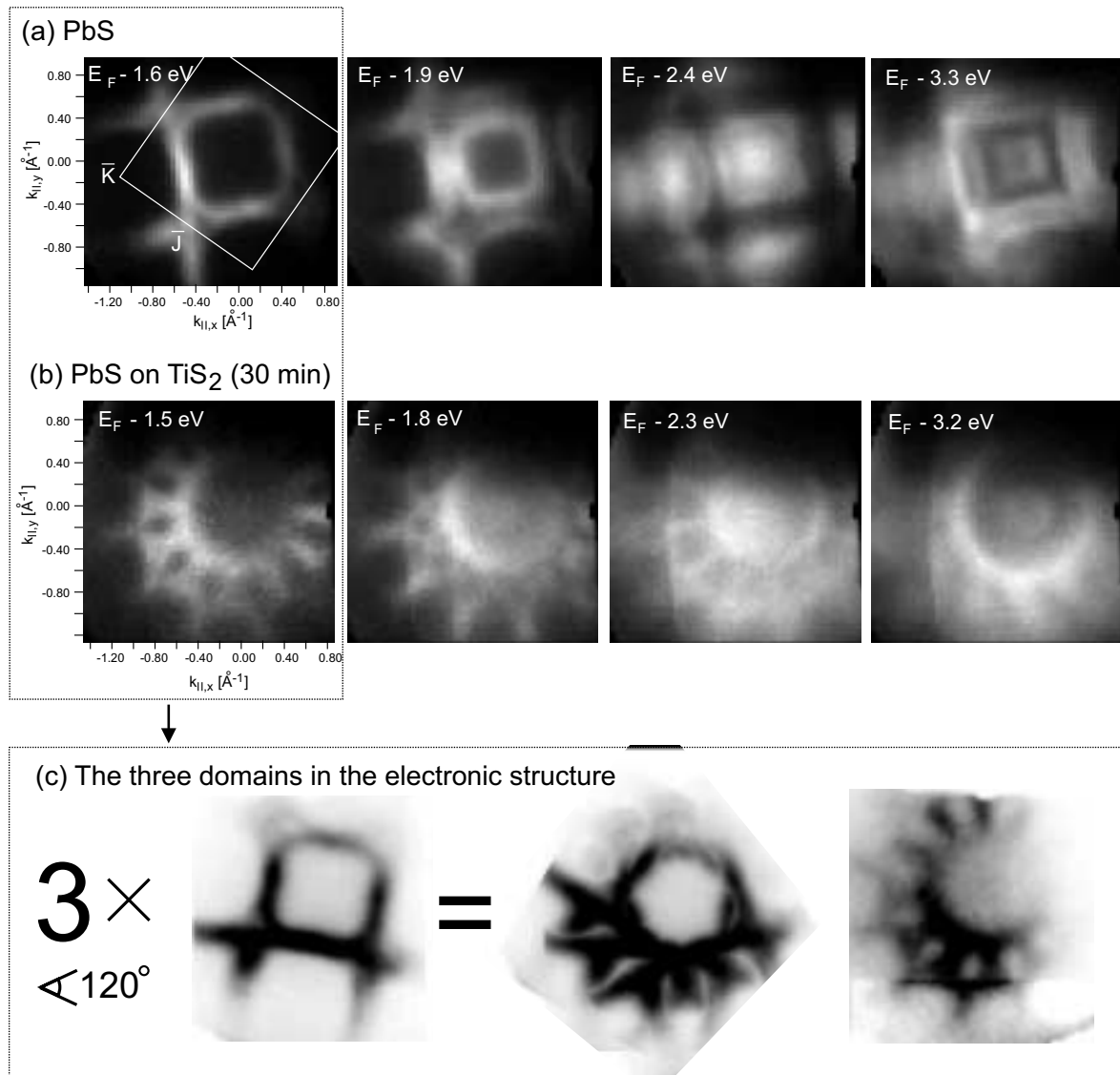


Figure 8.8: Polar angle distributions (PAD) of (a) PbS and (b) PbS on TiS₂ (30 min). (c) Reconstruction of the PAD of the epitaxial sample out of the PAD of PbS (see text)

in Fig. 8.9 (b) where they are compared with the misfit compound (PbS)_{1.18}TiS₂ (a). The misfit compound exhibits very distinct emission structures. We can clearly identify the emissions originating from the filled Ti band near the Fermi energy $E - E_F = -0.1$ eV at the M points of the Brillouin zone. The first Brillouin zone is shown with white lines in each image. At higher binding energies the sulphur derived states give rise to the emissions that form ring structures in the Brillouin zone centers, they are widened with increasing binding energy. Altogether we can distinguish the first and six further Γ points of the extended zone scheme.

Due to the electronic contributions of three domains the photoelectron distributions of the epitaxial sample are more complex. Near the Fermi energy the emissions can be attributed to the underlying substrate, the image resembles the PAD of the misfit compound at the same initial state energy. Similarly we can identify the Ti derived states at the M points of the TiS₂ Brillouin zone indicating a higher filling of these states than in pure TiS₂.

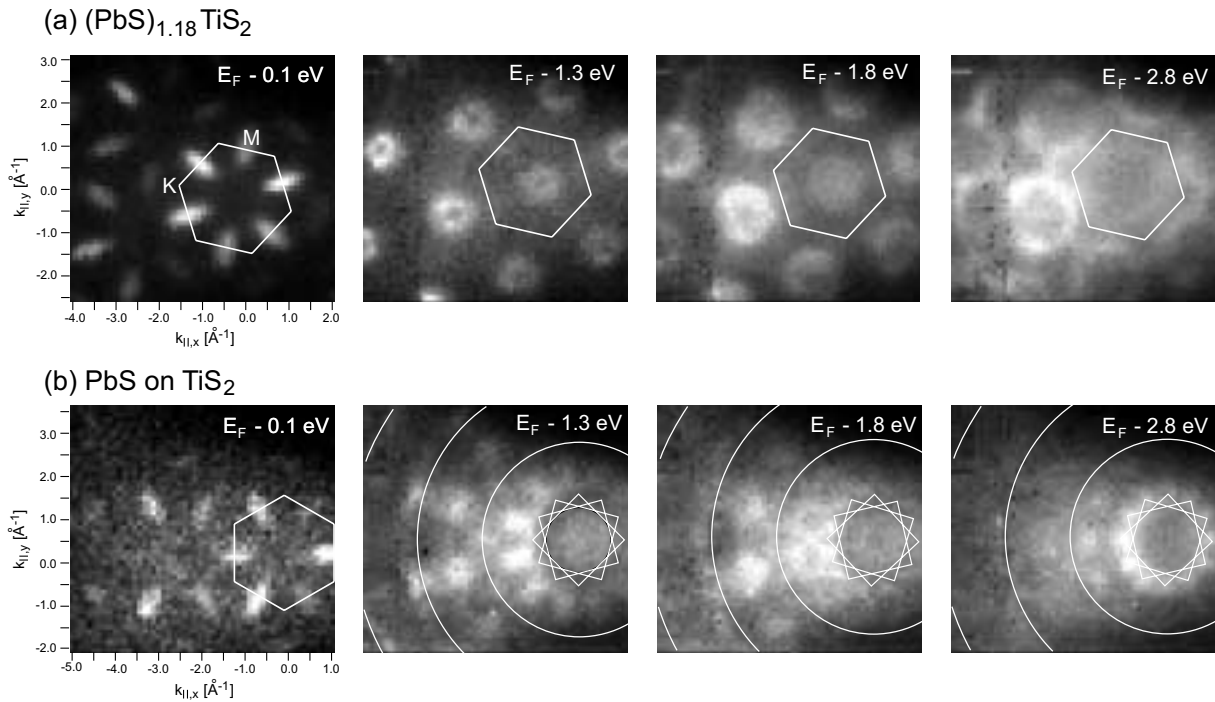


Figure 8.9: Polar angle distributions (PAD) of (a) $(\text{PbS})_{1.18}\text{TiS}_2$ and (b) PbS on TiS_2 . Electrons were excited with $h\nu = 132.2$ eV and yield information about the electronic structure in higher Brillouin zones.

In the next chapter 8.2 it will be demonstrated that these electrons are due to a charge transfer from the epilayer to the substrate, just as it is in the misfit compound. To higher binding energies the emissions originate from the PbS film. Therefore the surface Brillouin zones of the three domains of PbS are indicated instead of the hexagon corresponding to the TiS_2 subsystem. For the sake of clarity the higher Brillouin zones are approximated by concentric white circles that correspond roughly to a combination of all three domains. The structures within the first Brillouin zone that have been seen before (see Fig. 8.7 and 8.8) can not be resolved here. Nevertheless a clear emission pattern can be observed in higher Brillouin zones at $E - E_F = -1.3$ eV. It reflects the quasi-twelfold (3×4) symmetry as we have seen it before. Due to the superposition of three differently orientated domains the electronic structure does not match into one single extended zone scheme. In radial direction from the center of the first Brillouin zone we can distinguish zones of higher and lesser photoelectron intensity though. These emissions match reasonably to the periodicity of the higher Brillouin zones that were approximated by the concentric white circles. At still higher binding energies this periodicity is maintained, the bright spots in the second Brillouin zones exhibit ringlike shapes at $E - E_F = -1.8$ eV. At the highest shown binding energy of $E - E_F = -2.8$ eV the structures get weaker, only a ringlike structure at the border of the first Brillouin zones can clearly be observed.

Comparing the bonding in misfit compounds and epitaxial samples

In this chapter we will return to the question about the type of bonding that acts between the PbS and the TiS_2 layers in epitaxial samples as well as misfit compounds. The purpose of comparing both systems is to determine the changes of the electronic structure in misfit

compounds that reach beyond the changes in the epitaxial films and thus perceive the unique properties of misfit compounds. In Fig. 8.9 we have already recognized a filling of the conduction band of the TiS₂ substrate of an epitaxial sample. At the M points of the TiS₂ Brillouin zone the Ti derived band is shifted below the Fermi energy. For a more detailed analysis of this phenomenon energy distribution curves along the Γ M direction were measured for a submonolayer epitaxial film. In Fig. 8.10 the results are compared to pure TiS₂ on the one hand and to the misfit compound (PbS)_{1.18}TiS₂ on the other, that have already been introduced before (Chapter 7.1).

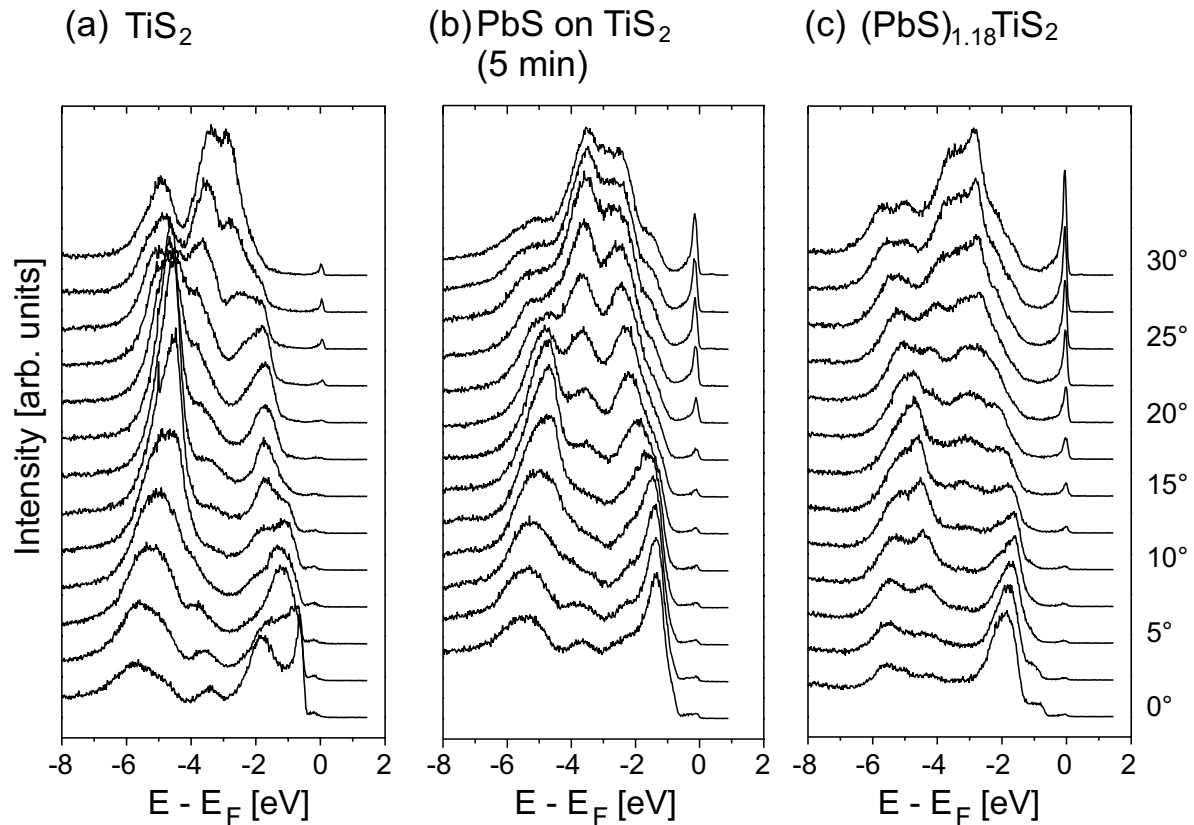


Figure 8.10: Energy distribution curves along the Γ M direction of the TiS₂ subsystem of (a) pure TiS₂, (b) a submonolayer film of epitaxial PbS on TiS₂ ($t_{exp}=5$ min) and (c) the misfit compound (PbS)_{1.18}TiS₂. The photon energy was $h\nu=21.22$ eV in all cases.

The epitaxial sample is the same that was investigated by STM in Fig. 8.2 (a). The directions of high symmetry corresponding to the substrate could precisely be determined by means of photoelectron angular distributions. Most of the emission structures of the epitaxial samples can clearly be attributed to the substrate, in particular the peaks at higher binding energies. The main difference between the three series of spectra concerns again the region near the Fermi level. Similarly to the misfit compound the epitaxial sample exhibits a conspicuous peak towards the M point. Although its intensity is not as high as in (PbS)_{1.18}TiS₂ it clearly indicates a charge transfer from the PbS epilayer to the substrate. In analogy to the conclusions in Chapter 7.1 we can explain the lesser intensity by a reduced amount of transferred electrons since the charge transfer certainly depends on the number of PbS/TiS₂ interfaces. While in the mono- (bi-) layer misfit compound the number of PbS/TiS₂ interfaces per TiS₂ layer amounts two (one) it is further decreased

in the epitaxial sample, because the coverage in the first PbS layer is less than one (see Fig. 8.2 (a)).

In order to analyse the electronic structure of the PbS epilayer itself into more detail than is permitted by electron angular distributions the choice of high symmetry lines is limited to the direction perpendicular to the layers (see above). In Fig. 8.11 energy distribution curves along this direction are presented for the same samples as in Fig. 8.10. They were measured in normal emission with varying excitation energies ($12 \text{ eV} \leq h\nu \leq 28 \text{ eV}$). Assuming direct transitions we can thus map the direction perpendicular to the surface which corresponds to the ΓA line for the TiS_2 subsystem. This assumption is certainly justified for transition metal dichalcogenides and in Chapter 5 it was demonstrated that it can also be applied to PbS, particularly along this special direction.

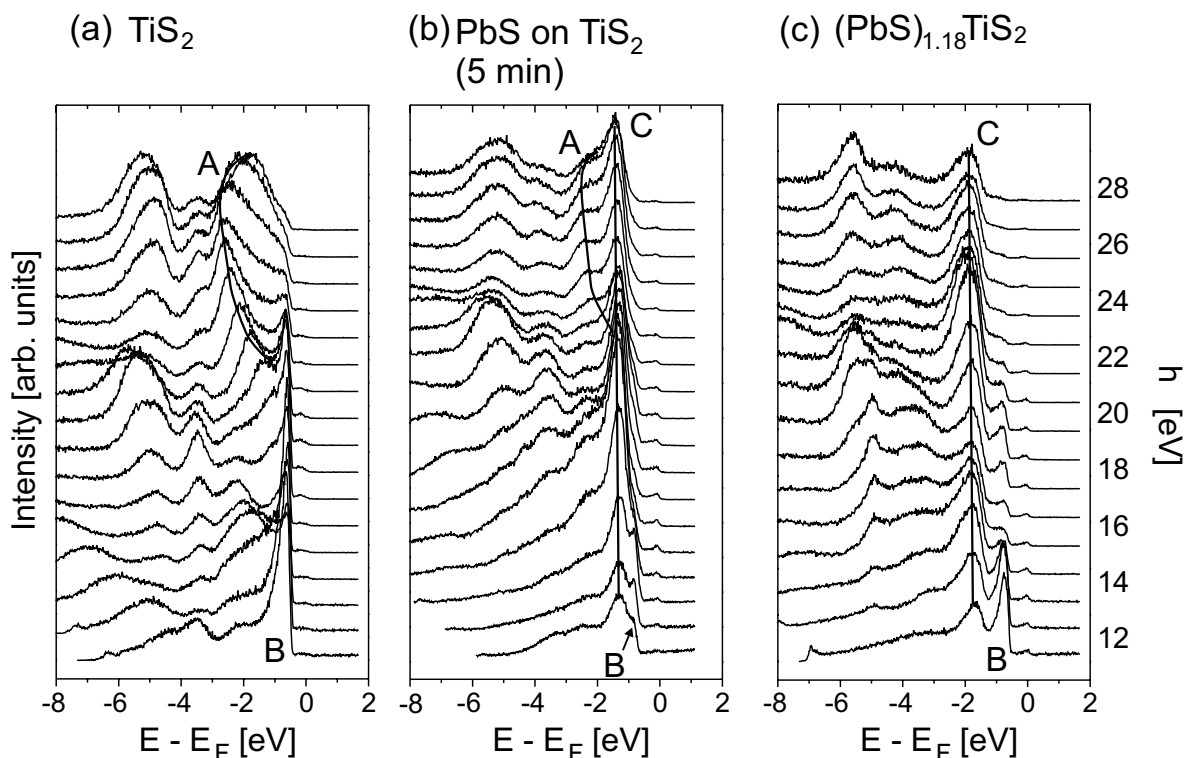


Figure 8.11: Energy distribution curves in normal emission with varying excitation energies of (a) pure TiS_2 , (b) a submonolayer film of epitaxial PbS on TiS_2 ($t_{exp}=5 \text{ min}$) and (c) the misfit compound $(\text{PbS})_{1.18}\text{TiS}_2$.

In the following discussion we will concentrate on the three electronic states that are labelled in the figure by A, B and C respectively. It can clearly be seen that the electronic states A and B originate from the TiS_2 subsystem while the stationary peak C can be attributed to the surface state of PbS (see Fig. 5.2). Peak A has mainly sulphur p_z character and is therefore highly dispersive along ΓA in pure TiS_2 . This state can still be observed in the submonolayer epitaxial sample. The dispersion appears to be reduced here, although this can not be concluded for certain because the peak is hidden by the strong emission C towards lower binding energies. In the misfit compound peak A has either disappeared or the dispersion is so much reduced that it is completely hidden by peak C. The effect of vanishing k_{\perp} dispersion has been observed in transition metal dichalcogenides before, either in intercalation compounds [142] or for TMDC which were decorated with Rb nanowire

networks [139,143]. It was explained by an elevation of the outermost sandwich layer of the respective transition metal dichalcogenide and a decreased overlap of the orbitals orientated perpendicular to the layers. In case of the intercalation compound it was stated that the decoupling of the outermost layer is not sufficient to explain all changes in the electronic structure, but that the assumption of a charge transfer is essential as well. For misfit layered compounds the total loss of layer perpendicular dispersion has already been explained in Chapter 7.2 as a consequence of the large layer separation due to the two atomic slice of PbS inserted into each van der Waals gap. On the basis of the epitaxial sample we can now draw a conclusion the other way round: A charge transfer (proven in Fig. 8.10) is not sufficient to explain the loss of layer perpendicular dispersion.

The second peak B that can unambiguously be attributed to the TiS₂ subsystem is observable in the epitaxial sample and the misfit compound only at lower excitation energies. It shows no dispersion due to its mainly sulphur $p_{x,y}$ character. This state and the PbS derived peak C shall now be investigated into more detail.

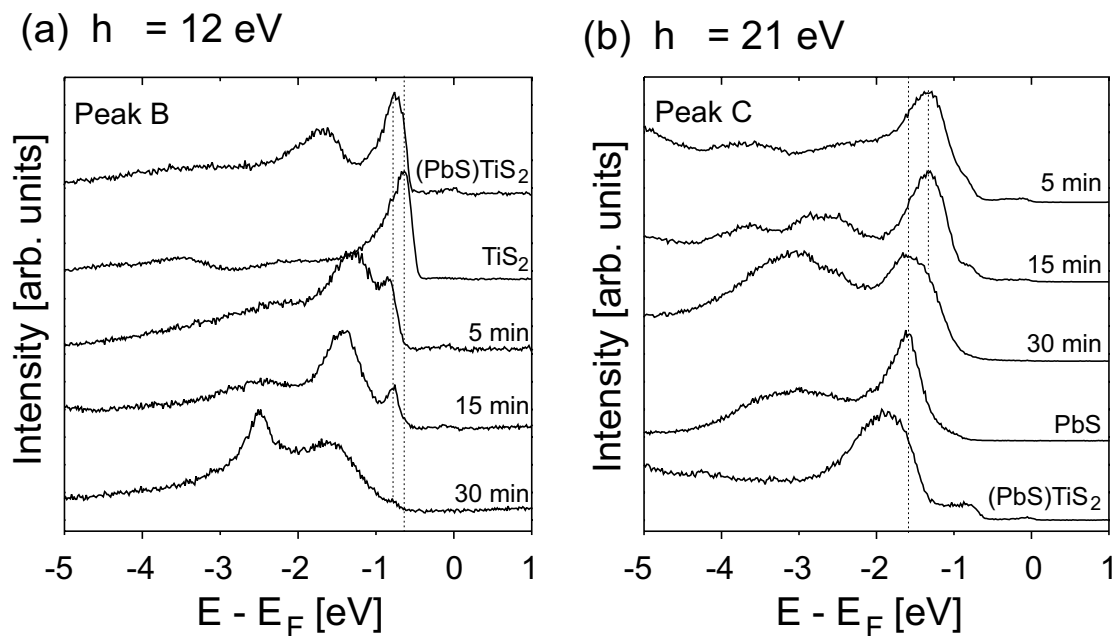


Figure 8.12: Comparison of normal emission spectra for various compounds as they are indicated at each spectrum: the misfit compound $(\text{PbS})_{1.18}\text{TiS}_2$, the pure compounds TiS_2 and PbS and epitaxial films of PbS on TiS_2 with different coverage. The spectra were measured with (a) $h\nu = 12$ eV and (b) $h\nu = 21$ eV

Fig. 8.12 (a) depicts normal emission spectra of several epitaxial samples PbS on TiS_2 in comparison to pure TiS_2 and the misfit compound $(\text{PbS})_{1.18}\text{TiS}_2$. All spectra were measured with an excitation energy of $h\nu = 12$ eV where the TiS_2 derived peak B is best observable, for the highest PbS coverage (30 min) of the epitaxial samples its intensity is very weak though. Compared to pure TiS_2 the spectra of all other samples are shifted to higher binding energies by approximately 150 meV. The shift is simply explicable by the electrons that are transferred from the PbS layers to the TiS_2 subsystem in both misfit compound (see Chapter 7.1, Fig. 8.9 (a)) and epitaxial sample (see Fig. 8.9 (b), 8.10). It is interesting to note that the shift, indicated by the dotted lines, is of the same amount for all epitaxial samples as well as for the misfit compound within experimental accuracy.

The TiS_2 conduction band that is occupied by the additional electrons is nearly flat (see Fig. 7.1 (a)) with a high local density of states and can accept a large number of electrons without causing a larger energetic shift of the spectrum.

Regarding peak C in Fig. 8.12 (b) that was identified as the PbS derived surface state (see Chapter 5) the analysis is more complex. Since the energetic shift of this state with regard to pure PbS occurs in different directions for the misfit compound and for the epitaxial samples it can not be explained simply by the charge transfer. It is a further hint that the bonding mechanisms in misfit compounds and between the epilayer and the substrate in the epitaxial samples are fundamentally different. The spectra of the epitaxial samples with lower coverage (5 min and 15 min) where the PbS contributions stem basically from the first layer of the PbS film are shifted by approximately 250 meV to lower binding energies. This shift can well be explained by the loss of electrons to the substrate in agreement with the shift of the TiS_2 derived peak in the opposite direction in Fig. 8.12 (a). The peak in the spectrum of the sample with higher coverage (30 min) comprises two contributions which coincide in their energetic position with the peak of pure PbS and the peak originating from the first layer of the PbS film respectively. In accordance to the results of the photoelectron angular distributions in Fig. 8.8 we can therefore state, that the electronic structure of the PbS epilayer is completely developed from the second layer on and it is not altered with respect to pure PbS. Contrarily to the epitaxial films, the PbS derived surface state in the misfit compound shifts to higher binding energies by approximately 300 meV. This shift is in contrast to the effect that we would expect to result from a charge transfer and that we observed for the epitaxial PbS films. The peak is very broad though and it is certainly blurred by the contributions of the TiS_2 subsystem. We have also learnt in Chapter 7.1 that changes occur in the valence band of the misfit compound that go far beyond the rigid band model. For a more precise analysis of peak shifts we therefore investigated Pb core levels in Fig. 8.13.

The Pb 5d core levels were measured with a photon energy of $h\nu = 79.7$ eV at room temperature. The original data sets for pure PbS, the misfit compound and a submonolayer PbS film on TiS_2 are depicted in Fig. 8.13 (a). After the subtraction of a linear background the peaks were fitted by a superposition of Lorentz peaks that was convoluted with a Gaussian to take instrumental and phonon broadening into account. For pure PbS and the PbS film it was sufficient to use two Lorentz peaks in order to achieve a satisfying agreement between the experimental data and the fit. For $(\text{PbS})_{1.18}\text{TiS}_2$ on the other hand it was inevitable to add two more Lorentzians. The asymmetry of the peaks can already be seen in the original data and is in agreement with the core level analysis of the other misfit compound $(\text{PbS})_{1.14}\text{NbS}_2$ in Chapter 7.2. The fits of the single peaks of each spectrum are presented in Fig. 8.13 (b). There we can clearly observe two contributions to the Pb 5d peaks in the misfit compound: The energetic position of the small contribution to the higher energy side coincides precisely with the Pb 5d levels of the epitaxially grown PbS layer on TiS_2 . It is shifted by 350 meV to lower binding energies with respect to the core levels of pure PbS which is in reasonable agreement to the shift of the surface state in the epitaxial sample. With the previous results concerning the charge transfer from the PbS film to the sample we can ascribe this contribution to a similar charge transfer in misfit compounds that has already been demonstrated by valence band photoemission studies and that is partly responsible for the attractive interaction between both subsystems in misfit compounds. The second and larger contribution of the Pb 5d core levels of the misfit compound is shifted to higher binding energies by 250 meV with respect to the pure PbS.

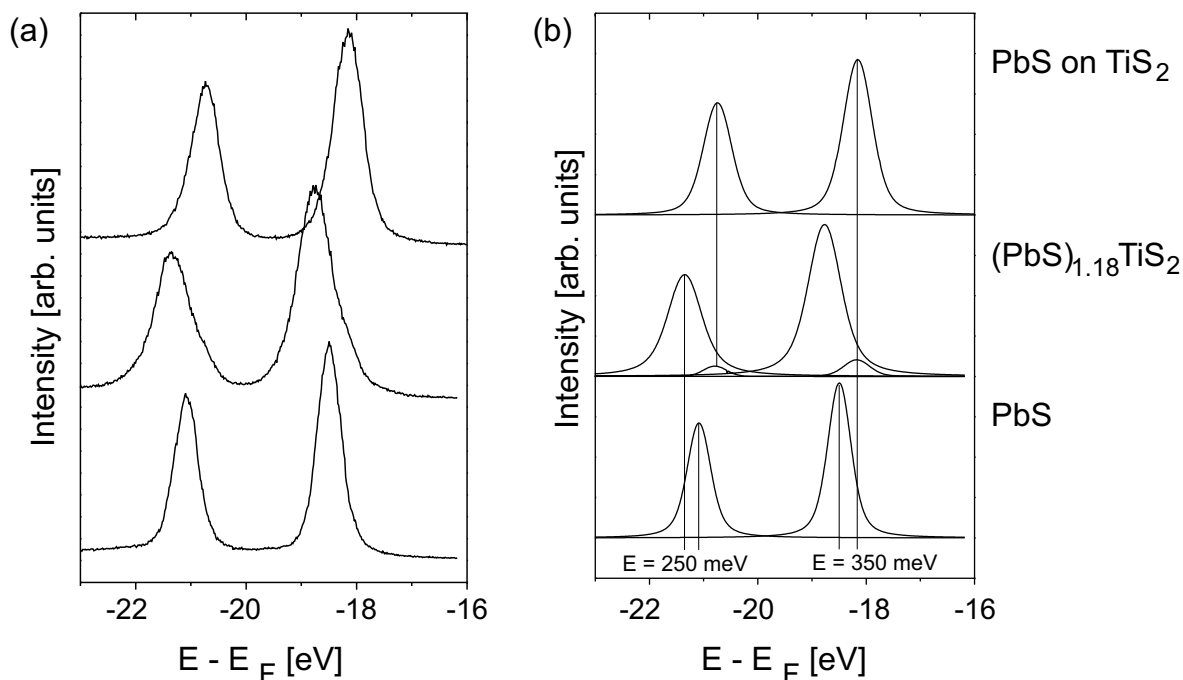


Figure 8.13: Photoemission spectra of the Pb 5d core levels of pure PbS, the misfit compound $(\text{PbS})_{1.18}\text{TiS}_2$ and the epitaxial sample of Fig. 8.9 (b): (a) original data and (b) Lorentz peaks of a least-squares fit.

This shift corresponds to the surface state shift in the valence band of the misfit compound. The lack of this contribution in PbS films indicates a different type of bonding in misfit compounds with respect to the epitaxial sample. With the knowledge from Chapter 7 that covalent bonding is the main mechanism for the large stability of misfit layered compounds we can attribute this contribution to the covalent bonds that are constituted between the lead atoms of PbS and the sulphur atoms of TiS_2 [].

The peaks of the misfit compound are broader than those of PbS and even of epitaxial PbS films (although the atoms are more ordered in the misfit compound than in epitaxial films), because of the varying Madelung potential due to the incommensurability.

8.3 Conclusions

By means of molecular beam epitaxy we prepared thin films of PbS on different transition metal dichalcogenide substrates and characterized their geometric structure by scanning tunneling microscopy and electron diffraction techniques. On all metallic and semiconducting TMDC the PbS epilayers grow with their fourfold (001) surface on the hexagonal substrate surface. Due to the break of surface symmetry at the interface three domains of epitaxial PbS emerge that are rotated by an angle of 120° with respect to each other. Considering only one of these domains the geometric arrangement is equal to misfit compounds. In contrast to misfit compounds it was possible to create heterostructures with a semiconducting TMDC subsystem. Together with the observation that the charge-density wave system of TaS_2 is not influenced by PbS islands on the surface this is a strong evidence that the bonding in epitaxial samples and in misfit layered compounds is of different kind.

The electronic structure of the epilayer can be studied in the high coverage regime (≥ 2 nominal monolayers). Photoemission measurements are characterized by a superposition of the electronic structure of the three domains. The electronic structure of a single domain is not altered with respect to pure PbS. In the low coverage regime (≤ 1 nominal monolayer) the influence of the epilayer on the substrate can be identified as a filling of the conduction band due to a charge transfer from PbS to the TiS_2 substrate. Consequently the electronic states are shifted to higher binding energies.

A detailed analysis of peak positions of both valence states and core levels revealed further discrepancies between epitaxial samples and misfit compounds. While energetic shifts in epitaxial samples could unambiguously be attributed to the charge transfer we could find clear evidence for a different bonding mechanism in misfit layered compounds that was identified as covalent bonding in accordance to results from Chapter 7.

9 Summary and perspectives

We investigated the geometric and electronic structure of misfit layered compounds exemplarily for two different systems $(\text{PbS})_{1.18}\text{TiS}_2$ and $(\text{PbS})_{1.14}\text{NbS}_2$. The main attention was laid on two outstanding properties that are inherent to this special class of material: the incommensurability and the high stability of the perfect alternate stacking. The access to these questions is gained from two directions:

1. The comparison of electronic properties of misfit layered compounds to those of the single subsystems and
2. The creation of a similar system as it is achieved by growing epitaxial layers of PbS on transition metal dichalcogenide substrates.

As a first step misfit layered compounds were grown by a chemical vapor transport technique for which adequate growth parameters were found. The grown single crystals were then characterized with respect to their stacking order perpendicular to the surface and their lateral order that turned out to be nearly perfect over large fractions of the samples. The electronic structures of the misfit layered compounds and the constituting systems NbS_2 , NbSe_2 , TiS_2 and PbS on the one hand and epitaxial PbS films on TiS_2 substrates on the other were studied by means of photoelectron spectroscopy using synchrotron radiation. With the analysis of the deviations of the electronic states of the misfit compounds from those of the single subsystems or the epitaxial samples we gain valuable information about the above mentioned properties concerning the incommensurability and high stability. The conclusions that could be drawn from photoemission experiments could be confirmed by theoretical band structure calculations. The main results from these investigations are the following:

The constituents As an essential precondition for the interpretation of electronic properties of misfit layered compounds a profound knowledge of the respective properties of the constituents is needed. Therefore, the electronic structures of the underlying transition metal dichalcogenides were studied. NbSe_2 and TiS_2 reveal experimental band structures that coincide reasonable with band structure calculations. Contrarily, photoemission spectra of NbS_2 deviates from the theoretical band structure. The changes can be ascribed to a weak self-intercalation of excessive niobium atoms into the van der Waals gap of the layered compound. This interpretation is in agreement with other studies that result in the non-stoichiometry of NbS_2 due to excess niobium atoms.

The second subsystem of the misfit compounds under consideration is the narrow gap semiconductor lead sulphide. Photoemission spectra of this compound cannot be interpreted with a simple direct-transition model. Especially off-normal spectra exhibit additional emission structures that cannot be explained by direct transitions. Convincing agreement between theory and photoemission results can be achieved by applying the weighted one-dimensional density of states model. It implies the relaxation of the surface perpendicular component of the electron momentum during the photoemission process so that non-k-conserving transitions must be taken into account to interpret photoemission spectra. Instead of direct transitions it is here singularities in the one-dimensional density of states that give rise to peaks in photoemission spectra. Within this model we find perfect agreement between experiment and theory that allows us to locate the valence band maximum of

PbS at an energy of approximately 0.7 eV below the Fermi level. A thorough investigation of electronic states very close to the Fermi energy revealed occupied conduction band states that turn PbS into a degenerate semiconductor. An interpretation as surface effect could be excluded by means of optical transmittance measurements.

Incommensurability These compounds, transition metal dichalcogenides and the cubic PbS, are the constituents of the investigated misfit layered compounds. By an alternate stacking of the different subsystems misfit compounds are formed. With our measurements on the misfit sample $(\text{PbS})_{1.14}\text{NbS}_2$ it turned out that photoemission spectra are dominated by the contributions of the NbS_2 subsystem. The dispersion of electronic states and the hexagonal symmetry in reciprocal space are roughly maintained. The deviations in the electronic structure with respect to the TMDC constituent NbS_2 yield information about the bonding between the different subsystem layers at energies well below the Fermi level (see below) and about the influence of the incommensurability at the Fermi energy. Due to the different symmetry of the subsystems a one-dimensional misfit is created along one in-plane layer axis. The different lattice constants in this direction give rise to mutual modulations of both subsystems that establish a quasi-periodic potential. Hence, electrons in the NbS_2 subsystem are not only subjected to the potential with the periodicity of their own host lattice. The modulation with a periodicity determined by the PbS lattice disturbs the motion of the electrons within the incommensurate direction. Electrons in the vicinity of the Fermi level are scattered in a umklapp-like process and the dispersion of the respective electronic band is reversed and does not cross the Fermi level as it does in pristine NbS_2 . Consequently the Fermi surface is modified exhibiting a twofold symmetry in the misfit layered compound $(\text{PbS})_{1.14}\text{NbS}_2$.

A second evidence for the influence of the incommensurability was obtained by photoelectron diffraction. By orientating the incommensurate axis into the polarization plane of the incident light we obtained a distinct diffraction pattern of photoelectrons that was not observed for arbitrary orientations. We ascribe this effect to the localization of electrons in the incommensurate direction due to the quasi-periodic potential.

Stability X-ray diffraction and electron microscopy measurements revealed a precise alternate stacking of the different subsystems in misfit layered compounds. The highly ordered stacking is connected to a decreased entropy and must be compensated by a likewise decreased energy with respect to the single subsystems. These considerations are in agreement with the observed high stability of misfit compounds. Photoemission measurements unambiguously prove a charge transfer from the PbS layers to the TMDC subsystems of TiS_2 and NbS_2 , respectively that results in a filling of the conduction band and the opening of a gap between transition metal derived d states and sulphur derived p states ("p-d gap"). These effects are known from intercalated TMDC samples and confirm the description of misfit compounds as intercalation compounds. Although the charge transfer gives rise to an electrostatic attraction between the different layers it is not sufficient to explain the high stability and the mutual modulation of the subsystem layers. By employing k-space mapping modes of photoemission also in the direction perpendicular to the layers we observed dispersing electronic bands in this direction which are a clear evidence for covalent bonding between the different subsystem layers. These measurements represent the first direct experimental proof for covalent bonding that have only been proposed from theoretical considerations before.

Epitaxy As an intermediate state between the single subsystems and the misfit layered compound we produced epitaxial PbS films on transition metal dichalcogenides. The atomic arrangement of the epilayer on the substrate is determined by the special geometric conditions between the cubic (001) surface of PbS and the hexagonal TMDC surfaces. The PbS epilayer finds three equivalent commensurate directions on the TMDC surface and grows with its lattice constant along these directions. Thus a three-domain structure of the PbS film emerges. The second orthogonal in-plane lattice constant of each PbS domain is then – as in misfit compounds – incommensurate to the underlying lattice. The electronic structure of the epilayer and the substrate is less altered with respect to misfit compounds. Photoemission results of the epilayer can be described as a superposition of the emissions from the three domains. No further deviations from pristine PbS were observed. Apart from a weak electron transfer from the epilayer to the substrate no changes in the electronic structure of the substrate were observed either. The interaction between PbS film and substrate is limited to electrostatic forces induced by the transferred charge and therefore of different type than in misfit compounds. These conclusions could be verified by a thorough analysis of core level spectra of both epitaxial samples and the respective misfit compound. Due to the different type of bonding it is possible to grow PbS also on semiconducting TMDC substrates while misfit compounds containing non-metallic TMDC do not exist.

Quasi-periodic structures remain a fascinating and challenging topic of modern physics. In contrast to conventional crystalline material the study of their special properties has only just begun. Due to the lack of translational symmetry and the resulting failure of the Bloch concept the theoretical treatment of quasicrystals is difficult and band structure calculations can only be performed for approximants that describe the real structures only roughly. In the future new theoretical techniques should be developed to allow a precise interpretation of the various phenomena that have been found experimentally, e. g. the scattering of localized electrons in the valence band. A new concept could possibly be achieved by using the four-dimensional superspace where misfit layered compounds regain translational invariance.

Experimentally, the study of an influence of the quasi-periodicity on macroscopic properties such as thermal and electric conductivity should be intensified. Misfit layered compounds can be treated in this context as ideal model system since they exhibit both a conventional periodic and a quasi-periodic direction in one layer. The influence of the incommensurability can thus easily be extracted by comparing properties inherent to the respective direction.

References

- [1] Ferienschule Jülich: *Neue Materialien für die Informationstechnik*. Forschungszentrum Jülich GmbH, Institut für Festkörperforschung, Jülich (2001).
- [2] K. von Klitzing: *The quantized Hall effect*. Rev. Mod. Phys. **58**, 519 (1986).
- [3] H. L. Stormer: *Nobel Lecture: The fractional quantum Hall effect*. Rev. Mod. Phys. **71**, 875 (1999).
- [4] A. Y. Cho: *Growth of III-V Semiconductors by Molecular Beam Epitaxy and Their Properties*. Thin Solid Films **100**, 291 (1983).
- [5] L. L. Chang: *Molecular Beam Epitaxy*. in S. P. Keller, Ed., Handbook on Semiconductors, Vol. 3, North-Holland, Amsterdam (1980).
- [6] A. Koma: *Van der Waals epitaxy for highly lattice-mismatched systems*. J. Cryst. Growth **201-202**, 236 (1999).
- [7] Meerschaut, A.: *Incommensurate Sandwiched Layered Compounds*. Trans Tech Publications Ltd, P.O. Box 10, Hardstr.13, CH-4714 Aedermannsdorf, Switzerland (1992).
- [8] R. Lifshitz: *The symmetry of quasiperiodic crystals*. Physica A **232**, 633 (1996).
- [9] A. S. Woedtke: *Epitaxie von reinen und dotierten Fulleren- und Phtalocyanin-Schichtsystemen sowie Untersuchung ihrer geometrischen und elektronischen Eigenschaften*. Ph. D. thesis, Inst. f. Exp. u. Angew. Physik, Universität Kiel (2002).
- [10] J. Wilson, and A. Yoffe: *The Transition Metal Dichalcogenides, Discussion and Interpretation of the Observed Optical, Electrical and Structural Properties*. Adv. Phys. **18**, 193 (1969).
- [11] J. Rouxel: *Intercalated Layered Materials*. , ed. F. A. Lévy (D. Reidel, Dordrecht) (1979).
- [12] M. Inoue, H. P. Hughes and A. D. Yoffe: *The electronic and magnetic properties of the 3d transition metal intercalates of TiS_2* . Advances in Physics **38**, 565 (1989).
- [13] G. V. Subba Rao and M. W. Shafer: *Intercalated Layered Materials*. , ed. F. A. Lévy (D. Reidel, Dordrecht) (1979).
- [14] T. Ungár, P. Martinetto, G. Ribárik, E. Dooryhée, Ph. Walter and M. Anne: *Revealing the powdering methods of black makeup in Ancient Egypt by fitting microstructure based Fourier coefficients to the whole x-ray diffraction profiles of galena*. J. Appl. Phys. **91**, 2455 (2002).
- [15] H. Preier: *Recent advances in lead-chalcogenide diode lasers*. Appl. Phys. **20**, 189 (1979).
- [16] T. K. Chaudhuri : *A solar thermophotovoltaic converter using PbS photovoltaic cells*. Int. J. Eng. Res. **16**, 481 (1992).

- [17] H. Kanazawa and S. Adachi: *Optical properties of PbS*. J. Appl. Phys. **83**, 5997 (1998).
- [18] T. Grandke, L. Ley and M. Cardona: *Angle-resolved uv photoemission and electronic band structures of the lead chalcogenides*. Phys. Rev. B **18**, 3847 (1978).
- [19] W. Sterzel and J. Horn. Z. Anorg. Allgem. Chem. **376**, 254 (1970).
- [20] L. Schmidt: *Superconductivity in PbNbS₃ and PbTaS₃*. Physics Letters **31** (1970).
- [21] L. Schmidt, S. L. McCarthy and J. P. Maita: *Superconducting behavior of the system (Pb(Nb_{1-x}Ta_xS₃))*. Solid State Commun. **8**, 1513 (1970).
- [22] A. Lafond, A. Sulpice, C. Deudon and A. Meerschaut: *X-ray structure determination and magnetic properties at a new misfit layered compound: yttrium chromium sulfide (Y_{0.93}O_{0.07})_{1.28}CrS₂*. Eur. J. Solid State Inorg. Chem. **31**, 967 (1994).
- [23] J. Wulff, A. Meetsma, R. J. Haange, J. L. de Boer and G. A. Wiegers: *Structure and electrical transport properties of the misfit-layer compound (BiS_{1.08}TaS₂)*. Synth. Met. **39**, 1 (1990).
- [24] G. A. Wiegers, A. Meetsma, R. J. Haange, S. van Smaalen, J. L. de Boer, A. Meerschaut, P. Rabu and J. Rouxel : *The Incommensurate misfit Layer Structure of (PbS)_{1.14}NbS₂, 'PbNbS₃' and (LaS)_{1.14}NbS₂, 'LaNbS₃': an X-ray Diffraction Study*. Acta Crystallograph. B **46**, 324 (1990).
- [25] A. Meerschaut, L. Guemas, C. Auriel and J. Rouxel: *Preparation, structure determination and transport properties of a new misfit layer compound: (PbS)_{1.14}(NbS₂)₂*. Eur. J. Solid State Inorg. Chem. **27**, 557 (1990).
- [26] S. Van Smaalen, A. Meetsma, G. A. Wiegers and J. L. de Boer: *Determination of the Modulated Structure of the Inorganic Misfit Layer Compound (PbS)_{1.18}TiS₂*. Acta Crystallograph. B **47**, 314 (1991).
- [27] A. Meerschaut, C. Auriel and J. Rouxel. Less-Common Metals (1991).
- [28] C. Auriel, A. Meerschaut, C. Deudon, G. A. Wiegers, J. Baas, J. Chen and P. Monceau: *Electrical transport properties of mono- and bilayer misfit compounds (MX)_{1+x}(TX₂)_m, M = Sn, Pb; T = Ti, Nb; X = S, Se*. Eur. J. Solid State Inorg. Chem. **38**, 565 (1995).
- [29] C. M. Fang, A. R. H. F. Ettema, C. Haas, G. A. Wiegers, H. van Leuken and R. A. de Groot: *Electronic structure of the misfit-layer compound (SnS)_{1.17}NbS₂ deduced from band-structure calculations and photoelectron spectra*. Phys. Rev. B **52**, 2336 (1995).
- [30] K. Suzuki, T. Kondo, T. Enoki and S. Bandow. Synthetic metals **55** (1993).
- [31] Y. Moëlo, A. Meerschaut, J. Rouxel and C. Auriel: *Precise Analytical Characterization of Incommensurate Sandwiches Layered Compounds [(Pb, Sn)S]_{1+x}[(Nb, Ti)S₂]_m (0.08 ≤ x ≤ 0.28, M = 1-3). Role of Cationic Coupling on the Properties and the Structural Modulation*. Chem. Mater. **7**, 1759 (1995).

- [32] S. Hüfner: *Photoelectron spectroscopy*, in: *Springer Series in Solid-State Sciences*, Vol. 82. Springer, Berlin (1995).
- [33] H. Hertz: *Über einen Einfluß des ultravioletten Lichtes auf die elektrische Entladung*. Ann. Phys. **31**, 983 (1887).
- [34] A. Einstein: *Über einen die Erzeugung und Verwandlung des Lichtes betreffenden heuristischen Gesichtspunkt*. Ann. Phys. **17**, 132 (1905).
- [35] W. E. Spicer: *Photoemissive, Photoconductive, and Optical Absorption Studies of Alkali-Antimony Compounds*. Phys. Rev. **112**, 114 (1958).
- [36] C. N. Berglund and W. E. Spicer: *Photoemission Studies of Copper and Silver: Theory*. Phys. Rev. **136**, 1030 (1964).
- [37] P. J. Feibelman and D. E. Eastman: *Photoemission spectroscopy – Correspondence between quantum theory and experimental phenomenology*. Phys. Rev. B **10**, 4932 (1974).
- [38] P. Aebi, J. Osterwalder, P. Schwaller, L. Schlapbach, M. Shimoda, T. Mochiku and K. Kadowaki: *Complete Fermi Surface Mapping of $\text{Bi}_2\text{Sr}_2\text{CaCu}_2\text{O}_{8+x}$: Coexistence of Short Range Antiferromagnetic Correlations and Metallicity in the Same Phase*. Phys. Rev. Lett. **72**, 2757 (1994).
- [39] K. Rossnagel, O. Seifarth, L. Kipp, M. Skibowski, D. Voß, P. Krüger, A. Mazur and J. Pollmann: *Three-dimensional Fermi surface of 2H-NbSe_2 and its implications on the charge-density-wave mechanism*. Phys. Rev. B **64**, 235119 (2001).
- [40] K. Rossnagel, L. Kipp and M. Skibowski: *The charge-density-wave transition in 1T-TiSe_2 – excitonic insulator or band-type Jahn-Teller mechanism?* Phys. Rev. B, in press (2002).
- [41] S. Doniach and M. Sunjic: *Many-electron singularity in X-ray photoemission and X-ray line spectra from metals*. J. Phys. C **3**, 285 (1970).
- [42] D. P. Woodruff and T. A. Delchar: *Modern techniques of surface science*. Cambridge Solid State Science Series, Cambridge (1986).
- [43] G. Binnig and H. Rohrer. *Helvetica Physica Acta* **55**, 726 (1982).
- [44] C. J. Davisson and L. H. Germer: *Diffraction of Electrons by a Crystal of Nickel*. Phys. Rev. **30**, 705 (1927).
- [45] M. Boehme: *Electronic structure of the layered materials TaS_2 and Rb-covered WSe_2* . Ph. D. thesis, Inst. f. Experimentalphysik, Universität Kiel (1998).
- [46] L. Kipp: *New developments in direct and inverse photoemission techniques and electronic structure of $\text{Ge}(001) 2\times 1$ and $\text{Si}(001) 2\times 1$ surfaces*. Ph. D. thesis, Inst. f. Experimentalphysik, Universität Kiel (1992).
- [47] D. Kampfenger: *Inverse Photoemission und Rastertunnelmikroskopie am Mischkristallsystem $\text{Ti}_x\text{Ta}_{1-x}\text{S}_2$* . Diploma thesis, Inst. f. Experimentalphysik, Universität Kiel (1995).

- [48] M. Traving: *Epitaktisches Wachstum und elektronische Struktur eines Halbleiter-Heteroübergangs aus Schichtkristallen: HfS₂ auf WSe₂*. Ph. D. thesis, Inst. f. Exp. u. Angew. Physik, Universität Kiel (1998).
- [49] C. Kreis: *Heteroepitaxial Growth and Electronic Structure of Transition Metal Dichalcogenide Clusters and Ultrathin Films*. Ph. D. thesis, Inst. f. Exp. u. Angew. Physik, Universität Kiel (2002).
- [50] R. Kunz: *Epitaxie von PbS auf TiS₂: Untersuchung der geometrischen und elektronischen Struktur*. Diploma thesis, Inst. f. Exp. u. Angew. Physik, Universität Kiel (2002).
- [51] K. Rossnagel, S. Harm, L. Kipp, M. Skibowski: *A high performance angle-resolving electron spectrometer*. Nucl. Instrum. Methods Phys. Res. A **467** (2001).
- [52] K. Roßnagel: *Fermi surfaces and Charge-Density Waves of Quasi-Two-Dimensional Metals Imaged by High-Resolution Photoelectron Spectroscopy*. Ph. D. thesis, Inst. f. Exp. u. Angew. Physik, Universität Kiel (2001).
- [53] S. Harm: *Untersuchungen zur Energieauflösung eines Elektronen-Analysators für winkelaufgelöste Photoemission mittels einer computergesteuerten Elektronik*. Diploma thesis, Inst. f. Experimentalphysik, Universität Kiel (1989).
- [54] N. Trares: *Optimierung eines Experimentes für winkelaufgelöste Photoemission mit Synchrotronstrahlung*. Diploma thesis, Inst. f. Experimentalphysik, Universität Kiel (1991).
- [55] K.-U. Gawlik: *Untersuchung der elektronischen Struktur von II-VI-Verbindungshalbleitern mit direkter und inverser Photoemission*. Ph. D. thesis, Inst. f. Experimentalphysik, Universität Kiel (1996).
- [56] J. Kanzow: *Untersuchung der geometrischen und elektronischen Struktur von Heteroschichtsystemen: Epitaktisches TaS₂ auf WSe₂ und der Fehlanpassungskristall (PbS)_{1.14}NbS₂*. Diploma thesis, Inst. f. Exp. u. Angew. Physik, Universität Kiel (2000).
- [57] G. A. Wiegers, A. Meetsma, R. J. Haange and J. L. de Boer: *Structure of Tin Hafnium Sulfide and Lead Hafnium Sulfide*. Acta Crystallograph. C **45**, 847 (1989).
- [58] A. Y. Cho: *Film Deposition by Molecular Beam Techniques*. J. Vac. Sci. Tech. **8** (1971).
- [59] A. Y. Cho and J. R. Arthur: *Molecular Beam Epitaxy*. Prog. Solid-State Chem. **10**, 157 (1975).
- [60] A. Koma, K. Sonouchi and T. Miyajima: *Electronic Structure of a Monolayer NbSe₂ Film Grown Heteroepitaxially on the Cleaved Face of 2H-MoS₂*. Proc. 17th Int. Conf. on the Physics of Semiconductors, San Francisco 1984 (Springer, New York), 1465 (1985).
- [61] A. Koma, K. Sonouchi and T. Miyajima: *Fabrication and Characterization of Heterostructures with Subnanometer Thickness*. Microelectronic Engineering **2**, 129 (1984).

- [62] K. Ueno, K. Saiki, T. Shimada and A. Koma: *Epitaxial growth of transition metal dichalcogenides on cleaved faces of mica*. J. Vac. Sci. Tech. A **13**, 68 (1990).
- [63] E. Wisotzki, A. Klein and W. Jägermann: *Quasi van der Waals epitaxy of ZnSe on the layered chalcogenides InSe and GaSe*. thin solid films **380**, 263 (2000).
- [64] R. Rudolph, Y. Tomm, C. Pettenkofer, A. Klein and W. Jägermann: *Van der Waals xenotaxy: Oriented growth of hexagonal GaSe(001) on rectangular GaAs(110)*. Appl. Phys. Lett. **76**, 1101 (2000).
- [65] M. Horn-v. Hoegen, T. Schmidt, M. Henzler, G. Meyer, D. Winau and K. H. Rieder: *Epitaxial layer growth of Ag(111) films on Si(100)*. Surf. Sci. **331-333**, 575 (1995).
- [66] J. Cibert, Y. Gobil, K. Saminadayar, S. Tatarenko, A. Chami, G. Feuillet, Le Si Dang and E. Ligeon : *Growth of (111) CdTe on tilted (001) GaAs*. Appl. Phys. Lett. **54**, 828 (1989).
- [67] Z. R. Dai and F. S. Ohuchi: *Vacancy ordering of Ga₂Se₃ at GaSe/GaAs(100) interface*. Appl. Phys. Lett. **73**, 966 (1998).
- [68] J. Brandt, J. Kanzow, K. Rosnagel, L. Kipp, M. Skibowski, E. Krasovskii, W. Schattke, M. Traving, J. Stettner, W. Press, C. Dieker and W. Jaeger: *Band structure of the misfit compound (PbS)NbS₂ compared to NbSe₂: Experiment and Theory*. J. Electron Spectrosc. Relat. Phenom. **114** (2001).
- [69] R. M. A. Lieth: *Preparation and crystal growth of materials with layered structures*. D. Reidel Publishing Company, Dordrecht, Holland (1977).
- [70] G. A. Wiegers, A. Meetsma, R. J. Haange and J. L. de Boer: *Crystal growth, structure and some properties of PbNbS₃, SnSnbS₃, LaNbS₃ and related misfit layer compounds*. Solid State Ionics **32** (1989).
- [71] G. A. Wiegers, A. Meetsma, S. van Smaalen, R. J. Haange, J. Wulff, T. Zeinstra, J. L. de Boer, S. Kuypers, G. van Tendeloo, J. van Landuyt, S. Amelinckx, A. Meerschaut, P. Rabu and J. Rouxel: *Misfit layer compounds (MS)_nTS₂ (M=Sn, Pb, Bi, rare earth elements; T=Nb, Ta; n=1.08-1.19), a new class of layer compounds*. Solid State Comm. **70**, 409 (1989).
- [72] A. Meerschaut, R. Roesky, A. Lafond, C. Deudon and J. Rouxel: *Misfit layered compounds: Polytypism, multilayer stages, nonstoichiometry and electronic structure, self-misfit Compounds*. Journal of Alloys and Compounds **219**, 157 (1995).
- [73] J. Brandt, L. Kipp, M. Skibowski, E. E. Krasovskii, W. Schattke, E. Spiecker, C. Dieker and W. Jäger: *Charge transfer in misfit layered compounds*. submitted to Surf. Sci. (2002).
- [74] C. Dieker, E. Spiecker and W. Jäger: *private communication*. Mikrostrukturanalytik.
- [75] R. Adelung, L. Kipp, J. Brandt, L. Tarcak, M. Traving, C. Kreis and M. Skibowski: *Nanowire networks on perfectly flat surfaces*. Appl. Phys. Lett. **74**, 3053 (1999).
- [76] Brushy Creek Mine: *Truscon Minerals*.

- [77] O. Anderson: *Bandstrukturen, Phasentransformationen und Adsorbateffekte der 1T-Übergangsmetallchalkogenide in winkelaufgelöster Photoemission*. Ph. D. thesis, Inst. f. Experimentalphysik, Universität Kiel (1986).
- [78] E. E. Krasovskii: *private communication*. Institut für theoretische und Astrophysik.
- [79] M. Traving, B. Murphy and J. Stettner: *private communication*. Institut für Experimentelle und Angewandte Physik.
- [80] T. Grandke, L. Ley and M. Cardona: *Valence band structure of PbS from Angle-Resolved uv Photoemission*. Phys. Rev. Lett. **38**, 1033 (1977).
- [81] R. Böttner, S. Ratz, S. Marquardt, U. Gerhardt, R. Gaska and J. Vaitkus: *Analysis of angle-resolved photoemission data of PbS (001) surfaces within the direct-transition model*. Phys. Rev. B **53**, 10336 (1996).
- [82] S.-H. Wei and A. Zunger: *Electronic and structural anomalies in lead chalcogenides*. Phys. Rev. B **55**, 13605 (1997).
- [83] J. R. Chelikowsky and M. L. Cohen: *Nonlocal pseudopotential calculations for the electronic structure of eleven diamond and zinc-blende semiconductors*. Phys. Rev. B **14**, 556 (1976).
- [84] A. Santoni, G. Paolucci, G. Santoro, K. C. Prince and N. E. Christensen: *Band structure of lead sulphide*. J. Phys.: Condens Matter **4**, 6759 (1992).
- [85] T. Ollonqvist, T. Kaurila, M. Isokallio, M. Pukkinen and J. Väyrynen: *Inverse photoemission and photoemission spectra of the PbS(001) surface*. J. Electron Spec. Rel. Phen. **76**, 729 (1995).
- [86] A. B. Preobrajenski and T. Chassé: *Atomic and electronic structure of epitaxial PbS on InP(110) and InP(001)*. Appl. Surf. Sci. **166**, 201 (2000).
- [87] A. Cricenti, M. Tallarida, C. Ottaviani, B. Kowalski, E. Gutievitz, A. Szczerbakow and B. A. Orłowski: *Differential reflectivity and angle-resolved photoemission of PbS(100)*. Surf. Sci. **482** (2001).
- [88] D. Shechtman, I. Blech, D. Gratias and J. W. Cahn: *Metallic Phase with Long-Range Orientational Order and No Translational Symmetry*. Phys. Rev. Lett. **53**, 1951 (1984).
- [89] International Union of Crystallography: *Report of the Executive Committee for 1991*. Acta Cryst. A **48**, 922 (1992).
- [90] X. Wu, S. W. Kycia, C. G. Olson, P. J. Benning, A. I. Goldman and D. W. Lynch: *Electronic Band Dispersion and Pseudogap in Quasicrystals: Angular-resolved Photoemission Studies on Icosahedral Al₇₀Pd_{21.5}Mn_{8.5}*. Phys. Rev. Lett. **75**, 4540 (1995).
- [91] D. Naumović, P. Aebi, L. Schlapbach, C. Beeli, T. A. Lagrasso and D. W. Delaney: *Quasicrystalline nature of quasicrystal surfaces: A photoemission study*. Phys. Rev. B **60**, 16330 (1999).

- [92] S. Roche and T. Fujiwara: *Fermi surfaces and anomalous transport in quasicrystals*. Phys. Rev. B **58**, 11338 (1998).
- [93] G. Neuhold, S. R. Barmann, K. Horn, W. Theis, P. Ebert and K. Urban: *Enhanced surface metallic density of states in icosahedral quasicrystals*. Phys. Rev. B **58**, 734 (1998).
- [94] E. Rotenberg, W. Theis, K. Horn and P. Gille: *Quasicrystalline valence bands in decagonal AlNiCo*. nature **406**, 602 (2000).
- [95] C. de Lange and T. Janssen: *Electrons in incommensurate crystals: Spectrum and localization*. Phys. Rev. B **28**, 195 (1983).
- [96] J. Voit, L. Perfetti, F. Zwick, H. Berger, G. Margaritondo, G. Grüner, H. Höchst and M. Grioni: *Electronic Structure of Solids with Competing Periodic Potentials*. Science **290**, 501 (2000).
- [97] K. Suzuki, T. Enoki and S. Bandow: *Electronic properties and valence state of Sm in $(SmS)_{1.19}TaS_2$* . Phys. Rev. B **48**, 11077 (1993).
- [98] K. Suzuki, T. Enoki and H. Tajima: *Optical reflectivity and carrier localization in incommensurate misfit layer compounds $(MS)_xTaS_2$ ($M = \text{rare-earth metal, Pb, Sn}$)*. Phys. Rev. B **52**, 16401 (1995).
- [99] T. Kondo, K. Suzuki and T. Enoki: *Transport and magnetic properties of incommensurate layer compounds $(RES)_xVS_2$* . Solid State Commun. **84**, 999 (1992).
- [100] T. Greber, J. Wider, E. Wetli and J. Osterwalder: *X-Ray-Photoelectron Diffraction in the Backscattering Geometry: A Key to Adsorption Sites and Bond Length at Surfaces*. Phys. Rev. Lett. **81**, 1654 (1998).
- [101] P. J. Hardman, P. L. Wincott, G. Thornton, A. P. Kaduwela and C. S. Fadley: *X-ray photoelectron diffraction and Auger electron diffraction from $TiO_2(100)$* . Phys. Rev. B **60**, 11700 (1999).
- [102] C. S. Fadley: *The Study of Surface Structures by Photoelectron Diffraction and Auger Electron Diffraction*. in Synchrotron Research: Advances in Surface and Interface Science, Ed. R.Z. Bachrach, Plenum, New York, USA (1992).
- [103] C. Solterbeck, W. Schattke, J.-W. Zahlmann-Nowitzki, K.-U. Gawlik, L. Kipp, M. Skibowski, C. S. Fadley and M. A. van Hove: *Energetic and spatial bonding properties from angular distributions of ultraviolet photoelectrons: application to the $GaAs(110)$ surface*. Phys. Rev. Lett. **79**, 4681 (1997).
- [104] A. Landers, Th. Weber, A. Cassimi, M. Hattass, O. Jagutzki, A. Nauert, T. Osipov, A. Staudte, M. H. Prior, H. Schmidt-Böcking, C. L. Cocke and R. Dörner: *Photoelectron Diffraction Mapping: Molecules Illuminated from Within*. Phys. Rev. Lett. **87**, 013002 (2001).
- [105] J. Osterwalder, T. Greber, S. Hübner and L. Schlapbach: *X-Ray-Photoelectron Diffraction from a Free-Electron-Metal Valence Band: Evidence for Hole-State Localization*. Phys. Rev. Lett. **64**, 2683 (1990).

- [106] D. D. Sarma, W. Speier and J. F. van Acker: *Comment on "X-Ray-Photoelectron Diffraction from a Free-Electron-Metal Valence Band: Evidence for Hole-State Localization"*. Phys. Rev. Lett. **66**, 2634 (1991).
- [107] C. H. Rüscher, C. Haas, S. van Smaalen and G. A. Wiegers: *Investigation of the optical reflectivity of misfit layer compounds: $(MS)_nTS_2$ ($T=Ta, Nb$; $M=Sn, Pb, Sm, Tb, La$; $1.08 < n < 1.23$)*. J. Phys.: Condens. Matters **6**, 2117 (1994).
- [108] Y. Ohno: *Electronic structure of the misfit-layer compounds $PbTiS_3$ and $SnNbS_3$* . Phys. Rev. B **44**, 1281 (1991).
- [109] A.R.H.F. Ettema and C. Haas: *A LEED and photoemission spectroscopy study of the surface of the incommensurate misfit layer compound $(SnS)_{1.16}TaS_2$* . surface science **269** (1992).
- [110] L. Cario, D. Johrendt, A. Lafond, C. Felser, A. Meerschaut and J. Rouxel: *Stability and charge transfer in the misfit compound $(LaS)(SrS)_{0.2}CrS_2$: Ab initio band-structure calculations*. Phys. Rev. B **55**, 9409 (1997).
- [111] A. R. H. F. Ettema and C. Haas: *An x-Ray photoemission spectroscopy study of interlayer charge transfer in some misfit layer compounds*. J. Phys.: Condens. Matter **5**, 3817 (1993).
- [112] S. Van Smaalen: *Renormalization of bond valences: application to incommensurate intergrowth crystals*. Acta Crystallograph. A **48**, 408 (1992).
- [113] C. H. Chen, W. Fabian, F. C. Brown, K. C. Woo, B. Davies, B. Delong and A. H. Thompson: *Angle-resolved photoemission studies of the band structure of $TiSe_2$ and TiS_2* . Phys. Rev. B **21**, 615 (1980).
- [114] J. A. Wilson: *Modelling the contrasting semimetallic characters of TiS_2 and $TiSe_2$* . Phys. Status Solidi B **86**, 11 (1978).
- [115] A. H. Thompson: *Electron-Electron Scattering in TiS_2* . Phys. Rev. Lett. **35**, 1786 (1975).
- [116] S. Sharma, T. Nautiyal, G. S. Singh, S. Auluck, P. Blaha and C. Ambrosch-Draxl: *Electronic structure of $1T-TiS_2$* . Phys. Rev. B **59**, 14833 (1999).
- [117] D. R. Allan, A. A. Kelsey, S. J. Clark, R. J. Angel and G. J. Ackland: *High-pressure semiconductor-semimetal transition in TiS_2* . Phys. Rev. B **57**, 5106 (1998).
- [118] C. M. Fang, R. A. de Groot and C. Haas: *Bulk and surface electronic structure of $1T-TiS_2$ and $1T-TiSe_2$* . Phys. Rev. B **56**, 4455 (1997).
- [119] H. E. Brauer, H. I. Starnberg, L. J. Holleboom, H. P. Hughes and V. N. Strocov: *Modifying the electronic structure of TiS_2 by alkali metal intercalation*. J. Phys.: Condens. Matter **11**, 8957 (1999).
- [120] E. E. Krasovskii and W. Schattke: *Surface electronic structure with the linear methods of band theory*. Phys. Rev. B **56**, 12874 (1997).

- [121] E. E. Krasovskii, F. Starrost and W. Schattke: *Augmented Fourier components method for constructing the crystal potential in self-consistent band-structure calculations*. Phys. Rev. B **59**, 10504 (1999).
- [122] E. E. Krasovskii and W. Schattke: *Semirelativistic technique for $\mathbf{k} \cdot \mathbf{p}$ calculations: Optical properties of Pd and Pt*. Phys. Rev. B **63**, 235112 (2001).
- [123] V. Grasso: *Electronic structures and electronic transitions in layered materials*. Reidel, Boston, USA (1986).
- [124] T. Matsushita, S. Suga, A. Kimura, H. Negishi and M. Inoue: *Angle-resolved photoemission study of Ni-intercalated 1T-TiS₂*. Phys. Rev. B **60**, 1678 (1999).
- [125] C. Umrigar, D. E. Ellis, D. Wang, H. Krakauer and M. Posternak: *Band structure, intercalation, and interlayer interaction of transition metal dichalcogenides: TiS₂ and LiTiS₂*. Phys. Rev. B **26**, 4935 (1982).
- [126] H. I. Starnberg: *Recent developments in alkali metal intercalation of layered transition metal dichalcogenides*. Mod. Phys. Lett. B **14**, 455 (2000).
- [127] H. E. Brauer, H. I. Starnberg, L. J. Holleboom, V. N. Strocov and H. P. Hughes: *Electronic structure of pure and alkali-metal-intercalated VSe₂*. Phys. Rev. B **58**, 10031 (1998).
- [128] J. Rouxel, A. Meerschaut and G. A. Wiegers: *Chalcogenide Misfit Layer Compounds*. J. Alloys Comp. **229**, 144 (1995).
- [129] J. A. Con Foo, A. P. J. Stampfl, A. Ziegler, B. Mattern, M. Hollering, R. Denecke and L. Ley: *Direct k-space photoemission imaging of the Fermi surface of Cu*. Phys. Rev. B **53**, 9649 (1996).
- [130] G. Poalucci and K. C. Prince: *Surface core-level shift of lead sulfide*. Phys. Rev. B **41**, 3851 (1990).
- [131] A.B. Preobrajenski and T. Chassé: *Epitaxial growth and interface structure of PbS on InP(110)*. Appl. Surf. Science **142**, 394 (1999).
- [132] Sze, S. M.: *Physics of Semiconductor Devices*. John Wiley & Sons, New York (1981).
- [133] J. A. Wilson: *Charge-density waves in metallic, layered, transition-metal dichalcogenides*. Phys. Rev. Lett. **32**, 1703 (1974).
- [134] K. Motizuki and N. Suzuki: *Structural Phase Transitions of Layered Transition Metal Compounds*. K. Motizuki, Reidel, Dordrecht (1986).
- [135] M.-H. Whangbo, D.-K. Seo and E. Canadell: *Structural and electronic instabilities of transition metal dichalcogenides, Physics and Chemistry of Low-Dimensional Inorganic Conductors*. C. Schlenker, J. Dumas, M. Greenblatt and S. van Smaalen, Springer Verlag, Berlin (1994).
- [136] G. Grüner: *Density Waves in Solids*. Addison-Wesley, Reading (1994).

-
- [137] Liang, W.Y.: *Electronic Properties of Transition Metal Dichalcogenides and their Intercalation Complexes*. M.S.Dresselhaus, New York (1986).
- [138] R. Friend and A. Yoffe: *Electronic Properties of Intercalation Complexes of Transition Metal Dichalcogenides*. Advances in Physics **36**, 1 (1987).
- [139] J. Brandt: *Der Einfluß von Nanostrukturen auf die geometrische und elektronische Struktur von metallischen Schichtkristallen*. Diploma thesis, Inst. f. Exp. u. Angew. Physik, Universität Kiel (1999).
- [140] R. Adelung, J. Brandt, L. Tarcak, L. Kipp and M. Skibowski: *Charge density waves affected by Rb nanowire network formation on 1T-TaS₂*. Appl. Surf. Sci **162-163**, 666 (2000).
- [141] R. Adelung, J. Brandt, L. Kipp and M. Skibowski: *Reconfiguration of charge density waves by surface nanostructures*. Phys. Rev. B **63**, 165327 (2001).
- [142] H.I. Starnberg, H.E. Brauer, L.J. Holleboom and H.P. Hughes: *3D-to-2D Transition by Cs Intercalation of VSe₂*. Phys. Rev. Lett. **70**, 3111 (1993).
- [143] R. Adelung, J. Brandt, K. Rossnagel, O. Seifarth, L. Kipp, M. Skibowski, C. Ramírez, T. Strasser and W. Schattke: *Tuning Dimensionality by Nanowire Adsorption on Layered Materials*. Phys. Rev. Lett. **86**, 1303 (2001).

List of abbreviations

ARPES	angle-resolved photoelectron spectroscopy
ASPHERE	Angular Spectrometer for Photoelectrons with High Energy Resolution
BW	bypass-wiggler
BZ	Brillouin zone
CBM	conduction band minimum
CDW	charge-density wave
CVT	chemical vapor transport
DESY	Deutsches Elektronen-Synchrotron
DORIS	Doppelringspeicher
DOS	density of states
EDC	energy distribution curve
EDX	energy dispersive X-ray
ESCA	electron spectroscopy for chemical analysis
HASYLAB	Hamburger Synchrotronstrahlungslabor
HONORMI	hochauflösender Normal-Incidence-Monochromator
LDOS	local density of states
MBE	molecular beam epitaxy
ODDS	one-dimensional density of states
PAD	photoelectron angular distribution
PLD	periodic lattice distortion
RBM	rigid band model
RT	room temperature
SBZ	surface Brillouin zone
SDOS	surface density of states
SEM	scanning electron microscope
STM	scanning tunneling microscope
TED	transmission electron diffraction
TEM	transmission electron microscope
TMDC	transition metal dichalcogenide
UHV	ultrahigh vacuum
UPS	ultraviolet photoelectron spectroscopy
VBM	valence band maximum
VDWE	van der Waals epitaxy
VUV	vacuum ultraviolet
XPD	X-ray photoelectron diffraction
XPS	X-ray photoelectron spectroscopy
XRD	X-ray diffraction

List of publications

International journals

1. R. Adelung, L. Kipp, J. Brandt, L. Tarcak, M. Traving, C. Kreis, M. Skibowski, *Nanowire networks on perfectly flat surfaces*, Applied Physics Letters **74**, 3053 (1999).
2. R. Adelung, J. Brandt, L. Tarcak, L. Kipp, M. Skibowski, *Charge density waves affected by Rb nanowire network formation on 1T-TaS₂*, Applied Surface Science **162-163**, 666 (2000).
3. R. Adelung, J. Brandt, K. Rossnagel, O. Seifarth, L. Kipp, M. Skibowski, C. Ramírez, T. Strasser, W. Schattke, *Tuning dimensionality by nanowire adsorption on layered materials*, Physical Review Letters **86**, 1303 (2001).
4. R. Adelung, J. Brandt, L. Kipp, M. Skibowski, *Reconfiguration of charge density waves by surface nanostructures*, Physical Review B **63**, 165327 (2001).
5. J. Brandt, J. Kanzow, K. Rossnagel, L. Kipp, M. Skibowski, E. E. Krasovskii, W. Schattke, M. Traving, J. Stettner, W. Press, C. Dieker, W. Jäger, *Band structure of the misfit compound (PbS)NbS₂ compared to NbSe₂: Experiment and Theory*, Journal of Electron Spectroscopy and Related Phenomena **114-116**, 555 (2001).
6. E. E. Krasovskii, O. Tiedje, W. Schattke, J. Brandt, J. Kanzow, K. Rossnagel, L. Kipp, M. Skibowski, M. Hytha, B. Winkler, *Electronic structure and UPS of the misfit chalcogenide (SnS)NbS₂ and related compounds*, Journal of Electron Spectroscopy and Related Phenomena **114-116**, 1133 (2001).
7. J. Brandt, L. Kipp, M. Skibowski, E. E. Krasovskii, W. Schattke, E. Spiecker, C. Dieker, W. Jäger, *Charge transfer in misfit layered compounds*, accepted for publication in Surface Science.
8. J. Brandt, J. Kanzow, L. Kipp, M. Skibowski, K. Rossnagel, K. Horn *Bonding mechanisms in the misfit layered compound (PbS)_{1.14}NbS₂*, in preparation
9. J. Brandt, L. Kipp, M. Skibowski, *Tracing the incommensurability in the electronic structure of misfit layered compounds*, in preparation
10. J. Brandt, R. Kunz, L. Kipp, M. Skibowski, E. Spiecker, W. Jäger, *Epitaxial growth of thin PbS films on TiS₂ and comparison to the misfit layered compound PbS_{1.18}TiS₂*, in preparation

11. S. Woedtke, J. Brandt, L. Kipp, M. Skibowski,
Interaction of K and Cl in C₆₀ fullerite thin films,
in preparation
12. S. Woedtke, J. Brandt, L. Kipp, M. Skibowski,
Titanyl phthalocyanine doped with chlorinated C₆₀ as improved photoacceptor,
in preparation

International conferences

1. J. Brandt, L. Kipp, M. Skibowski, E. E. Krasovskii, W. Schattke, E. Spiecker, C. Dieker and W. Jäger,
Charge transfer in misfit layered compounds,
21st European Conference on Surface Science, Malmö (Sweden) 2002, poster presentation.

Research reports

1. R. Adelung, J. Brandt, L. Kipp and M. Skibowski,
Nanowire network induced changes of electronic states visualized by Photoemission on layered 1T-TaS₂,
HASYLAB Annual Report 1999.
2. J. Brandt, J. Kanzow, K. Rosnagel, L. Kipp and M. Skibowski,
Experimental band structure of the misfit layer compound (PbS)NbS₂ in comparison to NbS₂ and NbSe₂,
HASYLAB Annual Report 2000.
3. S. Woedtke, J. Brandt, L. Kipp and M. Skibowski,
Interaction of K and Cl in C₆₀ fullerite thin films,
HASYLAB Annual Report 2000.
4. J. Brandt, R. Kunz, L. Kipp and M. Skibowski,
On the valence band maximum of PbS,
HASYLAB Annual Report 2001.
5. J. Brandt, R. Kunz, L. Kipp and M. Skibowski,
The electronic structure of epitaxial PbS on TiS₂,
HASYLAB Annual Report 2002.

Acknowledgements

As a colleague guessed I have certainly profited a lot from the last years that I passed here. I learnt about the difficulties of experimental physics and in particular ultra-high vacuum. But especially I learnt that quite a lot is much easier if one accepts the help of others. And therefore I wish to thank those who helped me not only in doing some research but who also made the last years largely endurable and mostly even pleasant:

- I have been fortunate to have Prof. M. Skibowski and L. Kipp as supervisors. I want to thank them for leaving me a lot of freedom in doing research and preparing talks and discussing my results and offering new ideas.
- This thesis would never have become that extensive without the support from J. Kan-zow and R. Kunz who accompanied me at numerous beam times in Hamburg and a lot of measuring sessions in Kiel. I very much appreciated working with them and often it was a lot of fun.
- In particular I wish to thank my colleagues that made life in the fourth floor easier until recently. And even after they had left they were always there for me in times of need. Thanks to C. Kreis and K. Rossnagel!
- I also very much acknowledge the constant support from S. Harm not only in terms of electronical and vacuum help, but even more for recognizing my sometimes very bad mood and for trying to help me out.
- Furthermore I wish to thank S. Woedtke, O. Seifarth, S. Gliemann, M. Kalläne and all other colleagues for the good spirit and encouragement they have offered.
- I gratefully acknowledge the collaboration and support of all members of the Forscher-gruppe who performed valuable calculations and measurements that helped to enlighten the mysteries of misfits: E. E. Krasovskii and Prof. W. Schattke, C. Dieker, E. Spiecker and Prof. Jäger, M. Traving, B. Murphy and J. Stettner, U. Cornelissen and Prof. F. Tuzek, S. Herzog and L. Ehm and probably those I have forgotten here.
- For technical support, excellent crystals and every kind of advice I thank M. Stiller, W. Krüger, J. Neubauer, W. D. Dau and M. Brix and his crew.
- I wish to send my special thanks to M. Seeger for helping me out of administrative difficulties and for her ability to cheer me up.
- Also I am very grateful to my parents, my brother and my sister-in-law who rescued me several times from HASYLAB and recovered me after exhausting beam-times.
- Finally I want to thank Rainer Kunz once more for all he did for me that goes far beyond all the physical stuff and who taught me to redefine the importance of different matters.

Lebenslauf

Julia Brandt
Goethestr. 28
geboren am 19. September 1973 in Pinneberg
deutsche Staatsangehörigkeit

- 1980 – 1984 Helene-Lange-Schule in Pinneberg
1984 – 1986 Theodor-Heuss-Schule in Pinneberg
1986 – 1989 Deutsche Schule in Den Haag
1989 – 1993 Deutsche Schule in Brüssel
Mai 1993 Allgemeine Hochschulreife
- 1993 – 1999 Studium der Physik (Nebenfach Chemie) an der
Christian-Albrechts-Universität zu Kiel
- November 1995 Diplomvorprüfung
- Mai 1998 Diplomhauptprüfung der Physik
- 1998 – 1999 Diplomarbeit bei Prof. Dr. M. Skibowski zum Thema:
Der Einfluß von Nanostrukturen auf die geometrische und elektronische Struktur von metallischen Schichtkristallen
- August 1999 Beginn der Dissertation bei Prof. Dr. M. Skibowski
1999 – 2003 wissenschaftliche Angestellte am Institut für Experimentelle und Angewandte Physik der Universität Kiel

Eidesstattliche Erklärung

Hiermit erkläre ich an Eides Statt, daß ich diese Arbeit selbständig unter der Beratung meiner wissenschaftlichen Lehrer und nur mit den angegebenen Hilfsmitteln erstellt habe.

Diese Arbeit wurde weder ganz noch in Teilen an anderer Stelle im Rahmen eines Prüfungsverfahrens vorgelegt.

Frühere Promotionsversuche wurden von mir nicht vorgenommen.

Kiel, den

Kurzfassung

In der vorliegenden Arbeit wurde die geometrische und elektronische Struktur von den schichtartig aufgebauten Fehlanpassungs-Verbindungen $(\text{PbS})_{1.14}\text{NbS}_2$ und $(\text{PbS})_{1.18}\text{TiS}_2$ untersucht. Das Konzept des Wachstums von Volumenkristallen mittels eines chemischen Transportverfahrens wird erklärt, und die so gewachsenen Kristalle werden hinsichtlich ihrer Stapelordnung, ihrer lateralen Ordnung, chemischen Reinheit und der Eigenschaften ihrer Spaltfläche charakterisiert.

Eine zweite Methode zur Kristallzucht stellt die Molekularstrahlepitaxie (MBE) dar. Dieser Prozess erlaubt das Wachsen dünner Filme von PbS auf verschiedenen Übergangsmetalldichalkogenid (ÜMDC) -Substraten von Submonolagen bis zu einigen Nanometer Dicke. Epitaktische Proben stellen ein Zwischensystem zwischen Fehlanpassungs-Verbindungen und den reinen Komponentenkristallen NbS_2 oder TiS_2 und PbS dar.

Die elektronische Struktur der Konstituenten von Fehlanpassungs-Verbindungen wurde mit winkelaufgelöster Photoemission untersucht. Die experimentelle Bandstruktur von TiS_2 stimmt sehr gut mit theoretischen Bandstruktur-Rechnungen überein. Photoemissionsspektren von NbS_2 zeigten dagegen Abweichungen, die als Folge einer schwachen Selbstinterkalation von überschüssigen Niobatomen in die van der Waals Lücke der Schichtkristalle interpretiert werden konnten. Für die Interpretation der Photoemissionsmessungen von PbS versagt das einfache Modell der direkten Übergänge. Ein passendes Modell stellt das Modell der gewichteten eindimensionalen Zustandsdichte dar, das sowohl direkte Übergänge als auch Übergänge, in denen die senkrechte Komponente des Elektronenimpulses relaxiert ist, berücksichtigt. Photoemissionsexperimente zeigten die elektronische Besetzung des Leitungsbandes. Optische Transmissionsspektroskopie bestätigten diese Ergebnisse und schlossen die Interpretation als Oberflächeneffekt aus.

Fehlanpassungs-Verbindungen zeigen im Zusammenhang mit ihrer ungewöhnlichen geometrischen Struktur zwei herausragende Eigenschaften: Aufgrund der unterschiedlichen Symmetrie der beiden Untersysteme bildet sich eine eindimensionale Fehlanpassung entlang einer in der Schichtebene liegenden Achse. Die unterschiedlichen Gitterkonstanten in dieser Richtung erzeugen gegenseitige räumliche Modulationen beider Untersysteme und damit ein quasiperiodisches Potential. Elektronen an der Fermienergie werden entlang der inkommensurablen Richtung gestreut. Dieser Prozeß bewirkt eine Umkehrung der Dispersion des Leitungsbandes; folglich ändert sich die Fermifläche von $(\text{PbS})_{1.14}\text{NbS}_2$ im Vergleich zu reinem NbS_2 und weist eine zweizählige Symmetrie auf.

Die hohe Stabilität und vor allem die exakte Stapelfolge ihrer beiden Untersysteme bedürfen einer starken Wechselwirkung zwischen den unterschiedlichen Schichten. Wir konnten zweifelsfrei einen Elektronentransfer von der PbS-Schicht zum ÜMDC-Untersystem nachweisen. In Photoemissionsspektren wird der Ladungstransfer sichtbar durch das Auffüllen des Leitungsbandes im ÜMDC-Untersystem und durch das Öffnen einer Energielücke zwischen Übergangsmetall abgeleiteten d Zuständen und Schwefel p Zuständen. Trotzdem genügt die daraus resultierende elektrostatische Anziehung nicht aus, um die hohe Stabilität und die gegenseitige Modulation der beiden Untersysteme zu erklären. Zusätzlich zum Ladungstransfer fanden wir erste direkte experimentelle Hinweise für kovalente Bindungen zwischen den unterschiedlichen Untersystemen, die für die zuletzt genannten Effekte verantwortlich sind.

In epitaktischen Proben spiegelt sich die unterschiedliche Geometrie der Untersysteme in der atomaren Anordnung des PbS-Films auf dem ÜMDC-Substrat wider. Die hexagonale ÜMDC-Oberfläche weist drei äquivalente Richtungen auf, in denen das kubische PbS-System mit einer seiner in der Schichtebene liegenden Gitterkonstanten kommensurabel aufwachsen kann. Auf diese Weise entsteht eine Drei-Domänen-Struktur, die mittels Elektronenbeugung bestätigt wurde und die auch in Photoemissionsmessungen sichtbar wird. Die Bindung zwischen PbS-Film und dem Substrat beruht auf einem Ladungstransfer. Kovalente Anteile konnten ausgeschlossen werden und wir fanden deutliche Hinweise, daß im Gegensatz zu Fehlanpassungs-Verbindungen eine gegenseitige Modulation der Untersysteme nicht existiert.

Abstract

In the present thesis the geometric and electronic structures of the misfit layered compounds $(\text{PbS})_{1.14}\text{NbS}_2$ and $(\text{PbS})_{1.18}\text{TiS}_2$ have been investigated. The concept of growing bulk misfit compounds by a chemical transport technique is explained and the crystals that were grown are characterized with respect to their stacking order, their lateral order, chemical purity and the properties of their cleavage plane.

A second technique for crystal growth is constituted by molecular beam epitaxy (MBE). This process allows to grow thin films of PbS on different transition metal dichalcogenide (TMDC) substrates from submonolayers to some nanometer thickness. Epitaxial samples represent an intermediate system between misfit compounds and the pure component crystals NbS_2 or TiS_2 and PbS.

The electronic structures of the constituents of misfit layered compounds was investigated by angle-resolved photoemission. The experimental band structure of TiS_2 was found to be in very good agreement with theoretical band structure calculations. Photoemission spectra of NbS_2 on the other hand exhibited deviations that could be interpreted as a consequence of a weak self-intercalation of excessive niobium atoms into the van der Waals gap of the layered material. For the interpretation of photoemission measurements on PbS the simple direct-transition model failed. An adequate model was found in the weighted one-dimensional density of states model that takes both direct transitions and transitions where the perpendicular component of the electron momentum is relaxed into account. Photoemission experiments proved the electronic occupation of the conduction band. Optical transmittance spectroscopy confirmed these results and excluded the interpretation as surface effect.

Misfit layered compounds exhibit two outstanding properties that are connected to their unusual geometric structure: Due to the different symmetry of the subsystems a one-dimensional misfit is created along one in-plane layer axis. The different lattice constants in this direction give rise to mutual spatial modulations of both subsystems that establish a quasiperiodic potential. Electrons at the Fermi energy are scattered along the incommensurate direction. This process results in a reversed dispersion of the conduction band; consequently the Fermi surface is altered with respect to pristine NbS_2 and exhibits a two-fold symmetry in $(\text{PbS})_{1.14}\text{NbS}_2$.

The high stability and in particular the exact alternate stacking of their two subsystems require strong interactions between the different layers. We could unambiguously prove an electron transfer from the PbS layer to the TMDC subsystem. In photoemission spectra the charge transfer is evident from a filling of the conduction band of the TMDC subsystem and an opening of a gap between transition metal derived d states and sulphur p states. Nonetheless, the resulting electrostatic attraction is not sufficient to explain the high stability and the mutual modulation of both subsystems. In addition to the charge transfer we found a first direct experimental evidence for covalent bonding between the different subsystems that accounts for those latter effects.

In epitaxial samples the different geometry of the subsystems is mirrored in the atomic arrangement of the PbS epilayer on the TMDC substrate. The hexagonal TMDC surface exhibits three equivalent directions in which the cubic PbS system can grow commensurately with one of its in-plane layer constants. Hence, a three-domain structure emerges that was confirmed by electron diffraction and that was also found in photoemission measurements. The bonding between the PbS epilayer and the substrate was determined to be due to a charge transfer. Covalent contributions can be excluded and we found evidence that mutual modulations of the subsystems are absent in contrast to misfit layered compounds.